4-2015

Biophysical Interaction Between Nanoparticles and Biomolecules

Slaven Radic
Clemson University, sradic@clemson.edu

BIOPHYSICAL INTERACTION BETWEEN
NANOPARTICLES AND BIOMOLECULES

_____

A Dissertation
Presented to
Graduate School of
Clemson University

_____

In Partial Fulfillment of
Requirements for the Degree
Doctor of Philosophy
Physics

_____

by
Slaven Radic
April 2015

_____

Accepted by:
Dr. Feng Ding, Committee Chair
Dr. Apparao Rao
Dr. Emil Alexov
Dr. Jian He

ABSTRACT

In the last two decades nanotechnology market has undergone remarkable growth. Breakthroughs in nanomaterial synthesis increased diverse nanomaterials production and subsequently their application. Owing to its large surface to volume ratio and remarkable physical properties not seen in the bulk materials, nanoparticles are finding emerging use in industry and medicine. Hence, it is expectable that at some point these nanomaterials will end up released into the environment and interact with bio systems. The purpose of this dissertation is to elicit implications of nanomaterial transformation once it gets inside biological milieu.

After literature review and introduction given in Chapter 1, Chapter 2 will discuss toxic effect of single and multi-walled carbon nanotubes (SWCNT, MWCNT) onto cells, once these nanoparticles' surface gets covered by blood plasma protein - fibrinogen, forming so called protein corona. Although, experimental technics enable protein corona characterization trough measuring binding affinities, protein residence time and detection of protein conformational changes, my curiosity to understand this phenomenon on molecular level, led me to use of computational approaches like molecular dynamics.

In Chapter 3 we will explore formation of nanoparticle-protein corona, using molecular dynamics methods and try to understand at molecular level, genesis of this entity. Our model system will consist of silver nanoparticle covered in citrate and ubiquitous protein found in every eukaryotic cell-ubiquitin.

Chapter 4 will deal with protein corona evolution on graphene and graphene oxide surface, where we will see how binding affinity and concentration of different natural amphiphiles determines corona composition over time.

Chapter 5 will explore how the surface chemistry of fullerenes affects protein stability. Fullerene surface is randomly covered with different number of hydroxyl groups, controlling its degree of hydrophobicity.

Finally, Chapter 6 will examine impact of nanomaterials on protein aggregation propensities. A lot of experimental studies found out that some nanoparticles promote while other hinder protein aggregation. We will try to delineate how interaction strength between nanoparticle surface and protein residues, relative concentration and protein stability influence aggregation tendency. In Chapter 7 will be given brief conclusion and future course in the field.

The aim of this study is to investigate at molecular level influence of nanoparticle-protein interaction on protein structural changes, binding affinities and aggregation which eventually can have beneficial or adverse effects onto biological system. Studying these interactions will give us better understanding of the fate of nanomaterials in biological milieu and help set future directions of their safe application in biomedical use.

DEDICATION

To David I. Chipurnoi, my sister Zorica Radic and my parents, without who I wouldn't be able to pursue my dreams.

TABLE OF CONTENTS

LIST OF FIGURES

LIST OF TABLES

CHAPTER 1

LITERATURE REVIEW

1. Introduction: Nanotechnology Market Growth

Two decades ago, an IBM scientist named Don Eigler constructed his employer company logo in letters by manipulating individual atoms. This endeavor was visual embodiment of scientific advancement that indicated power of nanotechnology to rebuild matter by manipulating atoms and molecules to obtain desired properties. The National Scientific Foundation (NSF) established its first program dedicated to research in nanotechnology in 1991, but only in the beginning of 21st century disintegrated fields of nanoscience and engineering were brought together under the same ten years vision outlined in Nanotechnology Research Directions[1]. This proposal was adopted in 2000 as official document of National Science and Technology Council (NSTC) and pawed the road for rapid emergence of nanotechnology in the beginning of 21st century.

NSF and NNCO-funded independent study spotted more than 1 trillion in global revenue form nano-enabled products just in 2013 (see http://www.nsf.gov/news/news_summ.jsp?cntn_id=130586&org=NSF&from=news). Also, Innovative Research and Products analysts identified rapid growth in approved patents related to nanotechnology[2] (Figure 1.1). For example, just in 2008 there were around 10,067 patent applications filed per year[2]. Whether it is development of nanotechnology based solar panels, novel cancer treatment or bio imaging, predicted growth of this emerging market for 2014-2020 period is 16.5 % as drawn in Nanotechnology Market Outlook 2020 by RNCOS' analysts[3].

Recognizing the advantage of targeted drug treatment and promising use of nanomaterials as drug delivery vehicles, healthcare industry is poised to be among the first ones to see benefits of nanotechnology. Cientifica's report, Nanotechnology for Drug Delivery 2012, gives analysis and geographical breakdown of nanotechnology drug delivery market[4]. The market growth for 2000-2010 shows it reached 1,030 million USD.

Total number of nanotechnology applications per year

Year	All applications	Non-overlapping applications
1991	224	224
2000	1,197	1,153
2008	12,776	10,067
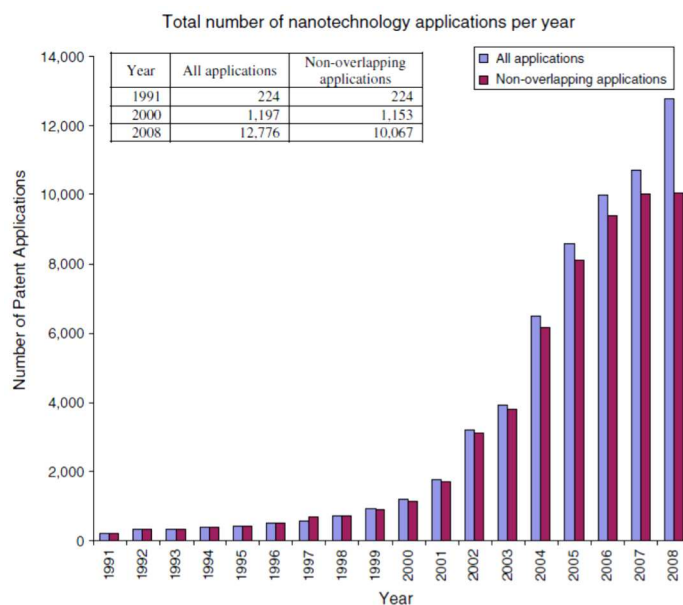
Figure 1.1. Growth in reported nanotechnology based application over time[2]. Springer and Journal of Nanoparticle Research, Vol. 12, 2010, pp 687-706, Trends in worldwide nanotechnology patent applications; 1991 to 2008, Dang ,Y., Zhang, Y., Fan, L., Chen, H. & Roco, M. C., Fig. 1 Copyright © Springer Science+Business Media B.V. 2009is given to the publication in which the material was originally published, by adding; with kind permission from Springer Science and Business Media.

2. Nanomaterials: Properties and Applications

Particles with at least one of three spatial dimensions less than 100 nm are termed as nanoparticles. They generally come in different shapes, sizes and chemical structure. Ranging from metallic (Au, Ag, Cu, Fe), semiconducting (quantum dots), carbon based (nanotubes, fullerenes, graphene, nano-diamonds) to polymer and co-polymer based nanoparticles; these materials are finding colossal potential use in industry, biomedicine or pharmacology[5–9].

Metallic nanoparticle. Metallic nanoparticles are ideal candidates for use in bio-imaging due to unique physicochemical properties that enable these nanomaterials to act as contrasting agents[10]. Gold nanoparticles, also called colloidal gold, is suspension of nano-sized particles of gold. Depending on its diameter, the color of this suspension can be red for nanoparticles less than 100 nm to yellow for larger nanoparticles[11,12] (Figure 1.2). Also, depending on the shape of gold nanoparticles their color can be changed and this is seen especially in the case of gold nano-rods. These interesting optical properties of gold nanoparticles are due to their specific interaction with light[13]. Once electromagnetic wave (EM) reaches the surface of gold nanoparticle it interacts with free electrons near the metal surface, forcing them to oscillate[14]. This process termed as localized surface plasmon resonance (LSPR) has characteristic resonant frequency, at which is seen EM absorption peak. Once EM wave is absorbed, excited plasmons dissipate energy through the light scattering or heat.

Owing to its optical properties gold nanoparticles are finding use in targeted bio imaging. Antibody-conjugated gold nanoparticles allow real time detection of penetration of gold particles into living cell at single molecule level by utilizing confocal microscopy method[15]. The basic concept of this technique is that object luminescence is excited by absorption of one or two photons with lower energy compared to the one needed for fluorescence. The advantage of this method is in reduction in noise to signal ratio and increase in contrast. Utilizing this benefit of gold nanoparticles, they are being used as tumor markers on the surface or inside the cell[16]. Also, dark field microscopy based on the light scattering from the objects, including the objects with size lower than the resolution of the microscope is one of the most popular techniques using gold nanoparticles in imaging[17]. As the scattering cross section of particle is 3-5 orders of magnitude than of fluorescence labels[15], gold nanoparticles are exploited to enhance visualization against the dark background. Once functionalized with proper antigens, these nanoparticles can preferentially bind or penetrate into tumor cells and in that way facilitate diagnostics up to accuracy of several cells[15].
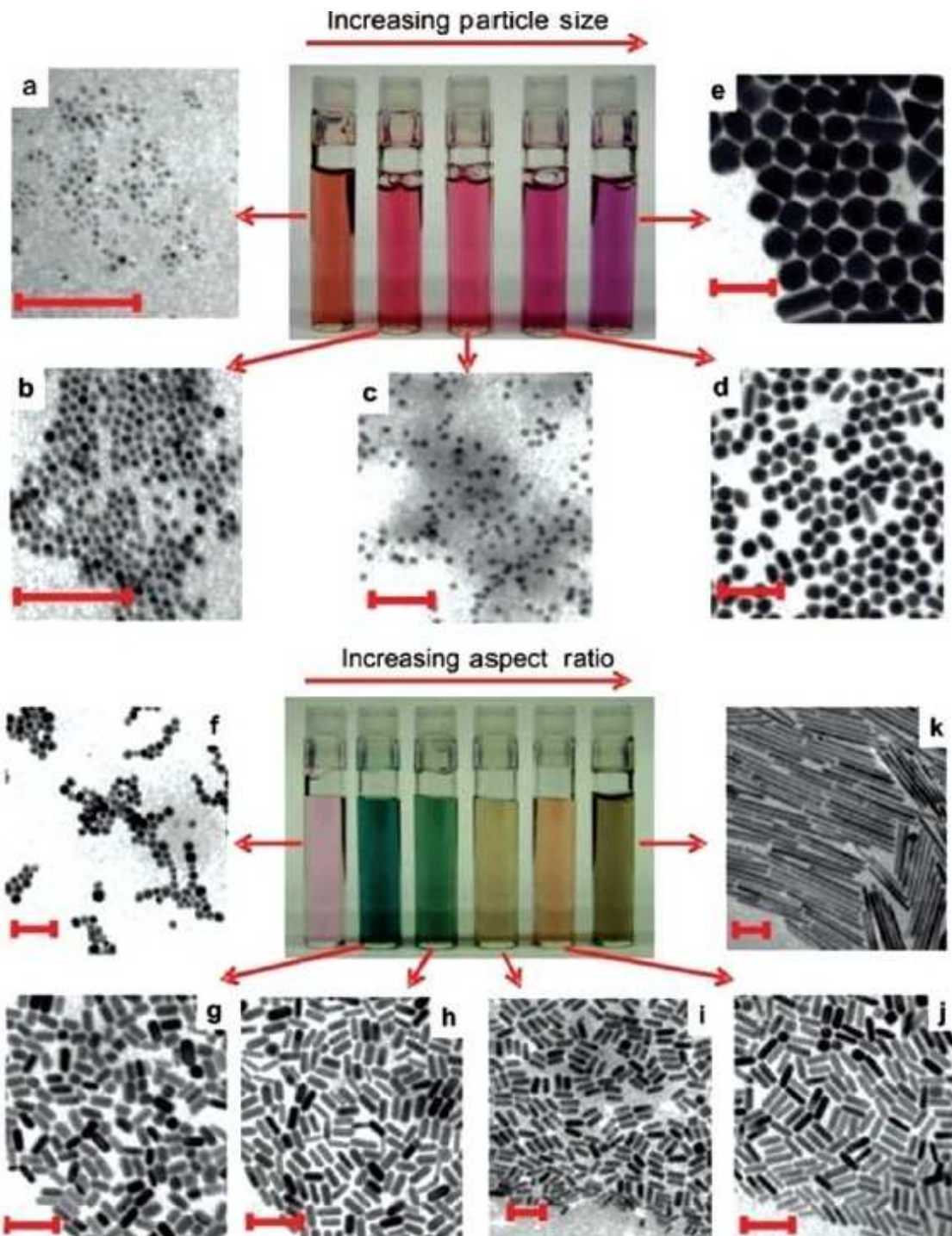
Figure 1.2. Colloidal gold suspension color dependence on the size and shape[14]

Silver nanoparticles (AgNP) are nanoparticles of silver ranging in size[18] from 1 to 100 nm. Their antimicrobial properties are the most explored ones[19–21]. The advantage of using nanoparticles compared to other chemical antimicrobial instruments is that microorganisms will be harder to become resistant to nanoparticles' antimicrobial effect. The exact mechanism of AgNP antimicrobial action isn't fully understood, but some studies suggest that silver ions play the major role[22] through electrostatic interaction between positively charged Ag ions and negatively charged microorganism membrane. On contrary, other study reported that destructive effect of AgNP on gram-negative bacteria was dependent on nanoparticle concentration and associated with formation of "pits" in the cell wall of bacteria[23,24]. Using electron spin resonance spectroscopy, studies found that when in contact with cell membrane, AgNP promote release of free radicals that subsequently damage cell membrane[19,25]. Putting aside detailed mechanism of silver nanoparticles microbial inhibitory effect, these studies suggest that AgNPs can be used as effective growth suppressant in different microorganisms, setting them as ideal candidates for medical devices.

Quantum Dots. Similarly to metallic nanoparticles, quantum dots' (QDs) optical properties are size and shape tunable[26,27]. As the size of QD decreases the band gap increases (Figure 1.4.). For example, highly luminescent CdSe QDs are potential materials for use as optoelectronic devices, and in vitro and in vivo imagining and analyses. Due to exceptional photostability and bright emission, broad absorption and narrow emission bands and large two-photon absorption cross-section[29], QDs are seen as

ideal substitution to organic fluorophores. Functionalized with specific ligands, these bioconjugated QDs effectively bound to targeted cell membranes[30] pawing the road to use of quantum dots as excellent probes for detection and imaging of cells. The endocytosis[31] of QDs was reviewed by Parak et al. Hydrophilic QDs entered cell via endocytosis and aggregated inside the cytoplasm[32]. Conjugated Tat peptides with QDs were delivered inside human fibroblast cells and the nucleus of COS 1 cells[33]. These studies point into promising application of QDs as targeted drug delivery vehicles.
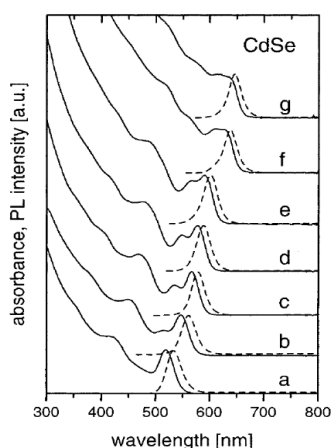
Figure 1.4. QD spectra. Absorption (full line) and emission spectra (dashed line) of different size QDs in range of 20-55 Å [26]. From Alivisatos, A. P. Semiconductor Clusters, Nanocrystals, and Quantum Dots. *Science* **271,** 933–937 (1996). Reprinted with permission from AAAS.

Carbon-based Nanoparticles. Owing to their unique physical and chemical properties like mechanical strength, thermal and electrical conductivity and optical properties, carbon based nanomaterials are finding increasing application in electronics and novel high-strength materials[34,35]. Carbon nanomaterials can be chemically functionalized which increases their solubility and makes them suitable for biomedical use. The most

common carbon nanomaterials are graphene, carbon nanotubes and fullerenes (Figure 1.5.).
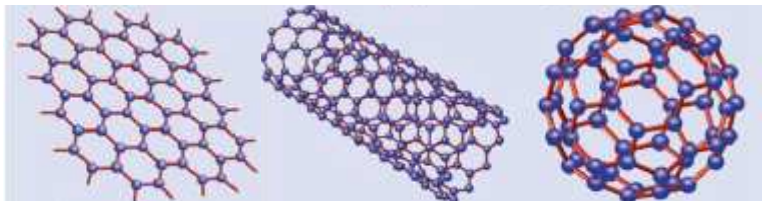
Figure 1.5. Graphene, carbon nanotube and fullerene[36]. Reprinted figure with permission from Castro Neto, A. H., Guinea, F., Peres, N. M. R., Novoselov, K. S. & Geim, A. K. The electronic properties of graphene. *Rev. Mod. Phys.* **81,** 109–162. Copyright 2009 by the American Physical Society.

Graphene is 2D allotrope[37] of carbon and first was isolated by Novoselov in 2004. Even though it is produced every time someone writes with pencil, no one expected graphene to exist in the free state and also, no tools existed to insulate one-atom thick layers among pencil debris[38]. Basically, graphene is made of carbon atoms arranged in honeycomb structure made out of hexagons (Figure 1.5.). Carbon atoms form σ and π bonds through sp^2 hybridization. The length of σ bond between two carbon atoms is about 1.42 Å and is responsible for robustness of the structure in all allotropes, while π orbitals due to strong tight-binding are contributing to strong collective effects, magnetism, and insulating behavior[39,40]. In biomedical applications, functionalized form of graphene, called graphene oxide (GO) is more used due to better suspension[41,42]. The intrinsic photoluminescence of GO is exploited for live cell imaging in the visible and near infrared[43]. Also, it was shown that doxorubicin, a widely used cancer drug, can be loaded

to graphene oxide and delivered to tumor cells[44] (Figure 1.6.). GO displays advantageous characteristics to be used as biosensing platform due to easy functionalization with biomolecules and tunable electronic properties that can make this functionalized GO to be insulator, semiconductor or semi-metal[45]. The hexagonal lattice of GO interacts strongly with aromatic structures in nucleotides through π-π stacking[46,47], also studies reported absorption of peptide onto GO surface[48–50]. As the oxidation process causes defects in planar structure of GO, leading to disruption of sp^2-bonded carbon atoms in 2D lattice, GO possesses a recombination electron-hole pairs localized in sp^2 region of a sp^3 matrix, displaying photoluminescence characteristic[51].
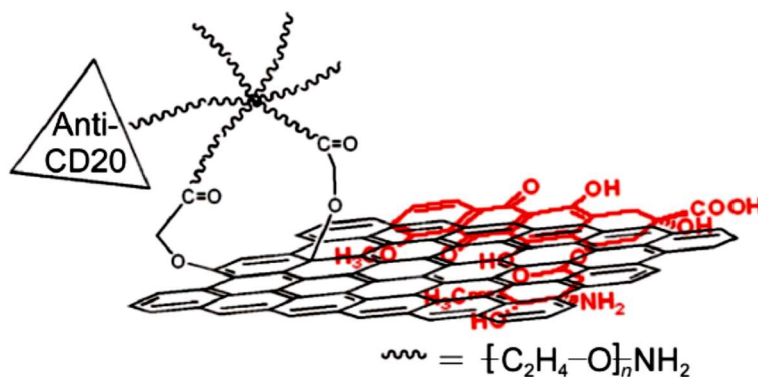
Figure 1.6. A scheme showing loading of doxorubicin (red) onto graphene-oxide-PEG-Rituxan[44]

Depending on the reduction processes, fluorescence emission spectra can be changed, opening opportunities for tailored optoelectronic properties[45]. Having in mind these GO characteristics, graphene oxide is finding use as a FRET donor, and owing to its

semi-metallic properties it can be used as FRET acceptor as well and being applied as biosensing platform in biomedicine[45].

Carbon nanotubes are tubular structures with sp^2 hybridized carbon atoms. The carbon nanotubes (CNT) can consist of one (single walled CNT) up to hundreds (multiwalled CNT) concentric carbon shells[52] adjacently separated by 0.34 nm. The quasy-one dimensional structure is responsible for high Young's module and tensile strength, so these materials are used in novel composite materials[53,54]. Also, depending on their structural parameters, CNT can be metallic or semiconducting, making them ideal candidates for novel electronic devices, including field-effect transistors (FETs), single electron transistors and rectifying diodes[55]. Recently they are investigated as possible hydrogen energy storage units[56]. Application of CNT in biomedical field is recently emerging[57], ranging from use of CNTs as DNA and protein biosensors, ion channel blockers, biocatalysts and in tissue engineering[58–62]. They are being used to specifically detect antibodies[63] and similarly DNA[58] when appropriately functionalized. Due to their large surface area, CNT can be loaded with different drugs and specifically delivered to targeted cell, which is necessary for efficient tumor treatment[64–66]. A study showed that application of drug loaded CNTs onto specific cells was more efficient compared when just free drug was used[67]. All these examples corroborate promising application of CNTs in biomedical and pharmaceutical industry.

Kroto et al. discovered fullerenes in 1985 and in 1996 this discovery led to Nobel Prize to Kroto, Curley and Smalley. Fullerene family is composed of carbon atoms forming ellipsoid, tube or spheres. The spherical fullerenes are also called buckyballs.

The C60 molecules possess high symmetry and are one of the most symmetric molecules known[68]. They are made of 20 hexagons and 12 pentagons and all double bonds are conjugated. Despite aromatic character of the bonds, C60 behaves more like electron-deficient alkanes[69]. These molecules are highly hydrophobic and tend to aggregate in solution[70], thereby non-conjugated fullerenes are of limited use in biological systems. Luckily, there are several developed techniques to increase fullerene solubility like encapsulations in special carriers-micelles and liposomes, calixarens , cyclodextrins or polyvinylpyrrolidon , then suspensions with the help of co-solvents and finally chemical functionalization to decrease hydrophobicity with addition of poly-hydroxyls, amino and carboxyl acids or amphiphilic polymers[71–77]. It has been shown by Friedman et al. and others that fullerene derivatives can inhibit HIV-1 replication by fitting into cavity of HIV-1 protease[78–80]. Further, Shoji et al. showed that fullerene derivatives have inhibitory effects on influenza A virus by interacting with PA subunit of H1N1 and H5N1 protease[81]. Fullerenes were recognized as excellent sensitizers for production of singlet oxygen[82]. This property of fullerenes was exploited to cleave DNA by photo activation[83]. Due to its lowest unoccupied molecular orbital and conjugated double bonds, fullerene are ideal electron acceptors, making an attack on free radicals very likely. This feature makes fullerenes radical scavengers[84] and when localized inside the cell mitochondrion, where in the case of diseases free radical species are produced, fullerene can act as radical sponge and have protective properties for the cell[85]. By attaching hydrophilic groups to the fullerene surface and making them water soluble, these carbon nanostructures become capable of drug or gene delivery to the cells. Fullerene size is

about 1nm, and studies by Isobe et al. and Nakamura et.al showed that fullerene can enter COS-1 cells with comparable or better efficiency compared to common used lipid vectors[86]. Foley et al. demonstrated crossing of fullerenes though cell membrane and binding to mitochondria[87]. Prospective use of fullerene is seen in cosmetic industry, owing to binding of fullerene to collagen and making collagen fibers stiffer[88], opening the doors to slowing down aging of the skin. An example of high definition TEM image of functionalized fullerene is shown in Figure 1.7.
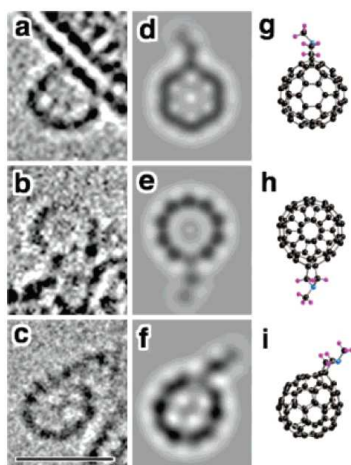
Figure 1.7. HRTEM images of functionalized fullerenes (different rotation angle view a-c) d-f simulated TEM images and g-i schematic image[89]. Reprinted with permission from Liu, Z., Suenaga, K. & Iijima, S. Imaging the Structure of an Individual C60 Fullerene Molecule and its Deformation Process Using HRTEM with Atomic Sensitivity. *J. Am. Chem. Soc.* **129,** 6666–6667. Copyright 2007 American Chemical Society.

3. Nanomaterials in biological milieu: Transformation and Toxic Effects

Enormous growth in production and application of nanomaterials raised concerns about possible toxic effect of these materials onto the environment and the biological system.

The use of nanomaterials in cosmetics, food production, nanomedicine, detergents raises concern that eventually they can end up released into the freshwater or marine ecosystems through sewage systems, and latter through food chain or inhalation end up in the biosystem[90–92] as illustrated in Figure 1.8.
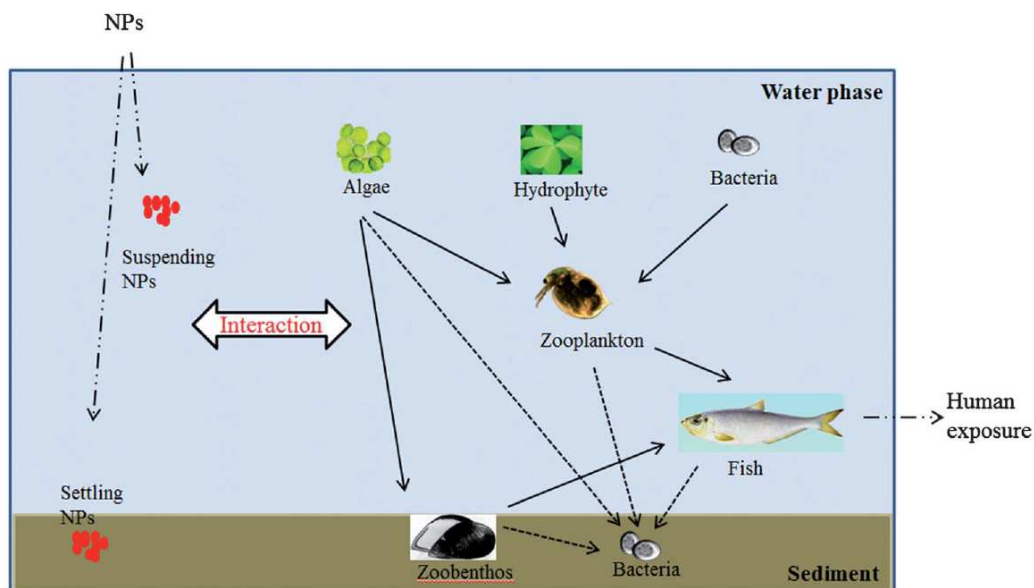
Figure 1.8.   Illustration of food chain routes that could lead to human exposure to nanoparticles. Adapted with permission[93] of the Royal Society of Chemistry.

Once nanoparticles get into the biological environment their surface gets coated with various biomolecules, forming so called protein corona[94] (Figure 1.9.). It's rather protein corona than the pristine nanoparticles that determines the fate of nanoparticle in biosystem [94]. Thus it is very important to characterize affinities, rates and stoichiometry of protein binding to the NPs surface in order to understand nanomaterials interaction with cells and its machinery. The rates at which proteins bind to nanoparticle surface can define its interaction with cell receptors. Tightly bound proteins with slow exchange rates

(hard corona) might follow the nanoparticle as it undergoes endocytosis, while loosely attached proteins could be replaced during this process with proteins found in cytoplasm determining the interaction between NPs and the cell environment. The lifetime of protein-nanoparticle complexes depends on the specific protein and nanoparticle type, but typically ranges from 100 s to many hours[95–99]. Cedervall et al. in study of protein corona formation between human serum albumin (HSA) and copolymer N-isopropylacrlamide (NIPAM): N-tert-butylacrylamide (BAM) nanoparticles, revealed stoichiometry dependence on hydrophobicity and size[94]. Copolymer particles with higher BAM content are more hydrophobic. In this study 85:15, 65:35 and 50:50 NIPAM:BAM NPs are used. Utilizing isothermal titration calorimetry (ITC) they showed that the number of proteins bound to more hydrophilic NPs (85:15) was about 60 while for hydrophobic one was about 350 (50:50), suggesting higher stoichiometric ratio for more hydrophobic particles. Also, as they increased the size of BPs from 70nm to 200nm they observed increase in bound protein to 980 and 5400 for 85:15 and 50:50 NIPAM:BAM NPs, respectively. Also, surface plasmon reso-
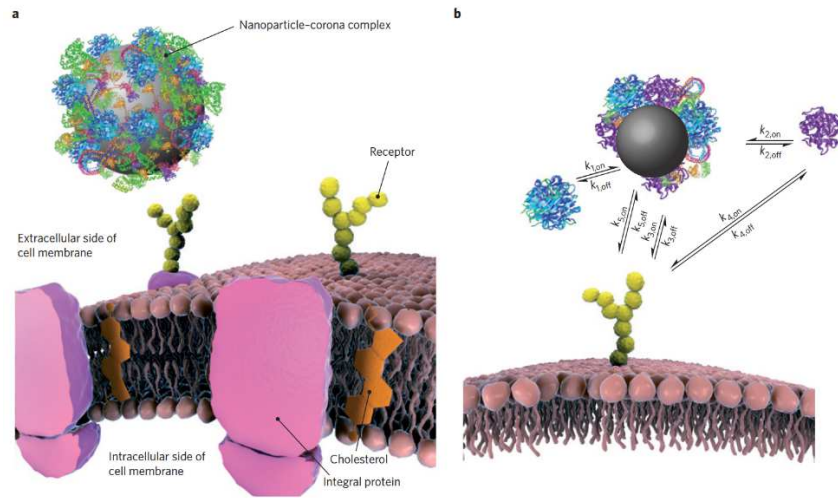
Figure 1.9. Nanoparticle-corona complex a) and relevant processes b) for NP interacting with receptor. Reprinted by permission from Macmillan Publishers Ltd: Nature Nanotechnology[100], copyright (2012)

nance (SPR Figure 1.10.) and size exclusion chromatography revealed that protein exchange rates depend om hydrophobicity.
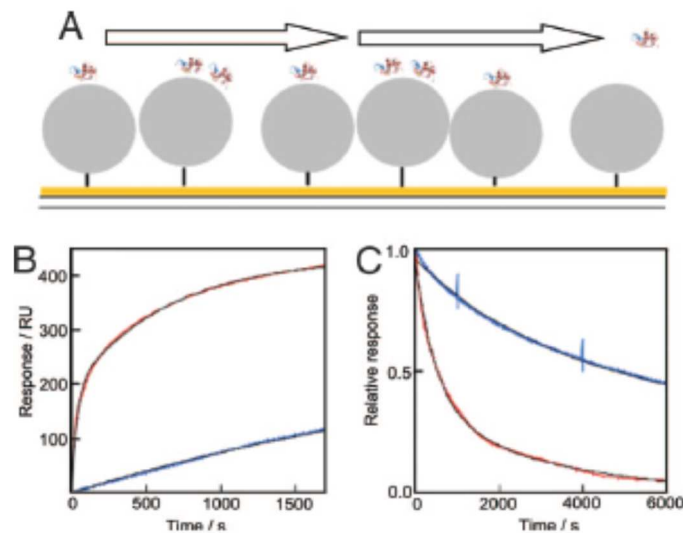
Figure 1.10. SPR A) Cartoon of a gold surface and associated protein over buffer is flown. B) and C) SPR data of plasma proteins injected overn70 nm 85:15 (blue) and 50:50 (red)

NIPAM:BAM NPs for 30 min B) and 24h C) [94]. Copyright © by the National Academy of Sciences HSA residence time on more hydrophilic particles is longer, compared to the hydrophobic ones. Further, they repeated experiment with fibrinogen, other blood plasma protein, and results showed that fibrinogen residence time on NPs is longer.

Additional experiments with blood plasma that consists of more than 3700 different proteins and NIPAM:BAM nanoparticles were conducted. It was found that several plasma proteins preferentially bound to the surface of copolymer nanoparticles and that at least six of them elute faster than HSA, implying slower exchange with the NPs surface. After, three cycle centrifugation of 20 min, albumin and fibrinogen SDS/PAGE signatures weren't observed, while some other plasma proteins (175, 75, 50, 35 and 28 kDa) were identified to bind the surface. Depending on the protein, binding amount was or wasn't dependent on nanoparticle's hydrophobicity. This study uncovered complex mechanism of nanoparticle-protein interaction, which depends on the protein type, nanoparticle surface properties and that some proteins form transient complexes with nanoparticles and the final corona composition is determined by competitive binding. Centrifugation experiments in above mentioned study, suggested two types of protein corona: soft corona, in which protein dissociates from nanoparticle surface and is in equilibrium with free protein in solution and hard corona, tightly bound protein with very slow dissociation rates. Milani et al. studied formation of transferrin protein corona using fluorescence correlation spectroscopy (FCS) methods[101]. They observed genesis of monolayer protein corona, up to nanoparticle surface saturation, followed by formation of the second protein layer. Protein that formed first monolayer is found to be tightly

absorbed to nanoparticle surface and formed hard corona, while weakly bound second monolayer formed soft corona. Further, this study noted two different adsorption processes, one describing protein adsorption to surface through protein-surface interaction and the second process involved in formation of the second layer through protein-protein interactions. When other plasma proteins were introduced together with already formed transferrin-nanoparticle corona, transferrin from the second layer, labeled as soft corona was replaced by plasma (Figure 1.11.).
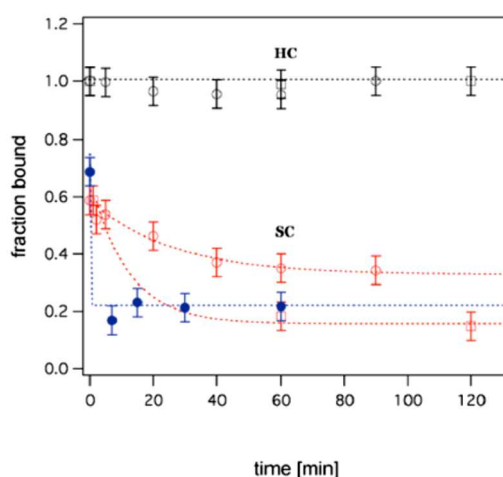
Figure 1.11. Competitive unbinding: Hard corona (HC) (black circle 5% and black squares 10 % added plasma); red, blue circles (5% added plasma on two different types of NPs) and red squares (10 % added   plasma) representing soft corona (SC)[101]. Reprinted with permission from Milani, S. et al. "Reversible versus Irreversible Binding of Transferrin to Polystyrene Nanoparticles: Soft and Hard Corona". Copyright 2012 American Chemical Society.

Transportation of nanoparticles through food chain and impact of polystyrene nanoparticles onto fish behavior and fat metabolism[90] was investigated by Cedervall et al.

Polystyrene nanoparticles of 24 nm size were fed to an algal culture, which then was filtered and fed to herbivorous zooplankton (Daphnia). After 24 h the zooplankton was washed, so residual surface bound nanoparticles were removed and then the zooplankton was given to top consumer, fish (Figure 1.12.). The control food chain was operated in the same way, except that no nanoparticles were given. It was noticed that nanoparticle fed test fish let Daphnia swim out their mouth and in general exhibited lethargic behavior. Polystyrene nanoparticles bind several apolipoproteins form human plasma[102] and one of them is apoA-I. ApoA-I and HDL proteins are essential for fat metabolism. It is likely that polystyrene nanoparticles travelled through intestine wall and entered blood stream, binding apoA-I and HDL proteins and influencing fat metabolism. After comparing triglycerides: cholesterol ratios of test and control fish, it was observed that after 14 days this ratio remain the same, but after 22 days drop was seen in the control, while minor changes in the test. Also, after 22 days increased concentration of cholesterol in liver was observed. Fish was fed with limited amount of zooplankton, so the drop in weight was expected. A significant weight loss was seen in control fish, while in the test fish weight remained the same, implying that nanoparticles interfered with metabolic process and blocked utilization of energy reserves. This study showed that protein corona formation can have devastating effect on metabolism of the top consumer and as well influence its behavior, leading to potential hazardous effect on ecosystem functioning.
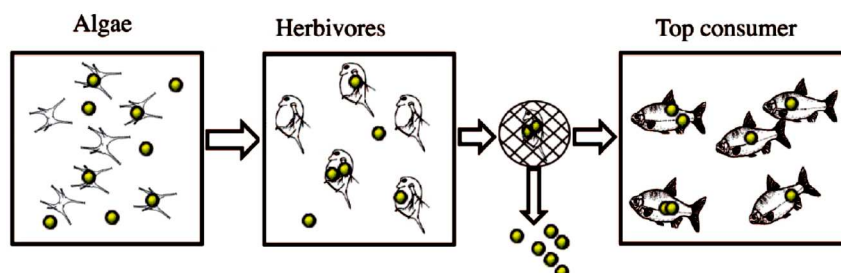
Figure 1.12. Food Chain. Scheme depicting process of feeding zooplankton with 24nm polystyrene NPS, and then after zooplankton was washed, it was given to top consumer-fish[90]

Lin et al. showed that C_{70} and multiwalled carbon nanotubes (MWCNT) can be taken and transferred to next generation in rice plants[91]. They saw that nanoparticles were found in roots, stems and leaves of the two weeks old first generation rice plants and later in seeds. The appearance of nanoparticles in the zones of plant vascular system suggests that uptake of NPs happened simultaneously with the uptake of water and nutrients in the xylem. Furthermore, no nanoparticles were detected on roots of mature plants suggesting powerful transport of nanomaterials from the roots to the leaves. Also in the leaves of the second generation plants C_{70} nanoparticles were observed, indicating transmission of nanoparticles from seeds of the first generation to the next one. Contrary to C_{70} uptake of MWCNT was insignificant at concentrations of 20 to 800 mg L^{-1} with some observed aggregates near the vascular system. At concentrations of 400 mg L^{-1} of C_{70} flowering of the plant was delayed by 1 month and seed setting rate reduced by 4.6%. At high concentration of C_{70} and therefore its aggregation in the vascular system of the plant, it is expected that these NPS would interfere with normal uptake of water and nutrients

necessary for the plant growth and in that way hinder its development. Similarly, with high concentration of MWCNT (400 mg L^{-1}) due to NPs induced blockage of the roots leading to the hindered uptake of water or nutrients, flowering of the plant was delayed for 1 month and the seed setting rate reduced for 10.5%. These two studies, one dealing with impact of nanoparticles on fauna and the other on flora uncover hazardous potential of nanoparticles onto the ecosystem and their propagation through the food chain, finally reaching human biosystem.

**Nanotoxicty**. In the next couple of paragraphs, I will briefly describe toxic effects of different nanoparticles in different cell structures and mammals. Protein adsorption to nanoparticle surface can mediate the uptake of nanoparticles through receptor mediated endocytosis[103] (RME). Influence of nanoparticle surface charge, functional groups, protein corona, size and intrinsic physico-chemical properties would be assessed in connection to potential toxic effects onto cell cultures.

Review by Alkilany et al. summarized the state of the toxic studies on gold nanoparticles done done by 2010[104]. In studies carried out, gold nanoparticles of sizes 4, 12, and 18 nm in diameter and capped with different agents showed non-toxic effect to human leukemia cell line[105]. Another group obtained similar results in cytotoxic study on influence of 3.5 nm onto immune system cell lines[106]. Citrate capped gold nanoparticles didn't show cytotoxic effects on dendritic cells, nor changed their phenotype[107]. On contrary, Goodman et al. found that cationic gold nanospheres of 2 nm diameter induced toxic effect on COS-1 cells at concentrations of 0.38-3 μM after 24 h incubation, while

the same nanoparticles with negative charge didn't. These results were explained through electrostatic interaction of cationic nanoparticles with negatively charged cell membrane[108]. Pan et al. investigated how nanoparticle size affects cytotoxicity in HeLa, SK-Mel-28 (melanoma cell line), L929 (mouse fibroblast cell line) and j774A1 (macrophage cell line) cell lines. In this study they found that 1.4 nm gold nanospheres (up to 5.6 μM after 72h incubation) induced cell necrosis, oxidative stress and mitochondrial damage in all cell lines. These effects weren't seen in the case of 15 nm diameter nanospheres[109,110]. Further it was concluded through studies of Patra et al. that some citrate capped gold nanoparticles were found toxic to a human lung carcinoma cells, but not to a human liver carcinoma cells[111]. Asharani et al. compared cytotoxicity of silver (5-35nm), gold (15-35nm) and platinum (3-10nm) nanoparticles capped by polyvinyl alcohol (PVA) on developing zebra fish embryos[112]. Gold nanoparticles had the least toxic effect in this study, not influencing hatching, mortality or cardiovascular system functioning. In study on effect of gold nanoparticle shape and surface functionalization onto epithelial cells, it was found that with the same functionalized group (coated with CTAB) rod shaped nanoparticles were less toxic than spherical ones[113]. The higher toxicity of gold nanospheres was attributed due to the higher CTAB translocation upon entering the cell compared to nanorods. These results suggest that cell type-nanoparticle specific interactions play the roll in toxicity

Silver nanoparticles (20 and 40 nm functionalized with small peptide) were found to cause toxicity in THP-1-derived human macrophages[114]. Smaller size NPs were more toxic compared to larger ones and after 48 h sharp decrease in cell viability was observed

at 18 µg/ml concentration of 20 nm AgNPs and 30 µg/ml concentration of 40 nm AgNPs. Nanoparticles were efficiently taken by macrophages where they exerted oxidative stress and through reactive oxidative species (ROS) damaged the cell. Other study of 10 nm AgNP with different coatings (citrate, PVP) caused DNA damage in human lung cells[115]. A lot of carried studies identified AgNP as a potential source of cytotoxicity[116–120].

Cytotoxicity of carbon nanomaterials was observed as well. Pulmonary toxicity of single-walled carbon nanotubes induced lethargy, weight loss and death in mice[121]. Similarly, multiwalled carbon nanotubes induced mesothelioma in mice[122]. Studies on graphene oxide discovered it's toxicity onto different cell lines[123]. Also depending on the hydroxylation, pristine and hydroxyl functionalized fullerenes exhibited toxic effect onto human dermal fibroblast and human liver carcinoma cells[124]. While pristine fullerenes exerted oxidative stress onto the cell and induced cell necrosis, hydroxylated fullerenes triggered cell apoptosis.

Also, recently it was found that nanoparticles interfere with protein aggregation. Formation of protein aggregates is considered to lead to Alzheimer's, Huntington's, Parkinson's, Creutzfeldt-Jacobs (mad cow) disease[125–127]. Depending on the type of nanoparticle and protein involved, it was found that some nanoparticles promote, while other hinder protein aggregation[128–134], leading to possible application of nanomaterials in protein aggregation remediation.

4. Understanding interactions of nanoparticles with environmental and biological system using both experimental and computational approaches.

Understanding the protein corona formation and transformation through nanoparticle-protein interaction is of the crucial importance in order to predict the fate of nanomaterials in biological systems. My research predominantly focused onto the study of protein corona genesis and its implications onto the protein structure and binding dynamics. My first study, presented in Chapter 2, delineated physical properties of fibrinogen protein corona on single-walled and multiwalled nanotubes. It identified distinct morphology of protein corona on SWCNT and MWCNT. Further, it investigated the interaction of protein corona with HT-29 cell's membrane and itss translocation upon the nanoparticle internalization into the cell. Although, this and the other experimental studies provided insights on formation, and size of protein corona[135], and protein composition on the nanoparticle surface[136], due to limited instrumental resolution, the molecular details of protein-nanoparticle interaction are poorly understood. Utilizing computational modeling together with the experiment, my research will try to bridge the gap between experimental observations and the molecular systems of the interest. Traditional molecular dynamics approaches already can accurately describe the system of proteins and nanoparticles[137–140], but lack reaching the timescales necessary for description of large systems[141,142]. This obstacle can be surpassed by employing coarse grained models and using simplified force fields[143–148], but they have limited predictive power on studying interactions between nanoparticles and specific protein.

In Chapter 3 we performed molecular dynamics study on formation of ubiquitin-silver nanoparticle protein corona. There we showed that our modeling can capture and reach length scales necessary for protein corona formation with high agreement to experimental studies. Further, study on ubiquitin-fullerene derivatives corona is outlined in Chapter 4 with emphasis on influence of nanoparticle surface chemistry on specific binding and protein misfolding. Studies in Chapter 3 and Chapter 4 investigated systems with one kind of protein, while in Chapter 5, I investigated protein corona evolution when different biomolecules compete on the nanoparticle surface. Finally, effects of nanoparticle surface on protein aggregation will be described in Chapter 6, specifically focusing on protein aggregation on nanoparticle surface and its implications onto the aggregation in the bulk. Conclusion will be given in Chapter 7.

CHAPTER 2

FORMATION AND CELL TRANSLOCATION OF FIBRINOGEN-CARBON NANOTUBES CORONA

1. Introduction

Carbon-based nanomaterials have been studied extensively over the past two decades for their unique physical properties and vast potential in electronics, imaging, sensing, biotechnology, and environmental remediation. Carbon nanotubes (CNTs), a major class of carbon-based nanomaterials, are especially attractive for biological and medicinal applications owing to their large surface area, high aspect ratio, and simplicity for accommodating chemical groups and drug loads[149]. However, integrating carbon nanomaterials with biological systems must first address the inherently poor solubility and biocompatibility of the engineered materials, on molecular, cellular and whole organism levels[135,150].

The solubility and biocompatibility of carbon-based nanomaterials may be afforded or enhanced through specific surface functionalization or nonspecific adsorption of proteins, lipids, amino acids, and nucleic acids[151–155]. Alternatively to such purposeful surface modifications, nanoparticles (NPs) voluntarily assume the form of a NP-protein "corona" upon entering living systems[156], resulting from their surface adsorption by plasma proteins and other biomolecular species. Naturally, understanding the formation of NP-protein corona has become a focused area of study due to its great relevance to

delineating the fate and toxicity as well as facilitating the biological and medicinal applications of nanomaterials[157].

The currently accepted paradigm assumes that the formation of NP-protein corona depends upon the physicochemical properties of the NPs (surface charge, coating, shape, roughness, and reactivity), the solvent (pH, ionic strength, and temperature), and the proteins (amphiphilicity, charge, pKa, chemical composition, and folding dynamics)[157–159]. In addition, plasma proteins may exhibit short ("soft") or long-term ("hard") residence times on their NP substrates[101], derived from the cooperativity (the Vroman effect[160], folding/unfolding) between the proteins convolved with the protein affinity for the NP substrates mediated by electrostatic and hydrophobic interactions, *van der Waals* forces, and hydrogen bonding.

In consideration of the vast biological and medicinal potentials of carbon-based nanomaterials, we have examined in the current study the binding of both single-walled and multiwalled CNTs (SWCNTs and MWCNTs) with fibrinogen (FBI), a major class of plasma glycoprotein that is essential for the coagulation of blood. It is shown through this study that the formation and stability of CNT-FBI coronas correlate with the differential surface areas of the two types of CNTs, as indicated by our UV-vis spectrophotometry and electron and fluorescence measurements. In addition, we have determined that the binding of fluorescently labeled FBI onto CNTs induced static (and possibly dark) quenching of the protein fluorescence. Utilizing the energy transfer between labeled FBI and CNTs (Fig. 4.1, left panel scheme), we have shown that CNT-FBI coronas could dissociate upon cell translocation, likely as a result of the different affinities of the

proteins and the nanostructures for the membrane bilayers. The knowledge derived from this biophysical study complements the existing proteomic, thermodynamic, and chromatographic studies of NP-protein corona[101,136,157,159,161,162], and may benefit both *in vitro* and *in vivo* evaluations of biological responses to intentionally administered or accidentally released nanomaterials.

SWCNTs (diameter: 1.4 nm, length: 0.5-3 μm, 5% impurities) and MWCNTs (OD: 40-70 nm, ID: 5-40 nm, length: 0.5-2 μm) were purchased from Carbon Nanotechnologies and Sigma. Bovine plasma FBI (termed as "unlabeled FBI", MW: 330kDa) and Alexa Fluor 546-labeled human plasma FBI (termed as "labeled FBI", ~15 dyes per FBI, Ex/Em: 558/573 nm) were received from Sigma and Invitrogen. The surface areas of SWCNTs and MWCNTs (in powder form) were derived from the Brunauer-Emmett-Teller (BET) equation[163] and the Barrett-Joyner-Halenda (BJH) method[164] as 855 and 104 m^2/g, respectively, using a physisorption analyzer (Micromeritics ASAP 2010).

2. Results and Discussion

The formation of CNT-FBI coronas was first visualized by scanning electron microscopy (SEM) imaging (Fig. 5.1, right panels). Specifically, CNTs and unlabeled FBI were mixed with Milli-Q water to final concentrations of 0.3 and 0.4 mg/mL respectively and incubated overnight. The CNT-FBI samples were then deposited onto aluminum substrates and air-dried. A Hummer 6.2 (Anatech) sputter was used to pre-coat the samples with a 2-4 nm layer of platinum for 1 min (pressure: 80 milli-torr, voltage: 15

mA). SEM imaging of the CNT-FBI protein coronas was then performed using a Hitachi S4800 electron microscope, at accelerating voltages of 10-15 kV. FBI coated both the SWCNTs and MWCNTs fully, and especially in the case of MWCNTs the protein agglomeration on the nanotube surfaces appeared complex in morphology. This is likely due to the bundling of the SWCNTs (Fig. 5.1, SWCNTs control), whose surface roughness and grooves could promote the predominantly axial orientations of the tubular FBI. In comparison, the larger and flatter MWCNT surfaces should be less restrictive for the binding of the protein.
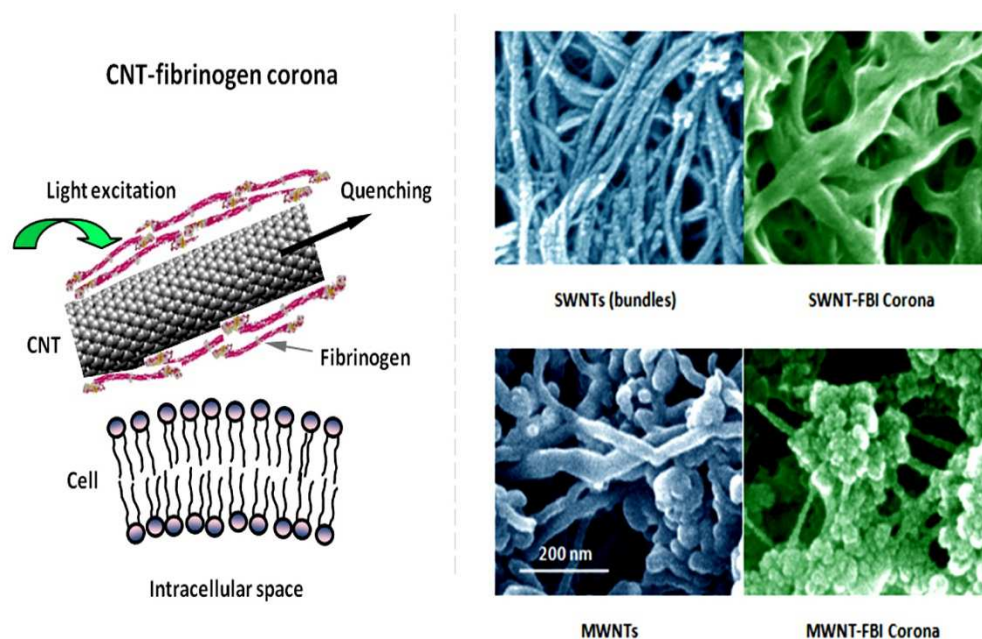
Figure 5.1. Fibrinogen corona. (Left panel) Schematic of the present study, showing quenching of FBI fluorescence as a result of energy transfer from the proteins to their CNT substrate and translocation of CNT-FBI across a cell membrane. (Right panel) SEM images of SWCNT bundles, SWCNT-FBI coronas (top panels), MWCNTs, and MWCNT-FBI coronas (bottom panels). Scale bar: 200 nm for all panels.

The stabilities of the CNT-FBI coronas were characterized by a Cary 300 BIO spectrophotometer (Varian). SWCNTs and MWCNTs were mixed separately with unlabeled FBI in Milli-Q water (pH 6.5) to render final concentrations of 0.5 mg/mL for both types of the CNTs and 2.5 mg/mL for the protein, respectively. The absorbance of the CNT-FBI mixtures was measured at 280 nm, corresponding to the wavelength where the tryptophan residues in FBI exhibited a peak absorbance. The absorbance measurement was conducted for 10 h, at a time interval of 30 min. As shown in Fig. 5.2 a, the absorbance dropped exponentially until stabilized after ~400 min for the SWCNT-FBI sample, while it remained very stable for the MWCNT-FBI sample over the entire course of 10 h. This result suggests that the SWCNT-FBI coronas were "softer" than the MWCNT-FBI, a proposition also corroborated by our analysis below. In addition to *van der Waals* force, hydrophobic interaction, as well as pi-stacking which could underlie the formation of CNT-FBI coronas, FBI could also initiate hydrogen bonding between adjacent CNT-FBI coronas. In the case of SWCNTs such inter-corona interaction could further destabilize the protein coating to induce precipitation.

The two different trends of protein absorbance in Fig. 5.2a can be analyzed using the Mason-Weaver differential equation[165]: $\dfrac{\partial c}{\partial t} = D\dfrac{\partial^2 c}{\partial t^2} + sg\dfrac{\partial c}{\partial z}$, where c is concentration of the solute (i.e., the CNT-FBI corona), D and s are the solute diffusion constant and sedimentation coefficient, z is a length parameter, and g is the acceleration of gravity. Based on the fitted exponents of -0.007 (for SWCNTs) and 0 (for MWCNTs)

in Fig. 5.2 a, the value of *4D/(sg)²* was calculated as 136.7 min for SWCNTs and infinity

for MWCNTs. Assuming m_0 and m_b are the actual and buoyant mass of the solute, ρ_f and

ρ_0 the densities of the solute and water, k_b the Boltzmann constant, and T the temperature,

and evoking equations $m_b = m_0(1 - \rho_f / \rho_0)$ and $s / D = m_b / k_b T$ derived from the Einstein

relation we estimate that SWCNT-FBI possessed an effective density of 1.36 g/cm³ while

MWCNT-FBI assumed an effective density approximately equal to that of water. Since

the density of SWCNTs is ~1.4 times that of water[166] and is only slightly higher than that

of SWCNT-FBI, we conclude that SWCNT bundles were coated with thin layers of FBI

to elicit a poor stability in water. In contrast, our analysis implies that MWCNTs were

adsorbed with multilayers of the protein to render a hard corona.

Fluorescence spectroscopy was utilized to yield more insight on the binding of

CNTs and FBI. Specifically, 3 mg of SWCNTs and MWCNTs were each added to 3 mL

of Milli-Q water and bath sonicated for 1 h. The CNTs were then mixed individually with

66.7 µL of the labeled-FBI (1.5 mg/mL) and Milli-Q water to yield samples containing

10-80 µg/mL of SWCNTs, 100-800 µg/mL of MWCNTs, and 100 µg/mL of labeled FBI.

The CNT-labeled FBI samples were then bath sonicated (Precision, Thermo) for 15 min

and incubated for 1 h on a rotator. After that the CNT-labeled FBI mixtures were

centrifuged at 12,100 RCF (13,400 RPM) for 15 min and supernatants containing free,

labeled FBI molecules were collected. Fluorescence intensities (Ex/Em: 558 nm/565-585

nm) of the supernatants were acquired using a Cary Eclipse spectrofluorometer (Varian).
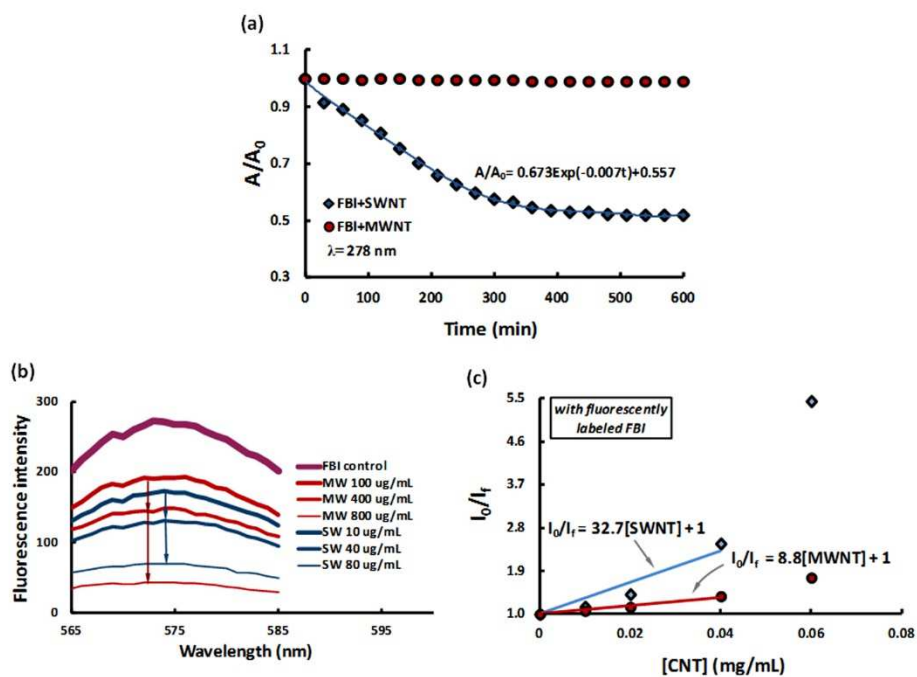
Figure 5.2. Spectroscopic characterization of FBI corona. (a) Normalized absorbance curves showing the stability of CNT-FBI coronas for both SWCNTs (blue diamonds) and MWCNTs (red circles) over 10 h. (b) Fluorescence intensities of free, labeled FBI supernatants obtained from pelleting SWCNT-FBI (blue curves, 10, 40, and 80 μg/mL of the SWCNTs) and MWCNT-FBI coronas (red curves, 100, 400, and 800 μg/mL of the MWCNTs). The fluorescence intensities decreased with increased nanotube concentration for both samples. (c) Stern-Volmer plots show quenching coefficients of 32.7 and 8.8 for SWCNT-FBI and MWCNT-FBI coronas, respectively. I_0 and I_f: fluorescence intensities of the labeled FBI control and the CNT-labeled FBI mixture, respectively. CNT concentrations: 0.02 to 0.08 mg/mL.

Compared with the control, the fluorescence intensities of all CNT-labeled FBI samples decreased (Fig. 5.2 b) as a result of CNT-FBI corona formation. Such fluorescence quenching can be attributed to the energy transfer between the labeled FBI (donor) upon excitation and the CNTs (acceptor) upon their binding with the proteins.

31

This energy transfer was efficient for SWCNTs because their second van Hove absorption transitions (i.e., 500-900 nm)[167,168] coincided with the emission of the Alexa Fluor 546 dye. Based on geometrical argument and our surface area measurement, the adsorbing capability of SWCNTs was estimated as one order of magnitude higher than that of MWCNTs per unit mass. Indeed, the fluorescence intensities were comparable between SWCNT and the 10× more concentrated MWCNT samples, showing a good correlation between protein adsorption capacity and surface area of the CNTs.

The peak fluorescence intensities at 572 nm were plotted for the CNT-labeled FBI samples and fitted using the Stern-Volmer equation: $I_0/I_f = 1 + K_{SV}[CNT]$, here I_0 and I_f are the fluorescence intensities of the labeled FBI (control) and CNT-labeled FBI mixture respectively, K_{SV} is the Stern-Volmer quenching coefficient, and $[CNT]$ is the concentration of the nanotubes. The Stern-Volmer plots appeared linear for both SWCNT-FBI and MWCNT-FBI samples at lower CNT concentrations (first 4 data points in Fig. 5.2 c), indicating a single quenching mechanism. At higher CNT concentrations, however, both curves deviated from linearity to denote occurrence of additional quenching mechanisms. Since collision between CNTs and FBI should occur more frequently at high concentrations the linear Stern-Volmer plots at the low CNT concentrations were attributed to static quenching. Though not substantiated in this study CNTs may also absorb light analogously to blackbody[169]. In our experiment, the molar mass ratio of the SWCNTs to MWCNTs was 1:418, and therefore the ratio of the Stern-Volmer coefficients for the SWCNT-FBI and MWCNT-FBI samples was 32.7:(8.8×418)=1:112. This analysis revealed that MWCNTs were far more efficient

quenchers than SWCNTs, whose smaller diameter and greater curvature were less favorable for the adsorption and alignment of the tubular FBI molecules.

The fluorescence quenching upon corona formation was utilized to examine the stability of CNT-FBI *in vitro*. For this purpose, HT-29 human colonic adenocarcinoma cell lines were cultured in DMEM with 1% penicillin streptomycin, 1% sodium pyruvate, and 10% fetal bovine serum. Approximately 5,000 cells were seeded in each well of a chambered glass slide and allowed to attach overnight at 37°C with 5% CO_2. The culture medium was then replaced with phosphate buffered saline (PBS) and CNTs coated with purified labeled FBI (free proteins removed by centrifugation) and added in each well to obtain concentrations of 1.25 and 12.5 μg/mL for the SWCNTs and the MWCNTs, respectively. This mass concentration ratio of 1:10 was to ensure the same amount of labeled FBI coated on the two types of nanotubes. The CNT-FBI coronas were allowed to incubate with cells for 2 h, followed by washing and replacing with fresh PBS prior to imaging.

As shown in Fig. 5.3, the FBI fluorescence is largely quenched in both panels (c) and (d), indicating CNT-FBI corona formation for both SWCNTs and MWCNTs. Cell adsorption of SWCNT-FBI and fluorescence recovery of FBI in intracellular space were evident (Fig. 5.3 e, arrows), suggesting dissociation of SWCNTs and FBI post membrane translocation. The isoelectric point of FBI is 5.5[170], and therefore the proteins were slightly positively charged when stored/processed in endosomes and lysosomes (~pH 4.5) and slightly negatively charged when located in cytosol (~pH 7.2). Since the SWCNT surfaces were charge neutral, changes in pH in the intra- and extracellular environment

should not drastically impact the binding of SWCNT-FBI. The dissociation of SWCNTs and FBI is therefore attributed to their differential affinities for the amphiphilic cell membranes.

Pronounced cell adsorption of MWCNT-FBI and recovery of FBI fluorescence in the extracellular space were observed, but minimal fluorescence was seen in the intracellular space perhaps due to the high energy cost for MWCNT endocytosis (Fig. 5.3 f). In addition, cell damage (from elongated to round shapes) was more apparent for MWCNTs than SWCNTs (Figs. 5.3 f vs. 5.3 e), likely due to the higher dosage and the toxicity associated with the MWCNTs[171].
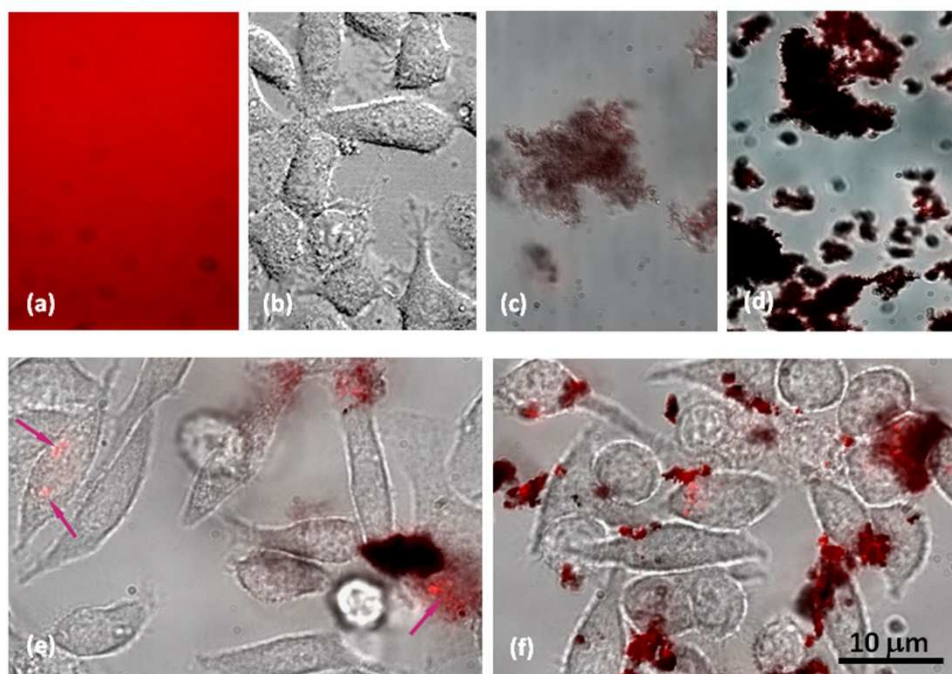
Figure 5.3. HT-29 cell uptake of CNT-FBI coronas overlaid from bright field and confocal fluorescence images. (a, b) Controls of labeled FBI fluorescence and HT-29 cells. (c, d) Controls of SWCNT-FBI and MWCNT-FBI showing fluorescence quenching. (e) Cell adsorption of SWCNT-FBI and FBI fluorescence recovery in the intracellular space (arrows). (f) Pronounced

cell adsorption and dissociation of MWCNT-FBI in the extracellular space indicated by fluorescence recovery. Cell damage induced by MWCNTs is evident. Scale bar: 10 μm for all images.

3. Conclusion

In short, we have examined the formation and stability of CNT-FBI coronas in the aqueous phase and *in vitro*. The binding between CNTs and FBI is consistent with the high hydrophobic and aromatic moieties of both the protein and the nanotubes, and agrees with the *in sillico* studies involving similar systems[172–174]. The differential "hardness" and stability of the SWCNT-FBI and MWCNT-FBI coronas were analyzed based on the concept of buoyant mass and Stern-Volmer plots, and were attributed to the different surface areas and morphology of the two types of CNTs. This study offers a new biophysical perspective for elucidating the concept of NP-protein corona, a topic essential to our understanding of the implications and applications of nanomaterials in living systems.

CHAPTER 3

CONCEPT OF DICRETE MOLECULAR DYNAMICS SIMULATIONS IN STUDYING PROTEIN CORONA PHENOMENA

1. Intoduction

Nanomaterials have been increasingly applied in consumer products due to their unique physical and chemical properties as stated in Chapter 1. Recently, protein corona has been found to screen functionalized molecules conjugated to nanoparticles, and subsequently cause the loss of designed function[175]. In addition, interactions with nanoparticles can also alter the structure, dynamics, and function of the bound proteins, which could further impact recognition of the proteins by membrane receptors and the immune system. Previous experimental studies have provided much insight, such as the existence and size of the protein corona[135], and protein composition on the nanoparticle surface[136]. However, due to limitations in instrument resolution, the molecular detail of protein-nanoparticle interaction remains poorly understood. Computational modeling, in contrast, provides a useful approach to bridge the gap between experimental observations and the molecular systems of interest[176]. Here we performed both computational and experimental characterizations of protein corona formation between a silver nanoparticle (AgNP) and ubiquitin protein. Silver nanoparticles are widely used in commercial products for their antibacterial and antifungal properties[177], while ubiquitin is ubiquitously expressed in all eukaryotic cells regulating protein distribution and recycling, thereby making AgNP and ubiquitin a representative model system for studying nanoparticle-protein interaction and corona formation.

Two major challenges arise in computational modeling of protein corona. First is the large system size — where an abundance of proteins interacts with nanometer-sized nanoparticles, and second is the long timescales associated with protein corona formation. Traditional molecular dynamics approaches can accurately describe the molecular system of nanoparticles and proteins[137–140], but are not able to reach the relevant time and length scales needed for depicting large systems till equilibration[141,142]. In comparison, coarse-grained simulations[143] can be used to study large molecular systems and reach long time scales by using a simplified forcefield[144]. These coarse-grained simulations have been applied to study general aspects of NP-protein interactions[143,145–148], but have limited predictive power for studying NP interactions with specific proteins. To overcome this barrier, we adopted a multiscale modeling approach[178], which coherently blended atomistic and coarse-grained simulations[179,180]. All-atom simulations were first performed to investigate the possible binding modes between an individual ubiquitin and a AgNP, and the knowledge of AgNP-ubiquitin binding was then incorporated into the construction of a coarse-grained model. With the coarse-grained simulations, we were able to extensively characterise the structure and dynamics of AgNP interacting with multiple ubiquitin molecules (up to 50). The dynamics of both atomistic and coarse-grained models were sampled by discrete molecular dynamics (DMD)[181], an efficient sampling method for underpinning protein dynamics (Appendix A).

2. Results and Discussion

Our transmission electron microscopy (TEM) and UV-vis absorbance measurements (Experimental Section, Appendix A) confirmed the binding of ubiquitin and citrate-coated AgNP (Figs. 2.1 a,b). For UV-vis, specifically, a red-shift occurred from 393 nm (peak wavelength for AgNP absorbance) to 407 nm (peak wavelength for AgNP-ubiquitin absorbance), indicating an increased dielectric constant resulting from nanoparticle-protein complex formation. Consistently, our dynamic light scattering measurement (Fig. Appendix A1) showed a hydrodynamic size of 34.5 nm for AgNP-ubiquitin at molar ratios of 1:100 to 1:500 (zeta potential: 12.3 mV), compared to that of 4.8 nm for ubiquitins (zeta potential: 4.6 mV) and 13.6 nm for AgNPs (zeta potential: -45.0 mV) alone, further corroborating their effective binding.
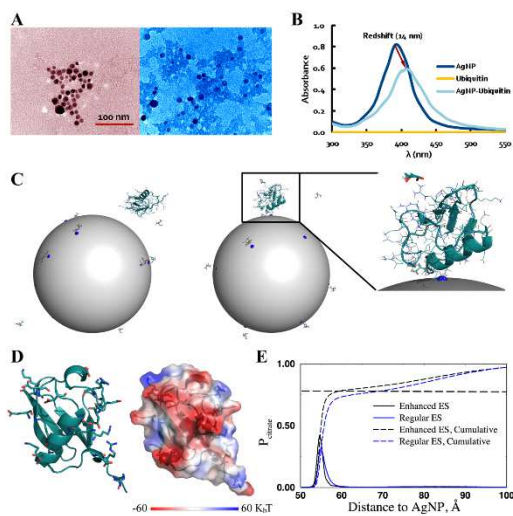
Figure 3.1. Interaction between a single ubiquitin and a citrate-coated AgNP. (a) TEM images of AgNPs (left panel) and AgNP-ubiquitin coronas (right panel) where the associations of the AgNPs and the proteins (shaded regions) are evident to imply their good binding affinity. (b)

UV-vis absorbance of AgNP, ubiquitin, and AgNP-ubiquitin, featuring a red-shift of the absorbance peaks for AgNP-ubiquitin and AgNP alone due to dampened surface plasmon resonance. (c) Initial (t = 0 ns) and final (t = 50 ns) structure of the ubiquitin-citrate-AgNP complex system. The ubiquitin is represented as cartoons, the side chains as lines, and the citrates as sticks. The gray sphere represents the nanoparticle, and the charged atoms on the AgNP surface are shown as blue spheres. Zoom-in view of the final structure indicates the binding between the ubiquitin and a charged AgNP surface atom. (d) The negatively (aspartate and glutamate) and positively (lysine and arginine) charged residues in ubiquitin are shown as sticks (left panel). The surface electrostatic potential (computed using PyMol, www.pymol.org) illustrates the cluster of negatively charged atoms near the protein helix (right panel). (e) Distributions of citrates around AgNP (solid lines) derived from the simulations. The electrostatic (ES) interaction between citrate and AgNP was artificially enhanced in one case. The dashed lines correspond to the accumulative probability. The horizontal dashed line corresponds to charge saturation, where the total charge of citrates equal that of the AgNP.

Next, we performed multiscale simulations to characterize the nanoparticle-ubiquitin corona formation *in silico*. We first performed atomistic simulations of a molecular system comprised of one ubiquitin molecule and one citrate-coated AgNP (Appendix A). The simulations were performed with implicit solvent, and the inter-atomic interactions were modeled by a physical force field adapted from Medusa[182], which include van der Waals, solvation[183], electrostatic, and hydrogen bond potentials. The coarse-grained silver atoms of the AgNP were assigned as hydrophobic with a small fraction being positively charged to account for the nanoparticle surface charges[184].

During simulations, we kept the center of the AgNP static, while allowing the ubiquitin and the citrates to move freely in the simulation box and surface silver atoms mobile on the NP surface. Since the physical properties of the coarse-grained AgNP model are rather general, the observed behaviors of AgNP-ubiquitin binding should be readily applicable to other metallic nanoparticles with positive surface charges, such as gold nanoparticles (AuNPs).

To evaluate whether ubiquitin could bind to a citrate-coated AgNP, we performed DMD simulations at 300 K with a ubiquitin molecule initially positioned away from a citrate-coated AgNP (Fig 4.1 c). Interestingly, we found that the neutral ubiquitin did not bind to the hydrophobic surface of the AgNP, but instead attracted to the surface charge of the AgNP by replacing the surface-bound citrates (-3e at neutral pH) that were stabilized by electrostatic interactions (Fig 4.1 c). Although ubiquitin does not have a net charge, it does possess eleven positively-charged and eleven negatively-charged residues out of the 76 total residues[185]. Near the surface of the ubiquitin helix, negatively-charged residues formed a cluster with low electrostatic potentials (Fig 4.1 d), which favored electrostatic interaction with counter charges[186]. The local surface area with low electrostatic potential allowed a stronger binding to the AgNP in simulations than did the negatively-charged citrates.

To test whether electrostatic interaction was the driving force for AgNP-ubiquitin binding, we artificially enhanced the binding affinity between citrates and AgNP by adding an additional charge to the citrate molecule (Appendix A). For both the case of artificially-enhanced electrostatic interactions and the regular (non-enhanced) case, we

performed ten independent atomistic DMD simulations with different initial AgNP/ubiquitin configurations. For a higher citrate-AgNP affinity due to enhanced electrostatic interactions, we did not observe any AgNP-ubiquitin binding in all simulations. In the case of regular citrate-AgNP interactions, we observed AgNP-ubiquitin binding for seven out of the ten simulations. The computed distributions of citrates from the AgNP also illustrated that the ability for ubiquitin to displace citrates and bind AgNP depended upon the electrostatic-dominating affinity between the citrates and the AgNP (Fig. 3.1 e). Therefore, the binding of ubiquitin to AgNP was mainly determined by electrostatic interactions.

From independent atomistic simulations, we constructed a structural ensemble of AgNP-ubiquitin binding complex. We averaged over the ensemble to compute for each residue the probability of forming contact with the AgNP, P_{AgNP}, (Appendix A). Only a subset of protein residues showed significantly high contact frequencies, while the rest of the protein did not interact with the AgNP (Fig. 3.2 a). As the result, the histogram of P_{AgNP} featured a bimodal distribution, with one peak close to zero and the other centered around $P_{AgNP} \sim 0.4$ (Fig. 3.2 b). We further determined the AgNP-binding residues (Fig. 3.2 b insert) as those with P_{AgNP} larger than 0.3, the median value separating two peaks in the histogram. These residues were located near the protein helix (Fig. 3.1 d). Although electrostatic interaction was indentified as the driving force for AgNP-ubiquitin binding, intriguingly only a fraction of the negatively-charged residues had high contact frequencies with the positively-charged AgNP surface (Figure 3.2 a). Since these negatively-charged residues are scattered on the surface of ubiquitin (Figure 3.1 c), it was

unknown *a priori* where these AgNP-binding residues were located. Next, we compared our results with a nuclear magnetic resonance (NMR) study of ubiquitin-gold nanoparticle (AuNP) binding[187]. In the NMR study, chemical shift of backbone NH groups was monitored upon ubiquitin binding to the AuNP. Since NMR chemical shift is very sensitive to the corresponding environment, chemical shift perturbations could be caused either by direct binding with the AuNP or due to NP-binding induced conformational changes. Three residues — 2, 15, and 18 — were found to have significant chemical shift perturbations upon binding to the AuNP. These residues are close to each other in the 3D structure, suggesting that the corresponding surface area bound to the AuNP. In our simulations, residue 18 had a high contact frequency with the AgNP and residue 2 also formed contact with AgNP (Fig. 3.2 a). The reason that we did not observe residue 15 in contact with the AgNP is due to the fact that leucine 15 is buried inside the protein. Since AgNP and AuNP are comparable both physically and chemically, we believe that the modes of their binding with ubiquitin are also comparable. This agreement between NMR observations and simulations highlights the predictive power of our computational methods.

We further investigated the thermodynamics of AgNP-ubiquitin binding by computing the potential of mean force, PMF (Appendix A). We calculated the 2D-PMF with respect to the centre-of-mass distance between AgNP and ubiquitin, d_{cm}, and the number of contacts between AgNP and the residues identified to bind AgNP specifically, N_c (Fig. 3.3 a). The 2D-PMF plot has two minima. One minimum corresponds to non-specific binding, where $N_c = 0$ and $d_{cm} \sim 70$ Å, while the other one represents the
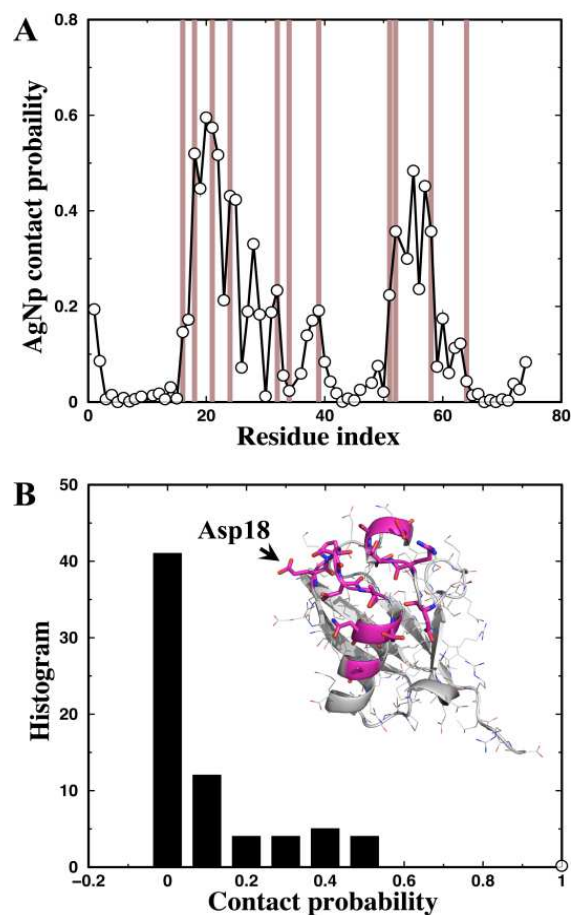
Figure 3.2. Specific binding between ubiquitin and AgNP. (a) The contact probability between AgNP and each ubiquitin residue, computed from independent all-atom DMD simulations (Appendix A). The shaded regions correspond to negatively charged residues, including both aspartate (Asp) and glutamate (Glu). (b) The histogram of the AgNP-ubiquitin contact probability displays a bimodal distribution. The ubiquitin residues with high contact frequency (> 0.3; corresponding to the second peak) to the AgNP are shown in sticks (insert). The residue Asp18 was also found to interact with gold nanoparticles[187].

the specific binding with $N_c > 0$ and $d_{cm} < 70$ Å. The barrier separating two minima corresponds to the re-orientation of the protein as illustrated in a typical simulation trajectory (Fig. 3.3 b). Before specific binding ($t < 0.7 \times 10^6$ t.u.), the system featured a large fluctuation of d_{cm} with the protein near the AgNP surface ($d_{cm} \sim 70$ Å). The protein had similar root-mean-square deviation (RMSD) from its native state before and after specific binding to AgNP. Therefore, protein re-orientation on the surface of AgNP was the rate-limiting step toward the specific binding.

In order to observe the formation of AgNP-ubiquitin corona *in silico*, it is necessary to include multiple proteins in simulations, which is beyond the capacity of atomistic simulations. Instead, we used a two-bead-per-residue model[188] to represent ubiquitin and a single atom to model each citrate. The inter- and intra-ubiquitin interactions were modeled by a structure-based potential model[189,190] which has been extensively used in computational studies of protein folding and protein aggregation[180]. The specific interactions between the AgNP surface charges and ubiquitin residues as well as other non-specific inter-molecule interactions were modeled according to atomistic DMD simulations (Appendix A).

We investigated AgNP-ubiquitin corona formation by performing DMD simulations of the coarse-grained system, with multiple ubiquitins (25 molecules) initially positioned randomly with respect to a citrate-coated AgNP. The temperature of the simulation system was kept at 325 K, which is below the melting temperature of ubiquitin, $T_m = 340$ K (Fig. Appendix A2).
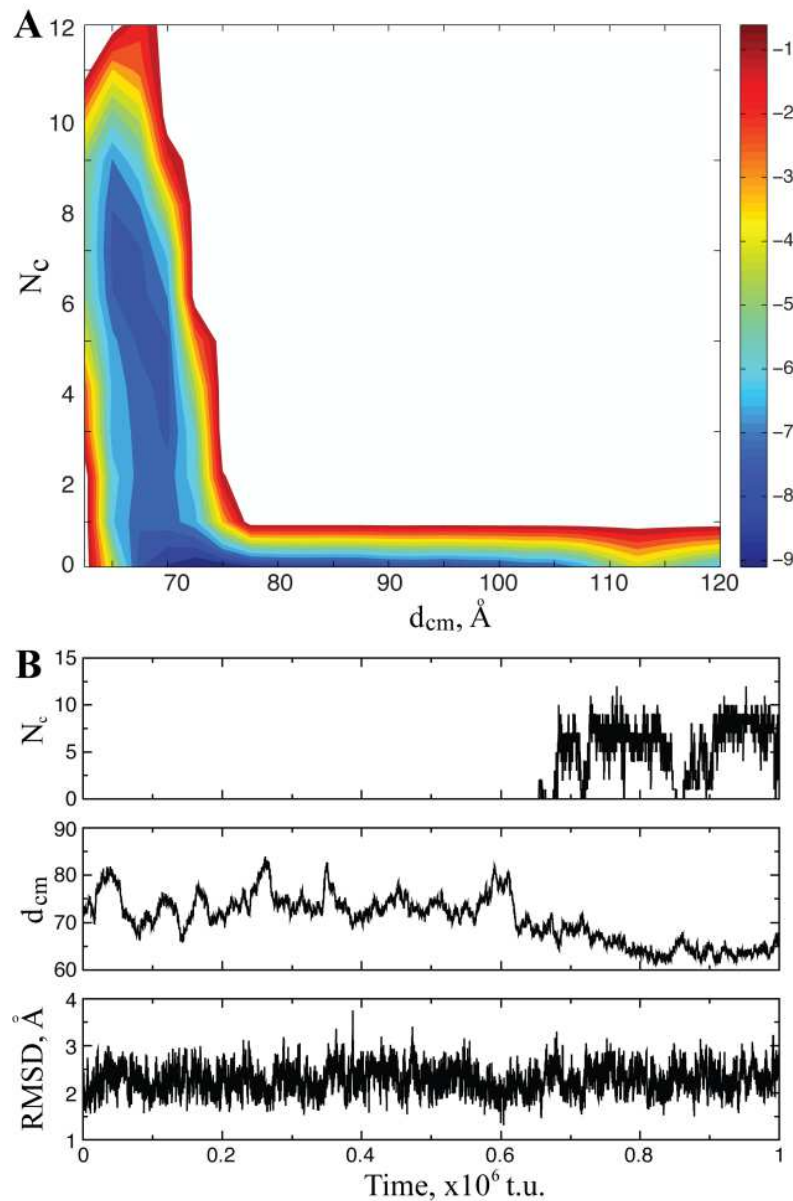
Figure 3.3. AgNP-ubiquitin binding thermodynamics. (A) Contour plot of the 2D-PMF with respect to inter-molecule distance, d_{cm}, and the number of specific inter-molecule contacts, N_c. The unit of PMF is kcal/mol. (B) A typical trajectory of the all-atom simulation of AgNP-ubiquitin binding. N_c, d_{cm}, and the RMSD of ubiquitin are shown as functions of the simulation time, in DMD time unit (t.u., Appendix A).

Therefore, an isolated protein was thermodynamically stable, mimicking the physiological conditions where the protein remains folded. To avoid potential biases associated with initial conditions, we performed ten independent simulations assuming different initial configurations and velocities. For each simulation we monitored the number of ubiquitins directly bound to the surface of AgNP, N_{bound}, as a function of time. All trajectories in Fig. 4a featured an initial fast binding, which slowed down as time progressed. Interestingly, the average N_{bound} did not follow a typical single-exponential binding kinetics, $\sim 1\text{-}exp(-\lambda t)$, which usually features a power-law with the exponent of 1 during initial binding in a log-log plot (Fig. 3.4 b). Instead, the exponent is $\sim 0.21 < 1$. Fitting analysis (Appendix A) suggested that a stretched-exponential, $\sim 1\text{-}exp(-ct^{\alpha})$, better represented the kinetics data. Similar stretched-exponential binding kinetics has been reported for the adsorption of human serum albumin onto a colloidal nanoparticle[191]. A stretched exponential function, corresponding to a linear superposition of exponential decays with a continuous distribution of relaxation times, is often used to describe the relaxation kinetics with high heterogeneity in the relaxation time. The heterogeneity could originate from competition with citrates, depletion of available binding sites for incoming ubiquitins, and non-specific interactions with other proteins. The binding rate between citrate and AgNP was concentration-dependent, and increased as ubiquitins displaced AgNP-bound citrates and subsequently increased the citrate concentration in solution. Examination of the simulation trajectories also suggested non-specific binding between the incoming protein and the proteins already bound to the surface, which

slowed down the specific binding with NP (Fig. A3). All these factors hindered the binding of ubiquitins to the AgNP surface, leading to the stretched exponential binding kinetics.

A stretched exponential decay of protein concentration in solution, $[p]\sim exp(-ct^\alpha)$ with $\alpha<1$, suggests that the association rate, $-(d[p]/dt)/[p] \sim 1/t^{1-\alpha}$ decreased as time increased and as more proteins bound to the NP surface. Assuming that the dissociation rates were the same for all proteins, the binding constant decreased as more proteins bound to the NP surface, which is indicative of the lack of binding cooperativity among the proteins. This observed anti-cooperativity is possibly a result of both steric hindrance[191] and non-specific protein-protein interactions (Fig. A3). Therefore, our coarse-grained simulations revealed a rich kinetics for nanoparticle-protein binding, which may need to be considered in future kinetic and mesoscopic modeling of corona formation, such as studies of the Vroman effect of abundant proteins for a nanoparticle entering the bloodstream[160].

The AgNP-ubiquitin complex structure derived from simulations had multiple ubiquitins bound to the surface of one AgNP, forming a single-layer protein corona (Fig. 3.4 c). The majority of AgNP-bound proteins stayed folded under the particular simulation condition (Appendix A) and bound to the surface of the AgNP with the protein helix facing the nanoparticle. Only in one of the simulations, one ubiquitin out of the 22 AgNP-bound proteins partially unfolded and the conformation was stabilized by extensive contacts with the hydrophobic surface of the AgNP (Fig. 3.4 c). In addition, we explored the effect of protein concentration on corona formation by performing DMD

simulation for a higher ubiquitin/AgNP stoichiometry of 50:1. In these simulations, ubiquitins competed with citrates for binding to the AgNP (Fig. 3.4 d). The final structure featured multiple layers of protein corona, whereas the first layer was dominated by specific binding between ubiquitins and the AgNP, and the outer layers were stabilized by protein-protein interactions (Fig. 3.4 e). This observation is consistent with our dynamic light scattering measurement (Fig. A1), where the hydrodynamic size of AgNP-ubiquitin was increased from ~35 nm at AgNP:ubiquitin ratios of 1:100 and 1:500 to 44 nm and 52 nm at AgNP:ubiquitin ratios of 1:1,000 and 1:2,000, respectively. Hence, the AgNP-ubiquitin complex structures derived from the coarse-grained simulations successfully revealed an atomic picture of the nanoparticle-protein corona.

The ability of nanoparticles to induce protein unfolding in the corona (Fig. 3.4 c) could be one of the mechanisms of nanotoxicity. To evaluate the impact of AgNP-binding on ubiquitin conformation, we computed for each protein residue the fraction of native contacts (Q-value[192]) for both the AgNP-bound and unbound ubiquitins (Fig. 3.5 a). A residue with its Q-value close to 1 maintains a native-like structure, while losing its structure if the Q-value is near 0. Both the AgNP-bound and unbound ubiquitins maintained native-like structures with most regions having their Q-values close to 1. Only loop regions between the secondary structures (18-19, 32-35, and 46-53) had relatively low Q-values. The difference in the Q-values for AgNP-bound and unbound ubiquitins suggests that residues in contact with the AgNP were stabilized upon binding (the regions with positive differences coincided with the residues bound to AgNP,
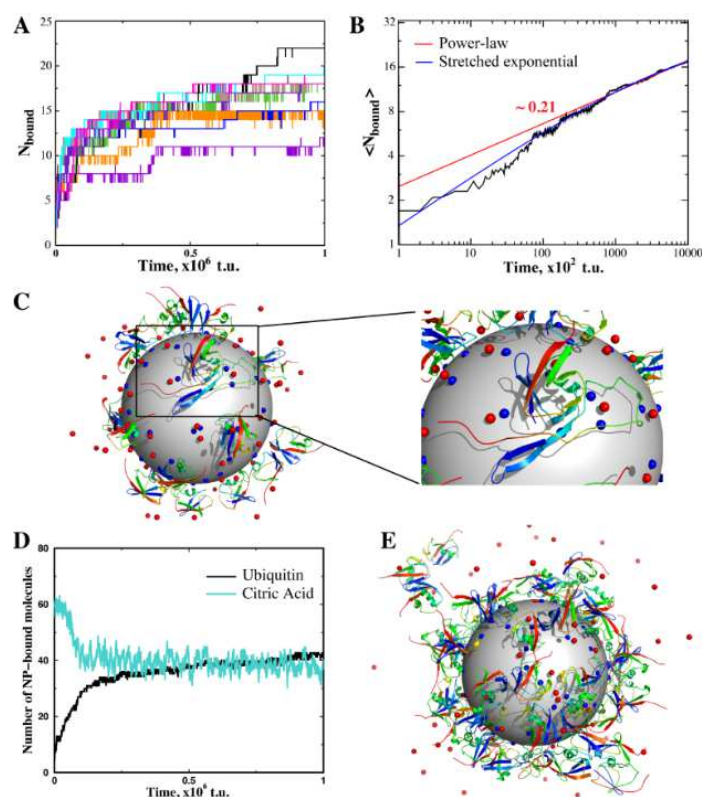
Figure 3.4. Ubiquitin-AgNP corona formation. (a) The number of ubiquitin molecules bound to AgNP, Nbound, was computed as the function of time (in DMD time unit, t.u., see Appendix A) from ten independent simulations (in different colors) of the coarse-grained molecular system. (b) The average number of ubiquitins bound to AgNP, <Nbound>, features a power-law (approximately linear) in a log-log plot. A power-law fit has an exponent of 0.21. A stretched exponential, ~1-exp(-ctα), better fits the data with α = 0.34. (c) The final structure from one of the simulations (corresponding to the black line with the highest Nbound in panel a). The ubiquitins are in cartoon representation. The citrates correspond to the red spheres. The large gray sphere denotes the AgNP, and the blue spheres on the surface of the AgNP are the positively charged atoms. One of AgNP-bound ubiquitin is unfolded on the nanoparticle surface (right). In a coarse-grained DMD simulation with a higher stoichiometry of ubiquitin to AgNP (50:1), ubiquitin (black line) competed with citrate (red) to bind AgNP by displacing initially-bound

citrates (d). At this high stoichiometry, multi layers of ubiquitins were found to deposit onto the surface of the AgNP (e)., Fig. 3.2 a). Two regions, one near the C-terminal of the helix and the other close to residue 46 in a loop, were significantly destabilized upon binding. The destabilization of protein helix due to AgNP-binding is consistent with our circular dichroism (CD) measurement (Appendix B), which revealed that the helical content was reduced by 27.8% relatively for the AgNP-bound ubiquitins compared to the free ubiquitins (Fig. 3.5 b). Our CD experiment also revealed small increase in the β-sheet content. Since the Q-value is computed based on protein native structure, it cannot measure the gain of secondary structures beyond the native state. With the protein concentration locally enriched on the AgNP surface, the increase of β-sheet content could result from the formation of inter-protein hydrogen bonds between partially unfolded protein regions. The formation of inter-protein hydrogen could further lead to protein aggregation[130], which requires further investigations in future studies.

3. Conclusion

In summary, both our computer simulations and experiments showed that ubiquitin proteins could readily bind to a citrate-coated AgNP to render a multilayer nanoparticle-protein corona. Despite many negatively-charged residues scattered on the ubiquitin surface, our multiscale modeling revealed a specific binding between ubiquitins and AgNP driven by electrostatic interactions. Notably, our coarse-grained simulations
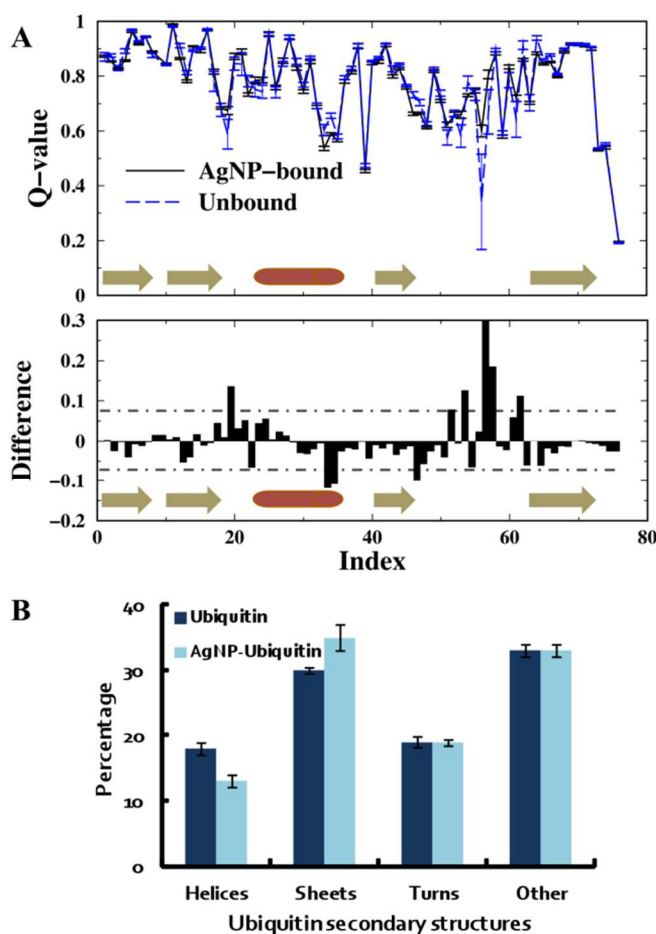
Figure 3.5. The structural change of ubiquitin upon AgNP binding. (a) The fraction of native contacts, Q-value, was computed for each residue for both the AgNP-bound (black) and unbound (blue) ubiquitins (top panel). The error bars were estimated from independent simulations. The yellow arrows indicate the residue segments forming β-strands, and the red rod denotes the residues forming the α-helix. The differences of Q-value were computed between AgNP-bound and unbound (bottom panel) cases. The two dashed lines correspond to deviations with one standard deviation above and below the average. The differences beyond the two lines are statistically significant. (b) The percentage of secondary structures in ubiquitin (dark blue) and in AgNP-ubiquitin (cyan) were probed by CD experiments (Apendix A).

of AgNP-ubiquitin corona formation uncovered an unusual stretched exponential binding kinetics, in agreement with a recent fluorescence kinetics measurement of nanoparticle-human serum albumin corona formation[191]. At a high stoichiometry, specifically, ubiquitins formed a multi-layer corona surrounding the AgNP. Both our simulations and experiments showed that AgNP-binding moderately destabilized the α-helix while increased the β-sheet content of the ubiquitins. Taken together, our new multiscale modeling method was able to recapitulate various structural and dynamic characteristics of nanoparticle-protein corona observed experimentally, and offered an atomic detail and a mechanistic insight into nanoparticle-protein self-assembly. Since the topic of protein corona and, especially, the connections between nanoparticle-protein corona with the transformation, biocompatibility, and immune responses of nanoparticles are still poorly understood, we believe that our method will find broad implications and applications in the research areas of molecular self-assembly, physical adsorption, nanobiophysics, nanomedicine, and the health and safety of nanotechnology.

4. Experimental and Computational Methods

We combined both experimental and computational approaches to characterize the formation of nanoparticle-ubiquitin corona formation. The details of both experimental and computational methods can be found in the Appendix A.

CHAPTER 4

EFFECTS OF NANOPARTICLE SURFACE CHEMISTRY ON NANOPARTICLE BINDING AND PROTEIN STRUCTURE

1. Introduction

Since their discovery, fullerene nanoparticles have attracted much attention due to their small sizes (~1 nm in diameter), caged structures, and distinct physicochemical properties. The ultrafine structures allow these nanoparticles to cross even the most difficult biological barriers, e.g. blood-brain barrier,[193,194] and reach different parts of the body, making them attractive drug and gene delivery vehicles.[195,196] Given their redox potentials as anti-oxidants[197,198] and relatively low toxicity,[199] fullerenes and their derivatives have also been investigated as novel drugs.[78,79,81,88,196] Specifically, functionalized fullerene derivatives have been found to inhibit the growth of sarcomas[200] and alleviate allergic responses.[201] Like many other types of nanoparticles, fullerene derivatives can bind to a wide range of proteins upon entering a biological system. For instance, it was found that fullerenes can bind to HIV protease,[78] influenza viruses,[81] serum albumin[202,203] and fullerene specific antibodies.[204] In light of the fact that increasing production and potential biomedical applications will eventually lead to human exposure to these carbon-based nanoparticles, it is essential to delineate the effect of fullerene-binding on the structure, dynamics and subsequent functioning of proteins, the building blocks of cellular life.

A major limitation for the use of pristine fullerene C_{60} has been its low solubility in water, and the need for special treatments like sonication, encapsulation in special carriers or use of co-solvents.[196] Alternatively, these hydrophobic nanoparticles can be functionalized with polar groups to better enable their designed biological and biomedical applications. One of the common functionalization strategies is hydroxylation, where polar hydroxyl (-OH) groups are chemically attached to the surface of fullerene nanoparticles to render soluble fullerenols.[196,205] Depending on the particular chemical procedures used to hydroxylate the fullerene, the number of OH groups on the hydroxylated fullerene (i.e., fullerenol $C_{60}(OH)_n$) may vary, assuming values of n=4, 6, 8, 20, 24, and 36,[206–209] for example. As one would expect, the solubility of fullerenol particles increases as the number of hydroxyl group is increased.[210] However, the effect of variations in nanoparticle surface chemistry on protein-fullerenol binding, including both structure and dynamics of protein-nanoparticle complex on the molecular and atomic levels, is largely unknown.

Various computational studies have been conducted in order to uncover the molecular mechanisms of the interactions between proteins and various fullerene derivatives. Using molecular dynamics (MD) simulations, hydroxylated fullerenols $C_{60}(OH)_{20}$ were bound to tubulin[211] and *taq* DNA polymerase[212] via the formation of hydrogen bonds. Fullerenes were also investigated *in silico* as a potential potassium channel blocker.[213] Through molecular modeling, fullerenes conjugated with small ligands were exploited as potential drugs to competitively bind the active sites of HIV-1 protease[78] and H5N3 influenza virus endonuclease.[81] Most of these previous studies,

however, focused on either pristine fullerenes or highly hydroxylated fullerenols. Recently, molecular docking has been applied to investigate the influences of size and extent of hydroxylation of fullerenols on their interactions with a variety of proteins, including RNA reverse transcriptase, RNase A, HIV-1 protease and tubulin.[214] It was found that the driving force of protein-fullerenol interaction was π-stacking and the increased number of hydroxyl groups resulted in a decreased binding affinity. However, since molecular docking studies assumed the protein conformation static or with only minor changes, variations in protein structure and dynamics upon nanoparticle binding as observed in many experiments[211,215,216] cannot be obtained.

Here, we applied a set of computational methods, including both docking and MD simulations, to systematically study the effect of fullerenol surface chemistry on its interaction with proteins, with the focus on changes in protein structure and dynamics. We used ubiquitin as the model protein since it is ubiquitously expressed in all eukaryotic cells[217] regulating protein distribution and recycling,[218] thus rendering our study both biologically and ecologically relevant. Specifically, we performed atomistic MD simulations with both explicit and implicit solvents. For the implicit solvent simulations, we used discrete molecular dynamics (DMD) simulations, a rapid conformational dynamics sampling algorithm[181] for biomolecules and molecular complexes. Compared to all-atom MD simulations with explicit solvent, DMD simulations with implicit solvents are able to reach longer time scales, which allowed direct observation of protein folding *ab initio*[219,220] and the observation of nanoparticle-protein corona formation.[117,221] For highly hydroxylated fullerenols, both our conventional MD and DMD simulations

suggested that the nanoparticles bound to the surface of ubiquitin via hydrogen bonds and the protein maintained its native structure. As a proof of the concept and in consideration of technical difficulty in accurately controlling the number of hydroxyl groups and solubilizing fullerenes, experiments were carried out only for highly hydroxylated fullerenol, $C_{60}(OH)_{20}$. We find that the binding sites derived from both docking and MD simulations are consistent with our fluorescence and isothermal titration calorimetry (ITC) measurements. As the number of hydroxyl groups decreased and the nanoparticles became subsequently more hydrophobic, both DMD and MD simulations revealed that the nanoparticles bound the protein via hydrophobic interaction and π-stacking. Only in DMD simulations, we were able to observe large-scale protein conformational dynamics that takes place on longer time scales, allowing the hydrophobic nanoparticle to partition into the protein core and subsequently disrupt the native protein structure. Overall, our results indicate that fullerenols with limited hydroxylation can induce protein misfolding, which could potentially trigger protein aggregation and adverse biological responses.[222,223]

2. Results and Discussions

Due to its high solubility and commercial availability, fullerenol with ~20 hydroxyl groups $C_{60}(OH)_{20}$ (buckyusa.com) is one of the most well-studied fullerene derivatives in both experiments[140,211,224,225] and simulations.[140,211,212,226–228] Therefore, we first focused on the binding of C_{60} and $C_{60}(OH)_{20}$ to ubiquitin using various computational methods, including molecular docking, MD (explicit solvent) and DMD

(implicit solvent) simulations. The simulation results of only $C_{60}(OH)_{20}$ were compared to experimental characterizations by fluorescence quenching, ITC, and circular dichroism (CD) spectroscopy. Experiments with pristine and low hydroxylated fullerenes were not carried out due to their poor solubility.

Fullerene C_{60} and fullerenol $C_{60}(OH)_{20}$ binding with ubiquitin. First, docking simulations were performed to identify the potential binding sites of C_{60} and $C_{60}(OH)_{20}$ nanoparticles on ubiquitin (Methods). The fullerenol nanoparticles showed two preferred binding sites on ubiquitin (see Fig 4.1 A). In 57% of docking simulations, $C_{60}(OH)_{20}$ bound to the protein surface region near residues 59–63, while in another 34% of simulations binding took place near the protein C-terminal (see Fig. Appendix B1 for a detailed view of the binding sites). The binding scores for these two sites are 8.2 and 8.1 kcal/mol, respectively. On the other hand, pristine fullerene showed only one predominant binding site that was similar to the first binding site of fullerenol, near residues 60–63 (Fig 4.1 B). The nanoparticle bound to this site in 90% simulations, with a binding score of 7.1 kcal/mol.
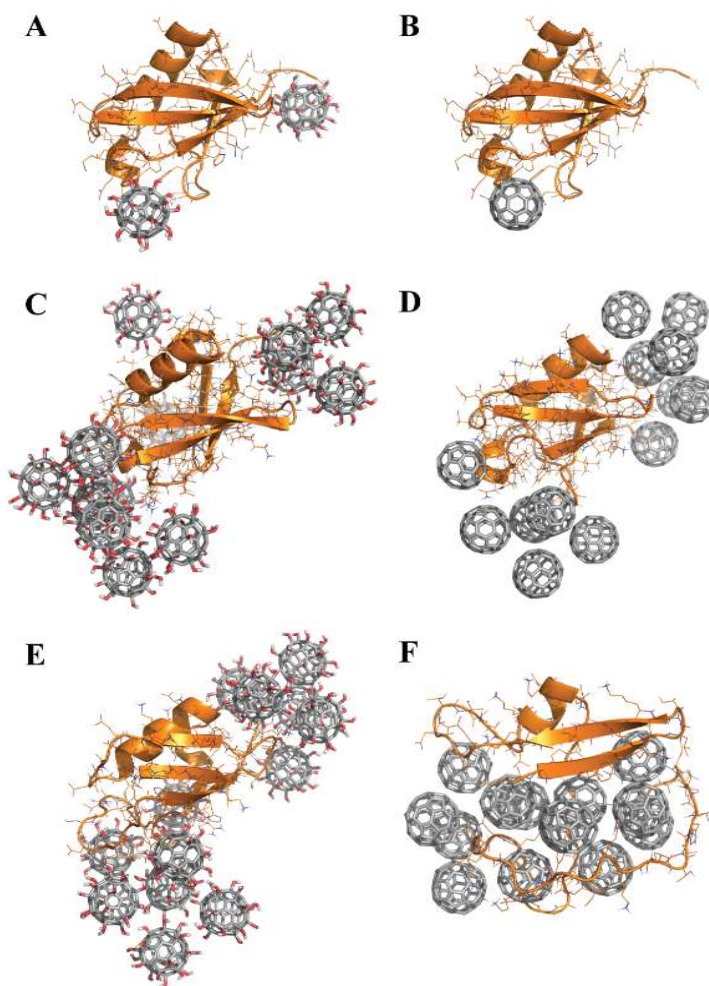
Figure 4.1. The predicted binding structures between ubiquitin and fullerene-based nanoparticles. The computational modeling approaches include molecular docking (A, B), MD simulations with explicit solvent (C, D), and DMD simulations with implicit solvent (E, F). The panels (A, C, E) correspond to the results for fullerenol $C_{60}(OH)_{20}$ binding, and panels (B, D, F) illustrate the binding with fullerene C_{60}. The protein backbone is shown in cartoon and the side-chains are in line representations. The carbon-based nanoparticles are shown in sticks.

Next, we performed both MD and DMD simulations of nanoparticle-ubiquitin binding (Methods). We started the simulations by placing 13 C_{60} or $C_{60}(OH)_{20}$ nanoparticles randomly around the protein. High nanoparticle-protein stoichiometry (13:1) was set up in order to observe multiple protein-nanoparticle binding events in one simulation. In both DMD and MD simulations, the hydrophilic $C_{60}(OH)_{20}$ nanoparticles bound to the protein surface at various locations via diffusion. Once bound, the particles started to diffuse on the protein surface and eventually formed clusters near the preferred binding sites. The final structures from MD (Fig 4.1 C) and DMD (Fig 4.1 E) simulations are highly similar, where the protein maintained its native-like structure while the nanoparticles form clusters near two similar binding sites. Interestingly, the two binding sites observed in MD and DMD simulations agree with these obtained from docking simulations. The binding in the proximity of TYR59 residue is also consistent with our fluorescence quenching experiment. Ubiquitin possesses only one tyrosine (TYR59), whose fluorescence intensity was measured for four different concentrations of $C_{60}(OH)_{20}$ at a given ubiquitin concentration. A linear static quenching of fluorescence intensity was observed with increasing $C_{60}(OH)_{20}$ concentration (Fig. Appendix B2). This observation indicates that $C_{60}(OH)_{20}$ molecules bound the protein specifically in the proximity of TYR59. The binding was further characterized by ITC measurement, which showed that an average of 1.3 fullerenol molecules bound to the protein (Fig. Appendix B3). This observation can be explained by the fullerenol preferential binding to two distinct sites of ubiquitin (near TYR59 and C-terminal). Different binding affinities of these two sites might result in the fullerenol:protein stoichiometry less than 2. Both the fluorescence

59

quenching and ITC experiments indicated that the binding affinity between $C_{60}(OH)_{20}$ and ubiquitin is 10–100 μM. The ITC derived stoichiometry is consistent with the simulation result of two binding sites per protein. Therefore, both our simulations and experiments are in agreement in terms of ubiquitin-$C_{60}(OH)_{20}$ binding, highlighting the predictive power of computational modeling for addressing nanoparticle-protein interactions.

In the fullerene-protein binding simulations, we found that the final protein structures from MD (Fig 4.1 E) and DMD (Fig 4.1 F) simulations were drastically different. In the DMD simulations, specifically, the hydrophobic fullerene nanoparticles eventually moved from the surface into the hydrophobic core of the protein. As a result, the protein was partially denatured with only a few native secondary structural elements remaining intact. Similar large protein conformational changes induced by binding of various types of hydrophobic carbon-based nanoparticles have been observed in both experiments[172] and simulations.[138] For example, serum proteins were found to undergo large conformational changes in the presence of multiwalled carbon nanotubes,[172] while MD simulations showed that a singlewalled carbon nanotube was able to partition into the core of a WW-domain protein to disrupt its native structure.[138] However, such large conformational changes were not observed in our accompanying MD simulations of fullerene-ubiquitin binding, where nanoparticles remained on the protein surface with similar binding sites as that for $C_{60}(OH)_{20}$ and the protein maintained its native-like structure. We hypothesize that the differential structures observed in the MD and DMD simulations of fullerene-ubiquitin binding are the result of the different time scales that

can be reached by implicit and explicit solvent within similar simulation times. Without friction due to solvent molecules, protein dynamics is known to be faster in implicit solvent simulations.[229] The key question here is given the same time scales in DMD simulations why C_{60} was able to denature the protein while $C_{60}(OH)_{20}$ was not. Next, we examined protein conformational dynamics in the presence of different nanoparticles using DMD simulations.

Differential protein conformational dynamics induced by C_{60} and $C_{60}(OH)_{20}$. To avoid the complexity of nanoparticle-nanoparticle and nanoparticle cluster-protein interactions, we performed DMD simulations of a single nanoparticle, C_{60} and $C_{60}(OH)_{20}$, interacting with a single protein ubiquitin. We monitored the root-mean-square deviations (RMSD) of protein conformation with respect to its native structure, the center-of-mass distance between the protein and the nanoparticle (d_{CM}), and the number of protein residues (N_C) in contact with the nanoparticle (typical simulation trajectories exemplified in Fig 4. 2). A residue was considered in contact with the nanoparticle if any of its heavy atoms were within 5 Å of the nanoparticle heavy atoms. Upon binding $C_{60}(OH)_{20}$, the RMSD value of the protein fluctuated around 2–3 Å with transient, large fluctuations occasionally approaching 4 Å (Fig 4.2 B) as observed in DMD simulations of ubiquitin alone without nanoparticle (Fig. Appendix B4). The contact number between protein and nanoparticle remained within 15 Å while the nanoparticle stayed on the protein surface with d_{CM} >15 Å (e.g., the snapshot structures along the trajectory in Fig 4.2 B).

In the case of C_{60}, the initial fluctuations of RMSD, contact numbers, and intermolecular distance d_{CM} upon nanoparticle binding were similar to those of $C_{60}(OH)_{20}$

binding (Figs. 3.2 A,B). After some large conformational fluctuations with RMSD around 2–3 Å ($3.5 \times 10^5 - 5 \times 10^5$ DMD time unit, t.u.), the contact number N_C increased to > 20 while the intermolecular distance d_{CM} reduced to ~5 Å. Eventually, the RMSD of the protein increased above 4 Å. The snapshot structure (inserts of Fig 4.2 A) indicated that the protein partially unfolded as the nanoparticle partitioned into the protein.

Taken together, since larger conformational changes often require higher energy changes and thus have lower probabilities for occurrence, the longer effective time scales in the DMD simulations allowed the observation of ubiquitin conformational dynamics with larger RMSD values (Fig 4.2 and Fig. Appendix B4) compared to the MD simulations with explicit solvent (Fig. Appendix B5). The observed C_{60}-ubiquitin structures in MD simulations (Fig 4.1 D) were consistent with the initial phases of C_{60} binding with ubiquitin, where nanoparticles remained on the protein surface without denaturing the protein (Fig 4.2). With large conformational changes populated along the DMD simulation trajectory, the protein partially exposed its hydrophobic core and the hydrophobic C_{60} was able to plug into the protein core to cause denaturation. On the other hand, the hydrophilic $C_{60}(OH)_{20}$ stayed on the protein surface as the protein folded back into its native state, results in transient large conformational fluctuations as observed also in DMD simulations of ubiquitin without any nanoparticles (Fig. Appendix B4). Therefore, the major reason for the differential protein dynamics upon binding to the nanoparticles is the difference in the nanoparticle surface chemistry — the number of hydroxyl groups. Next, we performed DMD simulations of protein binding with nanoparticles of different extent of hydroxylation.
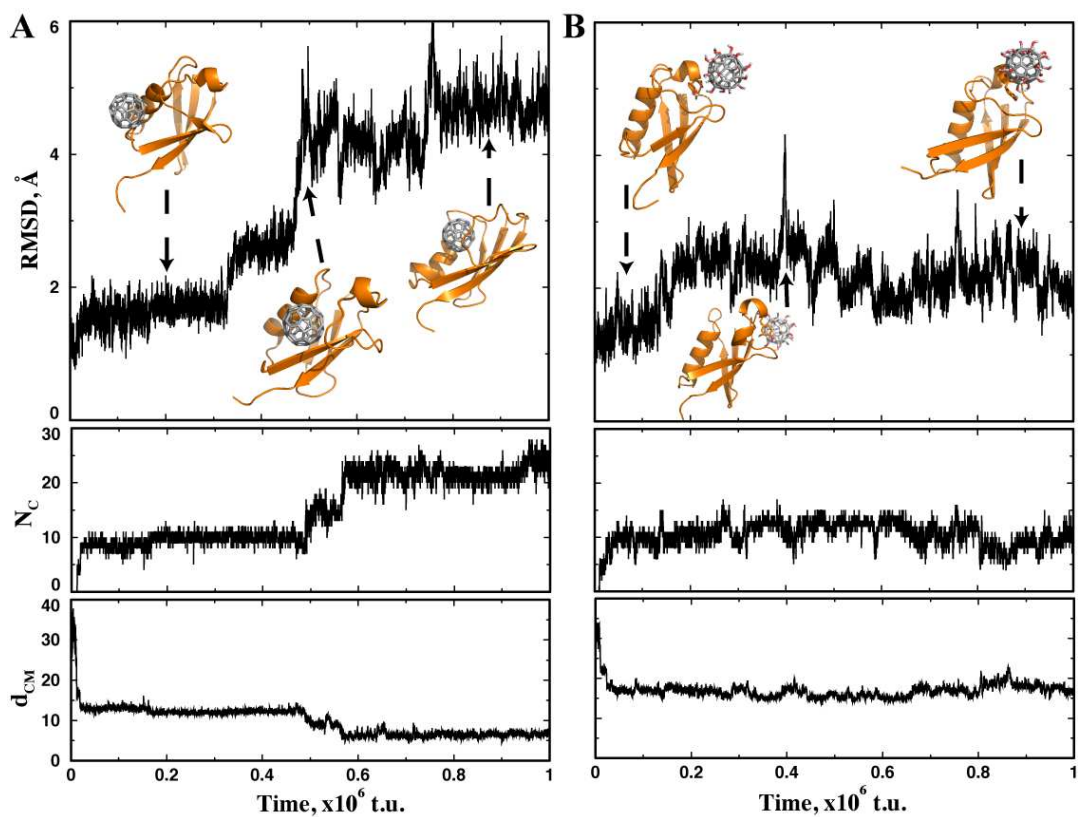
Figure 4.2. The binding trajectories in DMD simulations. Differential conformational dynamics of ubiquitin were observed upon binding fullerene C_{60} (A) and fullerenol $C_{60}(OH)_{20}$ (B). The RMSD of ubiquitin, the number of residues in contact with the nanoparticle (N_C), and the inter-molecular distance between the corresponding centers of mass (d_{CM}) were monitored as the function of simulation time, in the unit of DMD time unit (t.u.; see Methods). The snapshot structures of the protein-nanoparticle complex were shown as inserts along the trajectories.
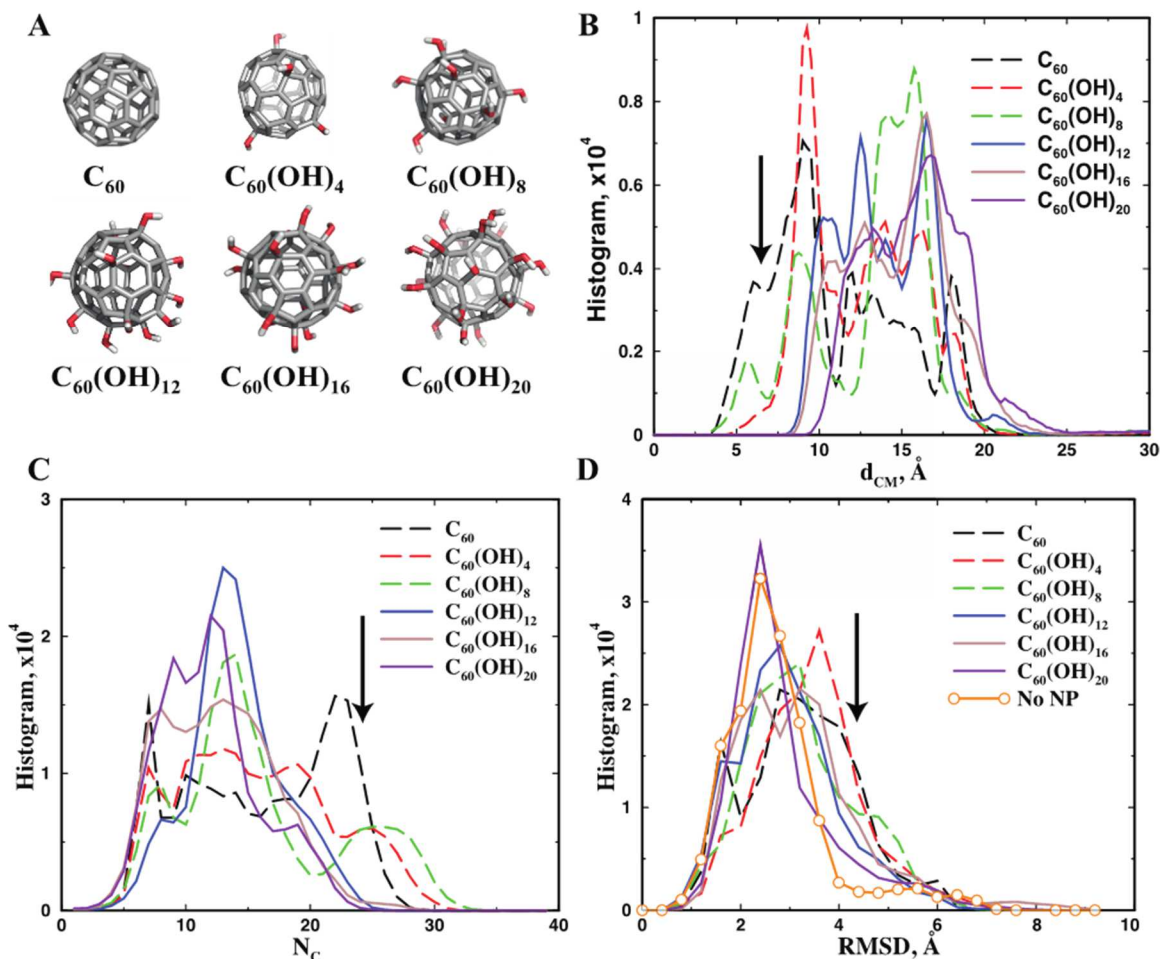
Figure 4.3. The equilibrium binding between ubiquitin and fullerenols with various numbers of hydroxyls. (A) The fullerenols C60(OH)n used in simulations, where n=0, 4, 8, 12, 16, and 20, are shown in sticks. Based on multiple independent DMD simulations with different initial conditions, we computed the histogram of (B) inter-molecular distances, dCM, (C) number of contacting residues, NC, an (D) the RMSD of the protein. The arrows highlight the significant changes in the histogram plots that correlate with the changes in the number of hydroxyl groups

Ubiquitin-fullerenol binding with different extent of hydroxylation. We investigated the interactions between ubiquitin and nanoparticles with intermediate hydroxylation,

including 4, 8, 12 and 16 hydroxyl groups and thus having intermediate surface hydrophobicity as well as various degrees of hydrogen bond donors and acceptors (Fig 4.3 A). For each fullerenol derivative, we performed DMD simulations with a single nanoparticle and a single protein. To avoid potential bias of initial condition and to increase sampling statistics, we performed 20 independent simulations with different initial intermolecular positions and orientations (Methods). Based on the independent DMD simulations, we calculated distributions of the intermolecular distance d_{CM} (Fig 4.3 B), the number of residue contacts N_C (Fig 4.3 C), and the protein RMSD (Fig 4.3 D). We found that as the number of surface hydroxyl groups decreased the fullerenol exhibited an increased probability to penetrate into the protein core (with low $d_{CM} < 10$ Å and large number of residue contacts $N_C > 20$) and consequently denatured the protein (with RMSD > 4 Å). Interestingly, we found that these nanoparticles can be approximately divided into two categories based on their binding behaviors, i.e., the more hydrophobic C_{60}, $C_{60}(OH)_4$, and $C_{60}(OH)_8$, and the more hydrophilic $C_{60}(OH)_{12}$, $C_{60}(OH)_{16}$, and $C_{60}(OH)_{20}$. The more hydrophobic fullerenols ($C_{60}(OH)_4$ and $C_{60}(OH)_8$) behaved like the pristine fullerene C_{60}, while $C_{60}(OH)_{12}$ and $C_{60}(OH)_{16}$ were similar to $C_{60}(OH)_{20}$ (Figs. 3.3 B-D). Due to smaller number of surface hydroxyls, the hydrophobic fullerenols have large hydrophobic patches on the surface, which can be buried inside the protein and thus disrupt the protein native structure. As the number of hydroxyl groups increases, the available hydrophobic patches and their sizes decrease, which allow the nanoparticles to stay on the protein surface upon protein binding.

In order to quantify the detailed binding between fullerenol and protein residues, we computed the average contact frequency between each residue and the corresponding nanoparticle (Fig 4.4). We colored the residues in the protein structure according to their binding frequencies (Fig 4.4 B). Compared to the more hydrophilic fullerenols, i.e., $C_{60}(OH)_n$ with $n \geq 12$, the binding of the more hydrophobic ($n < 12$) nanoparticles with the protein appeared mostly non-specific, including significant probabilities to interact with the buried residues. As the number of hydroxyl groups increased, the binding of hydrophilic fullerenols with the protein became more specific. For instance, the binding sites of fullerenol $C_{60}(OH)_{20}$ include the region near TYR59 and C-terminal (Fig 4.4 B). The C-terminal binding has a weaker probability (yellow color) compared to the binding near TYR59 (red color), consistent with the estimated binding probabilities from docking simulations.

Even though solubility increases as more hydroxyl groups are added to the nanoparticle surface,[210] our simulation study suggests that, compared to pristine fullerene C_{60}, fullerenol $C_{60}(OH)_8$ was still able to denature the bound proteins. Possibly due to the small size of the fullerenol nanoparticle, the extent of protein conformational change upon binding a single nanoparticle was relatively small as the increase of RMSD was relatively small (Figs. 3.2, 3.3). Next, we examined the effect of multiple fullerenol binding on ubiquitin secondary or tertiary structures.
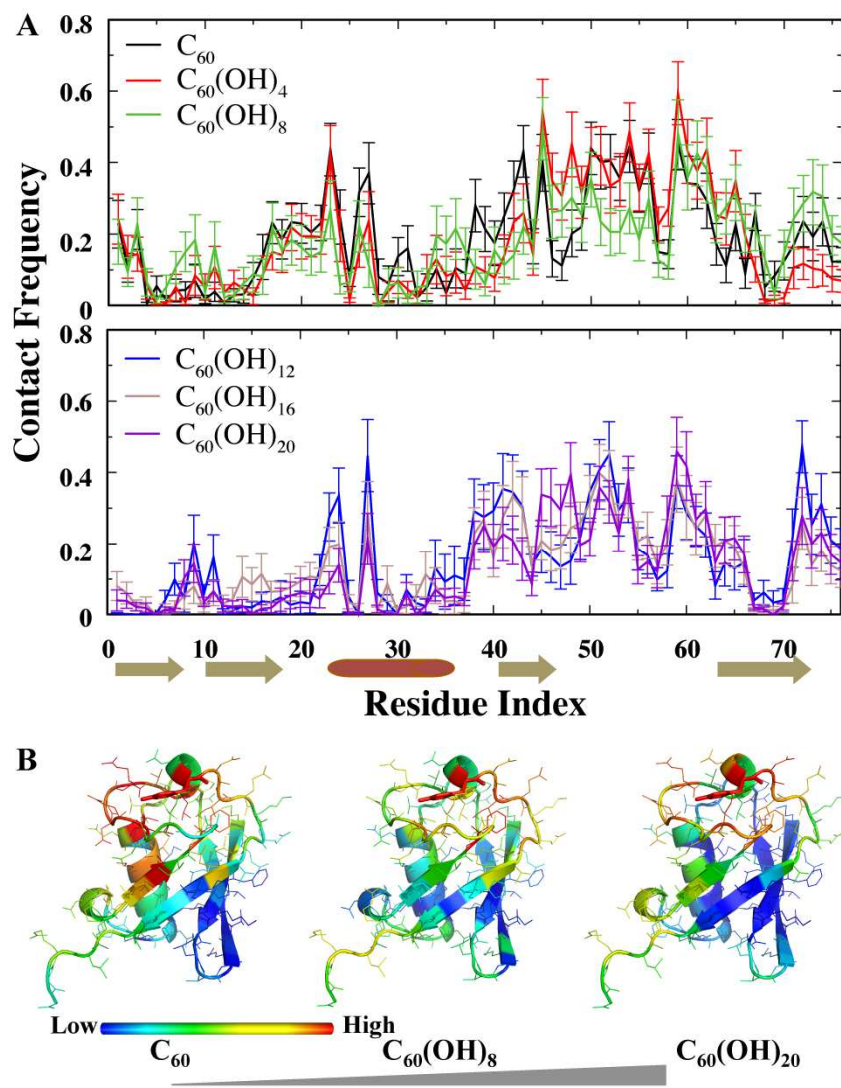
Figure 4.4. The contact frequency between fullerene and each protein residue. (A) The average contact frequency is computed over the independent DMD simulations, and the error bars correspond to the estimated standard errors. The schematics of protein secondary structures were shown underneath the sequence index, where arrows correspond to strands and cylinders denote helices. (B) In the native structure, we colored each residue according to their contact frequencies with respect to the nanoparticle.

67

Protein structural changes upon fullerenol binding. We performed DMD simulations with a ubiquitin protein interacting with multiple fullerenols of $C_{60}(OH)_n$, where n=0, 8, 20. Multiple independent simulations with different initial conditions were performed to enhance the sampling statistics. Averaged over the independent simulations, we computed the protein RMSD as the function of simulation time (Fig 4.5 A). Fullerene C_{60} had the greatest effect in terms of protein denaturation, with the highest RMSD of ~ 8 Å at the end of the DMD simulations. The protein core was loaded with multiple nanoparticles (Figs. 3.1, 3.5). As expected, fullerenol $C_{60}(OH)_8$ was also able to denature the protein, with RMSD > 4.5 Å; however, these nanoparticles could not fully penetrate the protein and were partially buried into the protein (Fig 4.5 A) to compromise the structure of the protein. Interestingly, the $C_{60}(OH)_{20}$-bound ubiquitin exhibited a smaller RMSD compared to the reference simulations where the nanoparticle was absent. The decreased RMSD in the presence of $C_{60}(OH)_{20}$ is likely due to the fact that a high number of surface hydroxyl groups on the nanoparticle surface was able to establish multiple hydrogen bonds with the protein side chains, thereby reducing their thermal fluctuations. To estimate the changes in protein secondary structures upon nanoparticle binding, we also calculated the average secondary structure contents of the ubiquitin using a method proposed by Srinivasan and Rose[230] (Fig 4.5 B).   The average was taken over multiple independent simulations. Compared to the reference simulations of ubiquitin alone, binding of fullerene and various fullerenols consistently reduced the content of α-helixes and turns, and increased the amount of random coils.
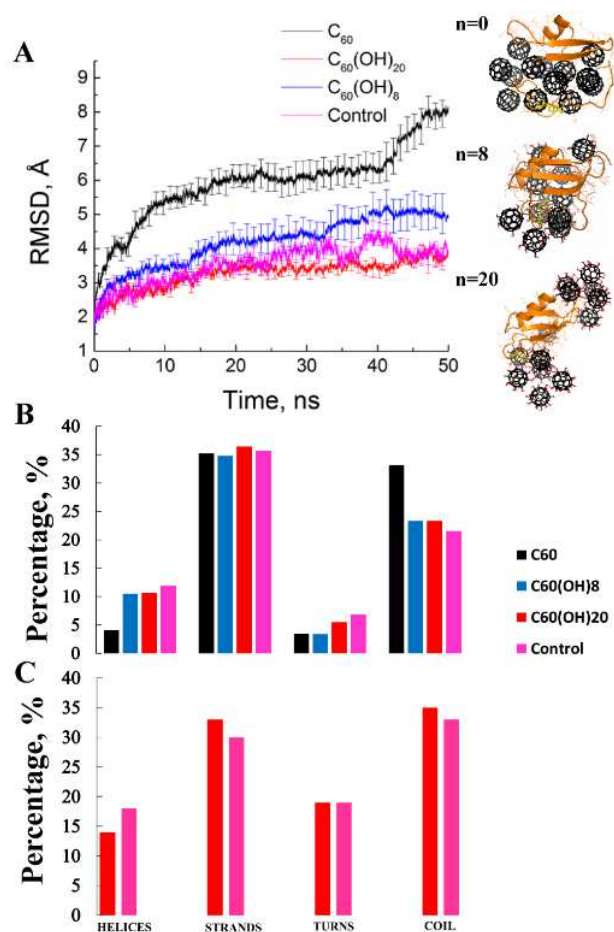
Figure 4.5. The tertiary and secondary structures of ubiquitin induced by multiple nanoparticle binding. (A) We monitored the average RMSD of ubiquitin as the function of DMD simulation time. Typical complex structures obtained from simulations were shown as inserts. The simulations with protein only were used as the control for comparison. (B) The secondary structure contents were computed from DMD simulations of ubiquitin upon binding fullerenols with various numbers of hydroxyls. (C) The experimentally measured protein secondary structure elements.

The changes in β strands are relatively small without obvious trends. Among the modeled nanoparticles, fullerene C_{60} had the strongest effects in terms of affecting protein

69

secondary structures. Experimentally, due to solubility and availability issues, we only performed CD measurements of ubiquitin alone and ubiquitin incubated with $C_{60}(OH)_{20}$ (Methods; Fig. Appendix B6 and Fig 4.5 C). The experimentally measured changes in secondary structure contents were qualitatively consistent with the predicted changes derived from DMD simulations. Although there are differences in the absolute values of secondary structure contents between experiments and simulations, the changes upon fullerenol bonding are in accord with each other, including slight decreases in alpha helices, and increases in β sheets and random coil content (Figs. 3.5 B, C).

3. Conclusion

We studied the binding of ubiquitin with fullerene and its fullerenol derivatives, $C_{60}(OH)_n$ with various number of hydroxyls, n. We find that while hydrophilic fullerenol binding primarily on the protein surface, the hydrophobic fullerenes enter into the core of the protein and denature it. In the case of $C_{60}(OH)_{20}$ for which experiments were possible,, agreement between experimental measures (including ITC, fluorescence quenching, and CD) and various computational methods (docking, MD with explicit solvent, and DMD with implicit solvent) underscore the predictive power of computational modeling for nanoparticle-protein interaction. Most importantly, the ability of DMD simulations to sample longer time scales than traditional MD simulations with explicit solvent allowed the observation of protein denaturation with hydrophobic fullerene C_{60}. The denaturation of proteins by hydrophobic carbon-based nanoparticles has already been observed experimentally.[172,231–233] Considering the technical difficulty in

controlling the number of hydroxyls and low solubility of fullerene nanoparticles, we are unable to experimentally verify the misfolding induced by fullerene nanoparticles. Our study has shown that DMD simulations can be used as an efficient tool for unraveling the complex phenomena at the nano-bio interface, such as delineating the structure and dynamics of nanoparticle-protein corona[158] in order to better understand nanotoxicity and thereby enable improved applications of nanomedicine.

The surface chemistry of nanoparticles is an important determinant of their interactions with proteins in addition to the nanoparticle size and shape.[158] In this work, we studied the effect of different extent of hydroxylation, where the surface hydroxyl groups can serve as both donor and acceptor for hydrogen bonding. Our results suggested that different extent of hydroxylation had significant effects on $C_{60}(OH)_n$-protein interactions. Specifically, fullerenols with $n \leq 8$ were able to denature the protein since their relatively small number of hydroxyls allowed more hydrophobic patches on the nanoparticle surface (Fig 4.3 A) and significant interactions with the protein hydrophobic core to disturb its tertiary structure. Hydrophilic nanoparticles, in contrast, remained bound on the protein surface without inducing major structural changes. In fact, hydrophilic particles, especially $C_{60}(OH)_{20}$, could form multiple hydrogen bonds with protein surface residues to reduce structural fluctuations (Fig 4.5 A). Taken together, our study revealed a distinctive role of surface hydroxylation in term of nanoparicle-binding induced protein misfolding. With the advancement of computational modeling of the nano-bio interface and improvement of the predictive power, it might be possible to accurately adjust the nanoparticle surface chemistry in order to reduce the potential

adverse effects such as nanoparticle-binding induced protein misfolding and concomitantly increase the nanoparticle biocompatibility.

4. Methods

Docking. C_{60} and $C_{60}(OH)_{20}$ were docked on to human erythrocyte ubiquitin structure obtained from the protein data bank (PDB ID: 1UBQ[234]). Three of 76 residues of this structure are different from the *A. thaliana* ubiquitin, which was used in experiments. Docking simulations were performed using AutoDock 4.2 docking software[235] with its default force field. Fifty docking simulations, each with 10 trials, were carried out keeping both protein and nanoparticles rigid. A Lamarckian genetic algorithm[235] with 2.5×10^7 evaluations was used. The resulting docked poses were clustered based on their mutual root-mean-square deviation values, using a cutoff of 0.8 nm. Here, the larger than usual cutoff value of 0.2 nm was used because the nanoparticle was able to bind the same site by rotating around its center of mass.

Molecular Dynamics (MD). The MD simulations were carried out using GROMACS simulation package version 4.5.4[236] with OPLSAA force field[237,238] for protein and a compatible parameter set for nanoparticles as described elsewhere[212]. The protein-nanoparticle complex was placed in a simulation box whose edges were at least 0.9 nm away from the solute. The box was then filled with TIP4P[239] water molecules. NA^+ and CL^- ions were added so that the simulation box had an ion concentration of 100 mM. The system was energy minimized between each of these steps using steepest descent algorithm. First, the simulation system was equilibrated with a 50 ps long NVT

simulation, which was followed by a 100 ps long NPT simulation. During these equilibrium runs, the temperature and pressure of the system were coupled using the Bussi-Donadio-Parrinello velocity rescale algorithm[240] (298 K, τ_T = 1 ps) and Berendsen weak coupling algorithm[241] (1 bar, τ_P = 4 ps, only for NPT simulation), respectively. For production runs, the Bussi-Donadio-Parrinello velocity rescaling algorithm and Parinello-Rahman algorithm[242] were used for temperature (298 K, τ_T = 1 ps) and pressure coupling (1 bar, τ_P = 4 ps), respectively. Six independent copies of each simulation were carried out, each lasting 100 ns. The simulation time step was set at 2 fs with all bonds constrained using the LINCS algorithm.[243] The electrostatic interactions were treated with smooth PME method,[244,245] with a cut-off of 0.9 nm. For Lennard-Jones interactions a cut-off of 1.4 nm was used without any switch or shift functions.

Discrete Molecular Dynamics (DMD) Simulations.

In our DMD simulations, fullerene derivatives with 0, 4, 8, 12, 16 hydroxyl groups were prepared by randomly removing –OH groups from fullerenol, whose structure was taken from a previous $C_{60}(OH)_{20}$ model.[85,86] The system was modeled and visualized using PyMOL.[246] Single nanoparticle simulations were carried out at room temperature 300 K. Dimensions of the simulation box were set at 75 Å in all three dimensions and periodic boundary conditions were imposed. Prior to simulation, ubiquitin and the nanoparticle were positioned away from each other. Initially, system was equilibrated for 5 ns and followed by 50 ns production simulations. Twenty independent simulations with difference initial conditions, including relative inter-molecular distance and orientation as well as velocities, were performed in order to

reduce the sampling bias of initial conditions and to increase sampling statistics. During the simulation we monitored protein RMSD. For comparison, multiple independent simulations of ubiquitin alone without nanoparticles were performed without any nanoparticle.

For the study of ubiquitin binding with multiple nanoparticles, 13 nanoparticles and one protein were initially positioned away from each other in a cubic simulation box of 100 Å. We chose to simulate three representative cases: insoluble fullerene C_{60}, partially hydrophobic $C_{60}(OH)_8$ and hydrophilic fullerenol $C_{60}(OH)_{20}$. For each case, 10 independent DMD simulations were performed and each simulation followed the same protocol as the single nanoparticle binding simulations.

Fullerenol Preparation. A stock of fullerenols (BuckyUSA) 1 mg/ml dispersed in Milli-Q was firstly sonicated and then the new 10x diluted filtered stock was made for the measurements. Filtration was done with Anotop filters (0.1 μm, Whatman).

Fluorescence measurements. Further study of the ubiquitin fullerenol interaction was done by fluorescence quenching study of ubiquitin (A. thaliana) tyrosine (Y) residue (MQIFVKTLTGKTITLEVESSDTIDNVKAKIQDKEGIPPDQQRLIFAGKQLEDGRTL ADY N IQKESTLHLV LRLRGG) by adding fullerenols into solution. The experiment was performed on a Varian Eclipse fluorometer. Concentrations of added fullerenol in solution were 9.43 mM, 15.7 mM, 23.6 mM, and 47.2 mM, while the ubiquitin concentration was held constant at 10 mM. The mixtures were incubated for 2 h before the measurement. The excitation wavelength was 220 nm and the observed emission was 303 nm, which is the emission wavelength characteristic for tyrosine residue. We fitted

data with the Stern-Volmer equation:[247]

$$\frac{I_0}{I} = 1 + K_b \cdot C_{FUOH}$$
(4.1)

where I_o is emission intensity of the ubiquitin without added fullerenol, and I is the emission intensity of ubiquitin when fullerenol with a concentration of C_{FUOH} is added to the protein.

To account for apparent quenching, we corrected our intensities considering our cell geometric and absorption characteristics. The correction is described by Parker equation:[248]

$$\frac{I_{corrected}}{I_{observed}} = \frac{2.3 \cdot d \cdot A_{ex}}{1 - 10^{d \cdot A_{ex}}} \cdot \frac{2.3 \cdot s \cdot A_{em}}{1 - 10^{s \cdot A_{em}}} \cdot 10^{g \cdot A_{em}}$$
(4.2)

Where $I_{corrected}$ and $I_{observed}$ are the corrected and observed intensities, A_{ex} and A_{em} are absorbance per centimeter at the excitation and emission wavelengths, and parameters s, g and d depend on the geometry of the measurement.

Isothermal titration calorimetry (ITC). The thermal dynamics of the binding between fullerenol and ubiquitin was investigated using an isothermal titration calorimeter (ITC, TAM III, TA Instruments). 1.88 mM of fullerenol solution (in Milli-Q water) was placed in the glass syringe, and then was titrated into the ampoule containing 0.1 mM ubiquitin solution (in Milli-Q water) at the rate of 9.975 μL per injection. The time interval between two consecutive injections was set to 15 min, and total 25 injections were performed. The raw data was pre-processed using TAM Assistant, and imported into NanoAnalyze, then fitted using the built-in Independent Model to render

the thermal dynamics of the binding, which yields n=3.083, K_a=6.324x10^4 M^{-1}, ΔH=16.83 kJ/mol, K_d=1.581x10^{-5} M, and ΔS=148.3 J/mol.K.

CHAPTER 5

DIFFERENTIAL BINDING OF MULTIPLE AMPHIPHILES TO NANOSHEETS

1. Introduction

Due to their unique physical properties[37,249,250], graphene and graphene derivatives have emerged as ideal materials for constructing novel nano- and quantum devices. The potential applications of graphene derivatives range from electronic circuits and energy storage to biomedical nanodevices for imaging, sensing, and diagnosis[45,251–254]. The increasing application and foreseeable mass-production of graphene derivatives[255,256], however, will likely lead to their environmental discharge, while advances in graphene-based nanomedicine will induce biological exposure to such engineered nanostructures. Consequently, it has become increasingly crucial to delineate the transformation, evolution, transport, and biocompatibility of graphene derivatives in the aqueous phase, ranging from biological to environmental systems[257].

Once discharged into the environment or introduced to biological systems, graphene derivatives may interact with natural organic matter, biomolecules, and other ionic and molecular complexes through self assembly and chemical reactions. Most of these natural and bio-materials are amphiphilic in nature, and are usually comprised of carbohydrates, peptides, and fatty acids. Since natural amphiphiles may bind with graphene derivatives to render a biocorona[161,258], it is conceivable that the fate of graphene derivatives in biological systems and the environment is determined by the entity of the biocorona rather than the nanomaterial substrates alone. Possessing vastly

different molecular morphology and physicochemical properties, natural amphiphiles are expected to feature distinct binding affinities for graphene derivatives to ascribe the latter new physical chemical and/or biological identities. Furthermore, differences in the concentration and affinity of natural amphiphiles may lead to their competitive binding for graphene derivatives, similar to the Vroman effect that is exhibited by serum proteins adsorbed onto solid surfaces[259].

The binding of small ligands and peptides to graphene derivatives has been a subject of a few recent studies. For example, Dai *et al.* showed that simple physisorption through π-stacking could be exploited to load doxorubicin -- a commonly used cancer drug -- onto graphene oxide[260]. It was demonstrated that uniformly dispersed graphene oxide[261,262] in a chitosan-ferrocene matrix became positively charged, thereby boosting its capacity to stabilize biomolecules such as glucose oxidase and consequently facilitate the fabrication of a glucose biosensor[253]. Katoch *et al.* showed that a dodecamer peptide could bind to graphene by orienting its aromatic residues, such as tryptophan and histidine, parallel to the nanosheet; by comparing the binding affinities of mutant peptides with tryptophans substituted by alanines the researchers identified an essential role of tryptophan in attributing to the strong binding of the peptide and the graphene[48]. The stability of peptides adsorbed onto a graphene nanosheet was studied through coarse-grained simulations, which underpinned the importance of π-stacking, van der Waals, and hydrophobic interactions in the binding[49,50]. Density functional theory calculations were employed to study how biomolecular adsorption could affect the density of states of graphene nanosheets[263]. These studies, however, mostly focused on the binding of

graphene derivatives with single-molecular or single-component amphiphiles. A systematic study of the binding of graphene derivatives with a collection of representative natural amphiphiles is essential for elucidating the transformation and dynamics of graphene derivatives in complex biological and environmental media.
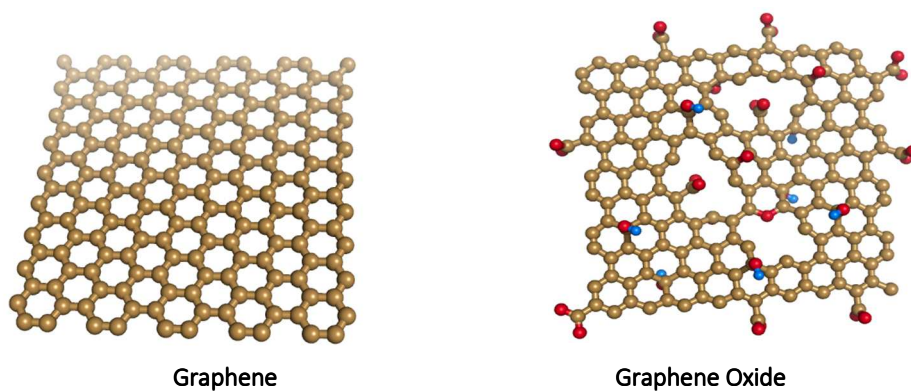
Herein we combined computational modeling and experimental characterizations to examine the binding of graphene and graphene oxide with natural amphiphiles. Specifically for simulations, we adopted cellulose dimers, tri-alanine peptides, and palmitic acids as model amphiphiles (Fig. 5.1) to represent the sugar, peptide, and fatty acid moieties present in algal exudates used in our experiments, respectively. In addition to being prevalent in aquatic environments, these molecular species are also ubiquitous across the biosphere of living organisms. We performed discrete molecular dynamics (DMD) simulations, a rapid dynamic sampling algorithm[264] to characterize the binding between the graphene derivatives and the natural amphiphiles. The molecular systems were modeled using the united atom representation, in which polar hydrogen and heavy atoms were explicitly modeled. The simulations were performed with implicit solvent, and the inter-atomic interactions were modeled by a physical force field adapted from Medusa[182], which include van der Waals, solvation[183], electrostatic, and hydrogen bond[180,265]. In our simulations, graphene nanosheet was presented as a two-dimensional honeycomb, where its aromatic carbon atoms featured van der Waals and hydrophobic interactions. In contrast, graphene oxide was modeled by introducing defects, epoxidations, hydroxylations, and carboxylations to its graphene backbone (Fig. 5.1). These modifications rendered the graphene oxide surface more hydrophilic in

physicochemistry and rugged in morphology than graphene.

2. Results

Differential binding of nanosheets with single amphiphiles – temperature varying DMD simulations. We first characterized the dynamics of single-molecular binding between the nanosheets of graphene derivatives and the amphiphiles. We performed DMD simulations at different temperatures and monitored the binding along the simulation trajectories. For example, in the case of graphene oxide and cellulose[266] binding, we observed three different regimes (Fig. 5.2). At low temperatures (Fig. 5.2 a), the molecular system had low potential energies and the cellulose stayed bound to the nanosheet with a high number of atomic contacts (N_c) occurring between the two species. At high temperatures (Fig. 5.2 c), the cellulose molecule dissociated from the nanosheet with higher potential energies and a low N_c value. The two species only occasionally formed contacts due to thermal fluctuations.

<center>Graphene   Graphene Oxide</center>

<center>**Natural Amphiphiles**</center>

<center>Cellulose Dimer $(C_6H_{10}O_5)_2$ Peptide: Tri-Alanine $(C_3H_7NO2)_3$ Palmitic Acid: $C_{16}H_{32}O_2$</center>
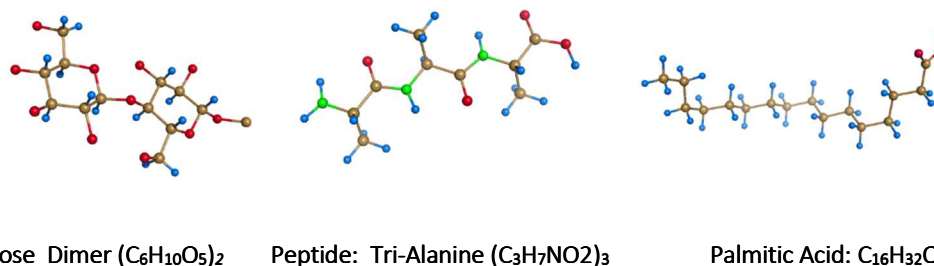
Figure 5.1. Simulation scheme of the nanostructures of graphene and graphene oxide nanosheets (top row) and the natural amphiphiles of a cellulose dimer, a tri-alanine peptide, and a palmitic acid (bottom row). Color schemes: brown - carbon, red - oxygen, blue - hydrogen, green - nitrogen.

Between these two extreme regimes, there existed a mid-point temperature, T_m, where the cellulose had approximately an equal probability of being bound and unbound to graphene oxide (Fig. 5.2 b). Interestingly, in the unbound state, the systems featured an intermediate energy state, which belonged to the excitation of a high-energy normal mode

due to harmonic constraint applied to confine the nanosheet (Fig. Appendix C1).

Therefore, the inter-molecular contact, N_c, rather than the potential energy, was a more appropriate parameter to monitor the binding. At T_m, the potential energies and inter-molecular N_c values displayed large and anti-correlated fluctuations, clearly resulting from the interplay of enthalpy and entropy. Here the contributions of entropy include freedoms in both translation and configuration. The values of T_m were used to quantify the binding affinities between the different amphiphiles and the nanosheets.

Accurate estimation of T_m requires sufficient sampling of the conformational space. We therefore applied replica exchange DMD simulations[265] (Methods) to enhance the sampling, where multiple simulations were running in parallel at different temperatures and the replica temperatures were subject to exchange periodically according to the Metropolis criteria[267]. A system in a kinetically trapped state has a chance to escape the local minimum by running at a higher temperature, thus enhancing the sampling. Based on the replica exchange simulations, we computed the thermodynamic parameters using the weighted histogram method (Methods)[268].

For both graphene and graphene oxide, we performed independent replica exchange DMD simulations of their binding to cellulose, tri-alanine, and palmitic acid. We computed the average N_c as a function of temperature (Fig. 5.3 a).
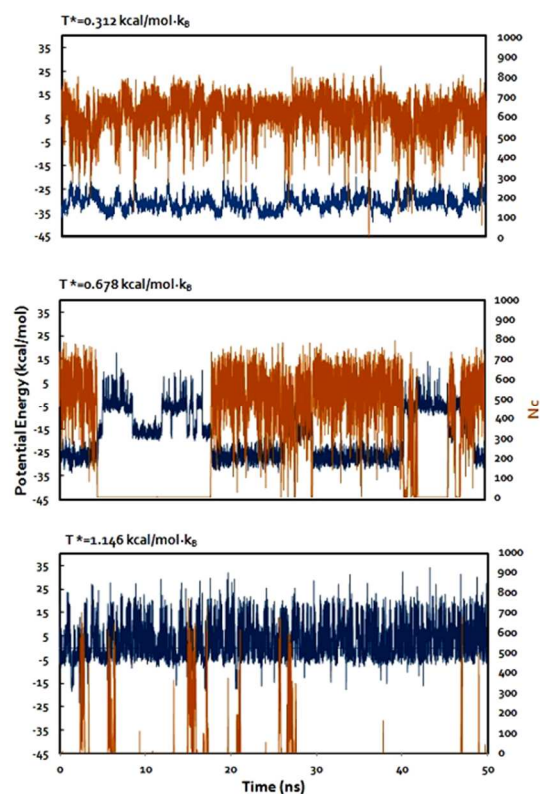
Figure 5.2. Binding simulation trajectories at different temperatures. Both potential energy (E, blue, left vertical axis) and number of atomic contacts (N_c, orange, right vertical axis) are shown for DMD simulations of cellulose-graphene oxide binding. Simulations at three different temperatures are shown: T^*=0.312 (a), 0.678 (b), and 1.146 (c), where the temperature unit is kcal/mol·k_B

For comparison between different molecular systems, we normalized the average N_c by its maximum value at low temperature to obtain the Q-value, which quantified the fraction of inter-molecular contacts. The amphiphiles showed a lower T_m when bound to graphene oxide than graphene, indicating a weaker binding associated with graphene oxide due to its various surface modifications that compromised inter-molecular hydrophobic interaction while encouraged electrostatic repulsion.

Interestingly, for both graphene and graphene oxide, palmitic acid displayed the strongest binding while tri-alanine showed the weakest (Fig. 5.3). The strong binding of palmitic acid to the nanosheets correlated with its longer molecular chain that consisted of a higher number of hydrocarbons and hence a greater degree of chain flexibility. The conformational flexibility of palmitic acid allowed its long hydrophobic tail to pack tightly against the nanosheet, taking advantage of contributions from van der Waals and hydrophobic interactions. Both the cellulose and the peptide were more rigid and hydrophilic compared to the palmitic acid tail. In addition, the higher melting temperature for cellulose on graphene, compared to that for peptide, can be attributed to stacking. In contrast to the ring-like structure of the cellulose, the peptide backbone of tri-alanine was unable to form many contacts with the nanosheet. This is in agreement with the molecular dynamics study by Katoch *et al.,* in which a lower binding affinity was observed when tryptophan residues were replaced by alanine. In the case of graphene oxide, the melting curves for cellulose and peptide were closer to each other (Fig. 5.3), suggesting that stacking was compromised by the functional groups of the nanosheet to shield its aromatic structure.

Differential binding of nanosheets with algal exudates – experiments. To complement the simulations, algal exudates were acquired from freshly cultured *Chlorella* sp. following a protocol developed in our lab[269]. The algal exudates were used to mimic the natural amphiphiles of cellulose, peptides, and fatty acids in the simulations. Graphene was synthesized using previously described chemical vapor deposition

method[270] while graphene oxide was produced using the modified Hummer's method[271]. Graphene-based materials exhibited strong Raman spectra due to the double resonance phenomenon[272]. Importantly, the overtone of disorder band (referred to as the 2D-band) exhibited two peaks at ~2690 cm^{-1} and ~2725 cm^{-1} (see Fig. 5.4 a).
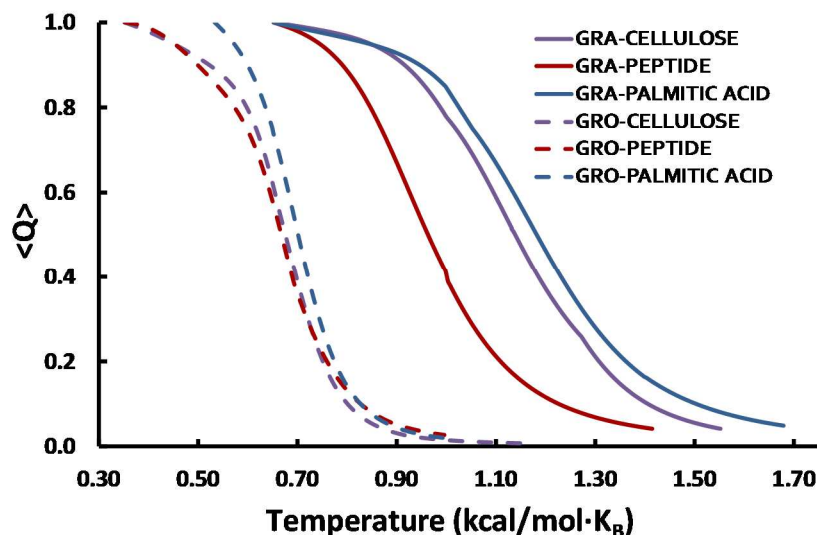

Figure 5.3. Differential binding affinities of natural amphiphiles with graphene derivatives. The average value of normalized fraction of contacts, $<Q>$, was computed as the function of temperatures (T^*) using the weighted histogram analysis method with replica exchange DMD simulations (Methods). The temperature dependence of $<Q>$ values illustrates the melting. For each of the three amphiphile species, the melting curves of both graphene oxide ("GRO", dashed) and graphene ("GRA", solid) are shown.

This band is highly sensitive to charge transfer from substrates, dopants or any adsorbents. We observed that the 2D-band in graphene upshifted upon exposure to the algal exudates, suggesting a possible charge transfer from graphene to algal exudates. However, no such charge transfer was observed in the case of graphene oxide, implying a

weaker interaction occurring between the graphene oxide and algal exudates (Fig. Appendix C2), in agreement with our simulations (Fig. 5.3). Furthermore, our Fourier transform infrared (FTIR) spectra (Fig. 5.4 b) showed that the exudate peaks were present and absent in the graphene and graphene oxide incubated with algal exudates and after washing with de-ionized water, consistent with both the Raman spectra and the simulations.

To further examine the binding kinetics of graphene and graphene oxide with algal exudates, we incubated the nanosheets with exudates in water and observed their precipitation at different temperatures (Methods). The absorbance peak of the algal exudates at 205 nm was monitored over time for both graphene and graphene oxide (Figs. 5.5 a, b). The normalized absorbance value corresponded to the total fraction of exudates and graphene (graphene oxide) still present in solution at a given time. This process was performed with fresh suspensions at both 30ºC and 35ºC. We also performed a control experiment of graphene and graphene oxide in the absence of algal exudates at both temperatures, and did not identify significant temperature dependence of the control precipitation over the temperature range examined.
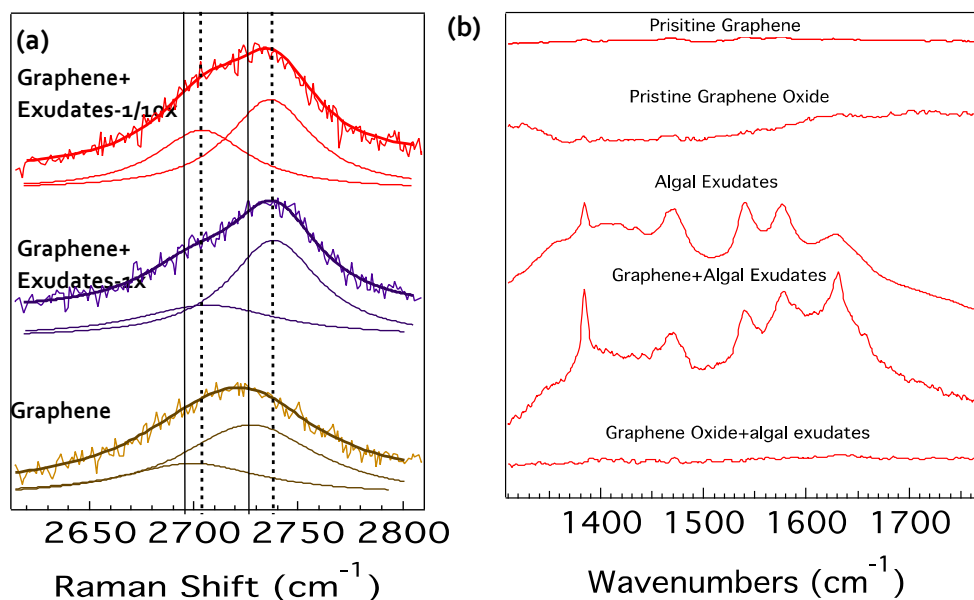
Figure 4.4. Raman (a) and FTIR (b) spectra of algal exudate-graphene/graphene oxide system. 1×: stock, 1/10×: ten-time diluted.

For both graphene and graphene oxide, algal exudates slowed the rate of precipitation at both temperatures. This general behavior is indicative of exudates binding with graphene and graphene oxide to render both types of nanosheets more water-soluble. The binding with algal exudates should also discourage π-stacking of the nanosheets, further slowing their rate of precipitation. The temperature-dependent behavior of graphene and graphene oxide with algal exudates displayed qualitatively the same trends – the overall difference in precipitation rate is due to the stark difference in hydrophobicity between graphene and graphene oxide. During the initial precipitation at 30ºC, both graphene and graphene oxide with exudates followed the control precipitation closely, indicating that under this temperature stacking of the nanosheets dominated

87

exudate-nanosheet interactions to favor precipitation. The suspensions at 35ºC showed less pronounced precipitations, reaching a complete suspension after 50 min incubation with the graphene oxide. At 240-min incubation with the graphene, while the suspension reached 60% of normalized absorbance at 30ºC, it registered 86% of normalized absorbance at 35ºC in the same time period. This behavior clearly confirmed that significant binding occurred between algal exudates and both graphene and graphene oxide, and this binding was further enhanced by elevated temperature.
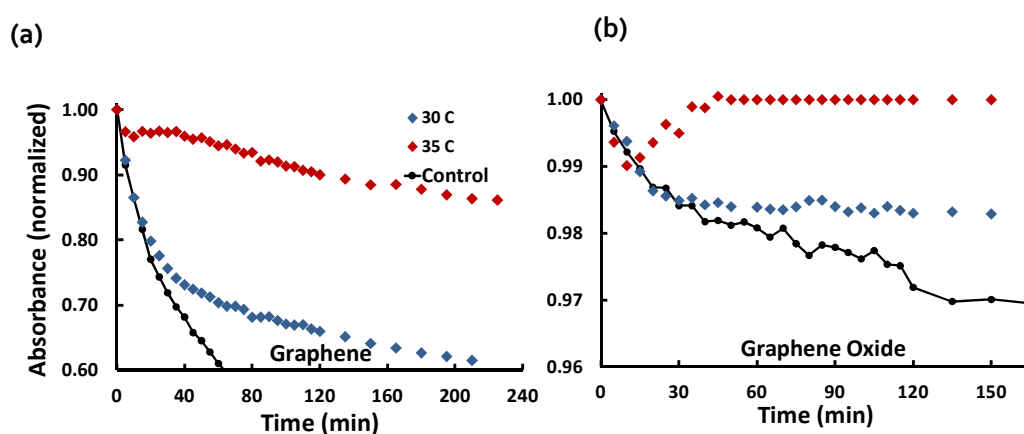

Figure 5.2. UV-Vis absorbance spectra of algal exudates mixed with graphene (a) and graphene oxide (b) measured at 30°C (blue) and 35°C (maroon). Control kinetics performed in the absence of exudates at 30ºC (with no significant difference seen at 35ºC) at concentrations equal to test samples.

Differential binding of nanosheets with multiple amphiphile species – DMD simulation. To model the binding of graphene derivatives with a collection of natural amphiphiles in biological and environmental media, we performed a constant-temperature DMD simulation of a graphene oxide nanosheet mixed with the three amphiphilie species simultaneously (Methods). We used the relative ratios of glucose to

88

peptide to palmitic acid as found in algal exudates,[273] 7:3:1, and accordingly we included 14 cellulose, 6 peptide, and 2 palmitic acid molecules. The amphiphilic molecules were initially positioned away from the nanosheet (Fig. 5.6 a). We chose a simulation temperature $T \approx T_m$ of tri-alanine binding. This temperature allowed rapid equilibration while all molecules were able to bind to the graphene oxide nanosheet.

We then monitored the number density of molecules bound to the nanosheet along the simulation trajectory (Fig. 5.6 b). Due to their high concentrations, peptides and celluloses rapidly covered the nanosheet to form a nanosheet-amphiphile biocorona (0-8 ns; Figs. 4.6 a, b), which hindered the binding of palmitic acids. However, due to their relatively weak binding affinity, the peptides and celluloses on the nanosheet underwent rapid exchange with the molecules in solution to assume a "soft" biocorona[101]. Despite having the lowest concentration in the simulation, palmitic acids occasionally interacted with the dynamic biocorona under diffusion. Once the nanosheet was available, a palmitic acid bound to its surface and remained bound during the course of the simulation (e.g., > 25 ns; Fig. 5.6 b). As a result, the biocorona became "hardened" as evidenced by the smaller fluctuations of the number of nanosheet-bound molecules after both palmitic acids were attached to the surface (t > 35 ns; Fig. 5.6 b). In the case of higher stoichiometric ratios of amphiphiles to the nanosheet, we expect a complete coverage of the nanosheet by strong binders like the palmitic acids to render a "hard" biocorona. Our results illustrate the general applicability of the Vroman effect for describing the binding kinetics of biomolecular species competing for graphene derivatives.

3. Discussion

We systematically studied the interactions of graphene derivatives with natural amphiphiles to elucidate the general fate of graphene nanostructures in biological and environmental milieu. Our computational studies showed that both graphene and graphene oxide could bind to the amphiphiles, although graphene oxide displayed a weaker binding capacity owing to its surface charge and surface functionalizations. Using algal exudates as a model system, our experimental characterizations confirmed the differential binding of graphene and graphene oxide for natural amphiphiles. Furthermore, our simulations revealed that natural amphiphiles of cellulose, peptide and palmitic acid -- owing to their differences in hydrocarbon content, conformational flexibility, and molecular geometry -- displayed distinct binding affinities for the graphene derivatives. Specifically, we were able to directly observe in our simulations, for the first time, a Vroman-like binding during which amphiphiles of different abundance and binding affinity rapidly competed for the graphene nanosheet surface; here amphiphiles of high abundance but low binding affinity readily covered the surface of the nanosheet to initiate a "soft" biocorona, while amphiphiles of low abundance but high affinity eventually took over to render a "hard" biocorona. This study offers a mechanistic basis for our understanding of the physicochemical properties and the fate and implications of graphene derivatives in biological and environmental matrices.
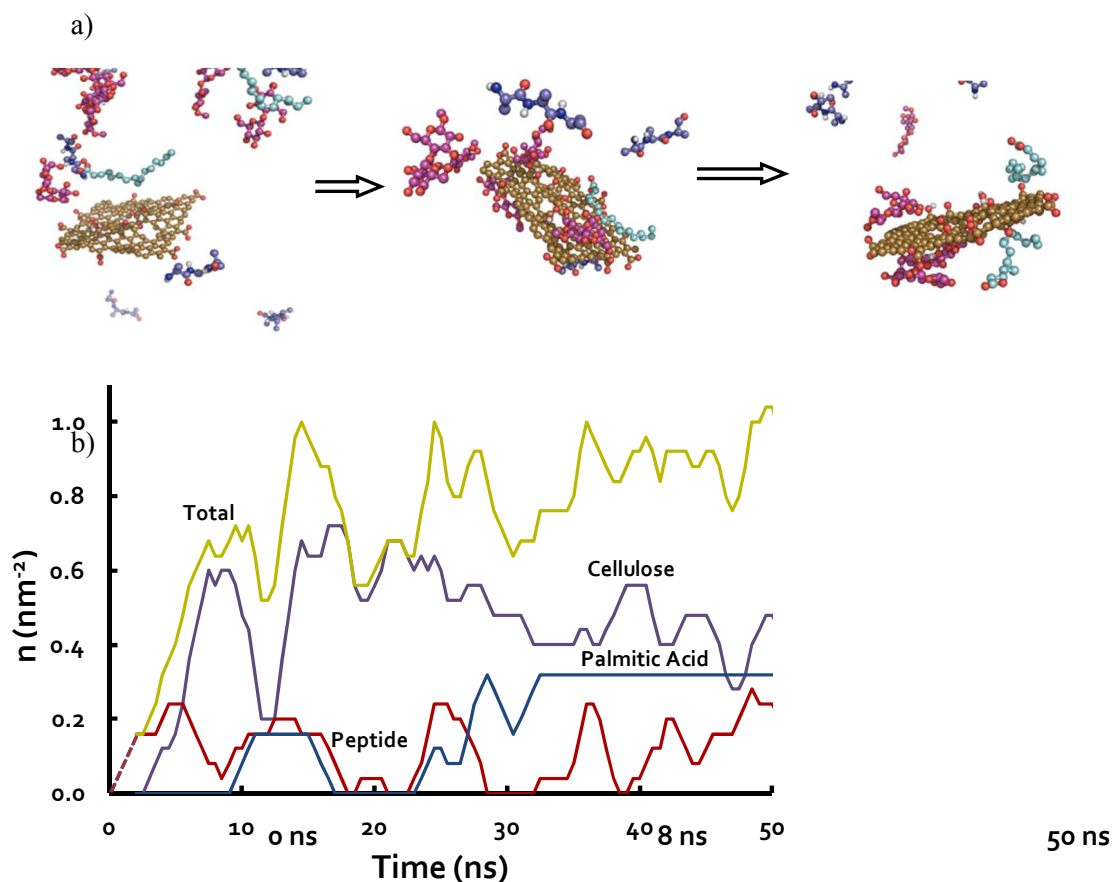
Figure 5.6. Vroman-like competitive binding of amphiphile mixture with graphene oxide. (a) The DMD simulation snapshots of the binding between graphene oxide and amphiphile mixture: t=0 ns, 8 ns, and 50 ns. (b) The number density of molecules, n, bound to the nanosheet is shown along the simulation trajectory.

4. Methods

Construction of the model systems. The graphene nanosheet was prepared using the VMD[274] carbon nanostructure builder plugin (www.ks.uiuc.edu/Research/vmd/plugins/nanotube). The dimension of the nanosheet was

set as 25 x 25 Å^2. The structure of graphene oxide was obtained by chemically editing the graphene nanosheet using Avogadro, a cross-platform molecule editor (avogadro.openmolecules.net)[275]. To mimic the experimentally-observed structural defects in graphene oxide[276–278], we included random vacancies in the graphene oxide matrix. We then introduced epoxide, hydroxyl, and carboxyl groups to the lattice in a stochastic manner while maintaining the valences of the composing carbon atoms. After the introduction of defects and chemical modifications, we performed energy minimization using the MMFF94s force field[279]. Because of the introduction of sp^3 carbons on the planner carbon latter, the graphene oxide nanosheet became non-planner after the energy minimization (Fig. 5.1).

The molecular structures of cellulose dimer, tri-alanine and palmitic acid were generated and minimized using open babel (openbabel.org)[280]. We adapted the MedusaScore force field[281], an extended Medusa force field[182] for small-molecule ligands, to model the inter-atomic interactions of biomolecules beyond proteins[282].

Simulation setup. The simulation was setup in a cubic box with each dimension of 100 Å. In our simulations, we applied harmonic constraints to the edge carbon atoms of graphene and graphene oxide with a weak spring constant k = 0.1 kcal/mol·Å^2. The rest of nanosheet atoms were free to move. For each of the molecular system, we first performed equilibration simulations of 5 ns, and then production simulations of at least 50 ns.

In DMD simulations, the temperature unit is kcal/mol·k_B. Here, k_B is the Boltzmann constant. For the replica exchange simulations, we used 14 replicas with different

temperatures to sample the conformational space. Ranges of temperatures used in replica exchange were from 0.65 to 1.55 for graphene-cellulose, 0.65 to 1.4 for graphene-peptide, 0.65 to 1.65 for graphene-palmitic acid, and from 0.35 to 1.2 for graphene oxide-cellulose, 0.35 to 1.0 for graphene oxide-peptide and 0.5 to 1.0 for graphene oxide-palmitic acid. The temperatures were adjusted to ensure sufficient exchange between replicas with neighboring temperatures and that the exchange rates were approximately equal.

To study competitive binding of the amphiphile mixtures, we placed a graphene oxide nanosheet together with 14 cellulose, 6 peptide and 2 palmitic acid molecules in a cubic box with the linear dimension of 110 Å. We followed previous report of algae exudate composition[273] to set up the molecular system. We performed the constant-temperature DMD simulation at $T = 0.67$ kcal/mol·Å^2 for 50 ns.

Inter-molecular contacts. We monitored inter-molecule interactions by measuring the number of atomic contacts between two molecules, N_c. Two atoms were counted as in contact if the inter-atomic distance was smaller than 6.5 Å. The fraction of inter-molecular contacts, Q, corresponded to N_c normalized by the maximum number of atomic contacts when two molecules were bound at low temperature.

Normal modes of the nanosheet. In our simulations, we constrained the nanosheets with harmonic constraints in order to direct monitor amphiphile binding without re-centering the molecular system around the graphene sheet. As a result, the constrained nanosheet can undergo collective motions, i.e. normal modes, which feature different frequencies and corresponding energies. At low temperatures, only the low-

energy modes that the atoms moved along approximately the same direction were observed. As the temperature increased, higher-energy normal modes could be excited (Fig. Appendix C1).

Weighted histogram analysis method (WHAM). The WHAM method utilizes multiple simulation trajectories with overlapping sampling along the reaction coordinates to self-consistently compute the density of states $\rho(E)$ by combining histograms from different simulation trajectories[283]. Given the density of states, the partition function can be computed: $Z = \int \rho(E)\exp(-E/k_BT)dE$. To compute any physical parameter as a function of temperature, we calculated the conditional probability $P(A\,|\,E)$ of observing a structure with the parameter of A at given energy E, evaluated from all simulation trajectories. The average RMSD as a function of temperature can be computed as $\langle A(T) \rangle = 1/Z \int A \cdot P(A\,|\,E)\rho(E)\exp(-E/k_BT)dEdA$.

Syntheses of graphene derivatives. Few-layer graphene samples were prepared using chemical vapor deposition technique. Briefly, 25 μm Ni foils were placed away from the center of tube furnace (diameter: 24 mm), which was maintained at 900°C under a flow of Ar (230 sccm) and H_2 (120 sccm). After 60 min, Ni foils were moved to the center and graphene was synthesized by decomposing methane (10 sccm) for 10 min at a reduced temperature (850°C). Subsequently, methane flow was shut off and the samples were moved away from the center. The furnace temperature was ramped down to 400°C at 5°C/min and was maintained at 400°C for 90 min. The H_2 flow was shut off immediately upon reaching 400°C, and the samples were cooled to room temperature under Ar flow.

For solvent exfoliation of graphene, bulk graphite (~1g) was dispersed in 100 mL of N-methyl-2-pyrrolidinone (NMP) and sonicated using 1/8" tip sonicator (Branson 250) at 100 W for 2 h. The resulting dispersion was filtered through a 0.45 μm nylon filter and re-suspended in 100 mL of fresh NMP. Subsequently, the solution was bath sonicated for 6 h and centrifuged at 500 rpm for 45 min. The supernatant was vacuum filtered using a 0.45 μm nylon filter. Finally, the filtered powder was washed several times using deionized water to remove residual NMP. We used modified Hummer's method to prepare graphene oxide.

Briefly, exfoliated graphene (2 g) was dispersed in concentrated H_2SO_4 (46 mL). $KMnO_4$ (6 g) was added gradually with stirring in an ice bath. The mixture was then stirred at 35°C for 2 h, and deionized water (100 mL) was added. In 1 h, the reaction was terminated by the addition of a large amount of deionized water (300 mL) and 30% H_2O_2 solution (5 mL), causing violent effervescence and an increase in temperature to 100ºC, after which the color of the suspension changed to bright yellow. The suspension was washed with 1:10 HCl solution (500 mL) in order to remove metal ions by filter paper and funnel. The paste collected from the filter paper was dried at 60°C, until it became agglomerated. The agglomeration was washed several times with deionized water and air-dried to obtain graphene oxide samples.

Micro-Raman and FTIR measurement. Micro-Raman spectra were collected using a Dilor XY triple grating spectrometer equipped with TE-cooled CCD coupled to an Ar^+ laser excitation at 514.5 nm. The Raman spectrum of graphene oxide exhibited a weaker 2D-band compared to graphene. Nonetheless, we observed that the 2D-band for

graphene oxide samples did not upshift (unlike graphene) upon incubation with algal exudates (see Appendic C Fig. C2). For FTIR measurements, the samples were incubated with algal exudates for 12 h. Subsequently, the samples were washed using de-ionized water to remove any unadsorbed exudates. For graphene oxide, the samples were centrifuged at 3,000 rpm for 2 h and the obtained pellets were washed in deionized water. Finally, the sample was air-dried overnight for performing FTIR studies. The dried samples were encased in a KBr matrix and their FTIR spectra were measured using a Bruker IFS v66 spectrometer.

UV-Vis measurement. For UV-Vis kinetics measurements, graphene was suspended in water from dry state and both graphene and graphene oxide (both 10 μg/mL) were bath sonicated for 5 min. Algal exudates, prepared as described previously[269], were then added and the resulting suspensions were immediately placed in a temperature-controlled UV-Vis spectrophotometer (Cary 300-Bio, Varian Instruments). The maximum temperature fluctuation of the device was ±0.02ºC.

CHAPTER 6

PROTEIN AGGREGATION DEPENDANCE ON NANOPARTICLE-PROTEIN INTERACTION STRENGTH AND RELATIVE CONCENTRATION

In preparation.

1. Introduction

The interactions between proteins and NPs can also change protein structures and affect their corresponding functions[102,284], leading to possible toxic effects[116,118,285–287]. Therefore, it is important to understand corona formation and its impact on absorbed proteins in order to enable the vast applications of nanomedicine.

Because of a high concentration of proteins in the NP corona, a polymeric NP has been found to promote amyloid aggregation of beta-2 microglobulin, an amyloidogenic protein in serum[130]. Given the capability of NPs to cross the blood-brain-barrier[195,288–291], many efforts has also been devoted to study the effect of NPs on protein aggregations in neurodegenerative diseases, such as of amyloid-beta peptide (Aβ) in Alzheimer's disease (AD) [128–134,292–294]. The amyloid aggregate of proteins is characterized by a common cross-β structure[295,125–127,296,297]. Many recent studies suggest that oligomers populated along the aggregation pathway rather than the final amyloid fibril are cytotoxic[298–300]. Motivated by advances in nanotechnology and nanomedicine, many studies focused on understanding impact of NPs with various physicochemical properties on protein aggregation in order to reduce protein aggregation upon NP exposure and also to find novel NPs that may inhibit aggregation.

Given the diversity of NPs and proteins used in previous experimental studies, both aggregation inhibition and promotion effects have been reported. Amyloid

aggregation is a nucleation process, which is characterized by a lag time followed by sigmoid increase of amyloid fibrils[301]. Sara Linse et al. showed that copolymer particles, cerium oxide particles, quantum dots, and carbon nanotubes enhance fibril formation of b$_2$-microglobulin[130] with shortened aggregation lag time. Similar effect was seen when TiO$_2$ nanoparticles were introduced to the Aβ solution[132]. It has been suggested that NPs locally increased protein concentration which enhanced the probability of the formation of critical aggregation nucleus[301]. On the other hand, Cabaleiro-Lago et al. found that Aβ and islet amyloid peptide (IAPP) fibrillation was inhibited by adding polymeric NPs[130,133]. Guo et al. observed that singlewalled carbon nanotubes (SWCNT) prevent the formation of β-sheets of Aβ[302]. Similarly, Liao et al. showed that negatively charged gold nanoparticles inhibit Aβ fibrillization and relieved Aβ toxicity to neuroblastoma[134]. Interestingly, it was also noticed that a given NP might have a dual effect on protein aggregation depending on the relative concentration ratio between protein monomers and NPs (surface area). Since the protein to NP ratio determines the partition of proteins in solution and on NP surface, Cabaleiro-Lago et al. observed that amyloid aggregation of Aβ was promoted at a high protein to NP surface ratio and inhibited at the lower ratio (i.e., lower concentration of protein on NP surface)[131]. In order to fully harness the beneficial effects and reduce the adverse effects of NPs, it is necessary to uncover the driving forces that dictate the drastically different impacts of NPs on protein aggregation in addition to the kinetic effects.

Depending on their core materials and surface coatings, various NPs have distinct physicochemical properties and thus different interactions with proteins. We hypothesize

that the complex aggregation behavior in the presence of NPs is also determined by the inter NP-protein interactions. Using coarse-grained modeling with discrete molecular dynamics (DMD) simulations, Auer et al. studied the dependence of protein aggregation on different protein-protein and protein-NP interactions. The NP was modeled as a single bead with attractive interaction to proteins. They observed that protein aggregation is enhanced by a stronger protein-NP interactions and NP surface served as fibrillization catalyst[293]. However, the experimentally observed inhibition of protein aggregation was not observed. We postulate that modeling NP as a single bead cannot capture some important aspect of surface diffusion, such as the surface roughness due to atomic surface. In this study, we explicitly modeled the surface atoms of a spherical NP (two atoms layers) and used Aβ as the model protein system, which is modeled by a simplified two-bead-per-residue model[303]. We probed the effect of varied interaction strength between NP and protein on Aβ aggregation. Using DMD simulations, we observed an optimal NP-protein interaction strength with which Aβ has the maximum aggregation on NP surface. With interactions weaker than the optimal value the increases of NP-protein interaction promotes aggregation. As the interaction strength is stronger than optimal value, Aβ aggregation was inhibited on NP surface. We also studied the concentration dependence of Aβ aggregation on NP surface. Our results shed light on the diverse effect of NPs on protein aggregation.

2. Results and Discussion

In our two-bead-per-residue model[188] for Aβ peptides, each amino acid is represented by the backbone Cα and sidechain Cβ beads model both intra- and inter-chain interaction, which has been extensively used by us and others to study protein aggregation *in silico*[190] and the interaction potential is ε. We used the NMR structure of Aβ (PDB ID: 1BA4) βs the reference structure, where the protein is partially helical (Fig. 6.1 A). In addition, we also included hydrogen bond interaction between backbone Cα beads (**Methods**). For the NP, we modeled the surface atoms as approximately closed-packed on the 2D spherical surface with a diameter of 100 Å (**Methods**). We assigned non-specific attractive interactions between NP and protein atoms with the interaction potential of ε_{NP}. We kept NP atoms static and proteins free to move in DMD simulations.

Folding of Aβ monomer in solution. Before modeling Aβ aggregation under the influence of NP, we first characterized the folding dynamics of Aβ monomer in the absence of NP (or in solution) using replica exchange simulations[304] (Methods). Eight replica were used with temperatures ranging from 0.45 to 0.80 ε/K_B, and the incensement of 0.05 ε/K_B, where ε is the interaction of Gō potential and K_B is the Boltzmann constant. We used weighted histogram analysis method (WHAM)[283] to calculate heat capacity (C_v) and radius of gyration (R_g) (Fig. 6.1).We observed two peaks in the C_v plot as the function of temperature (Fig. 6.1 B). Examination of Aβ structures at low temperatures (T < 0.55 ε/K_B) simulations indicated that the C-terminal forms non-native helixes (Fig. 6.1 B).
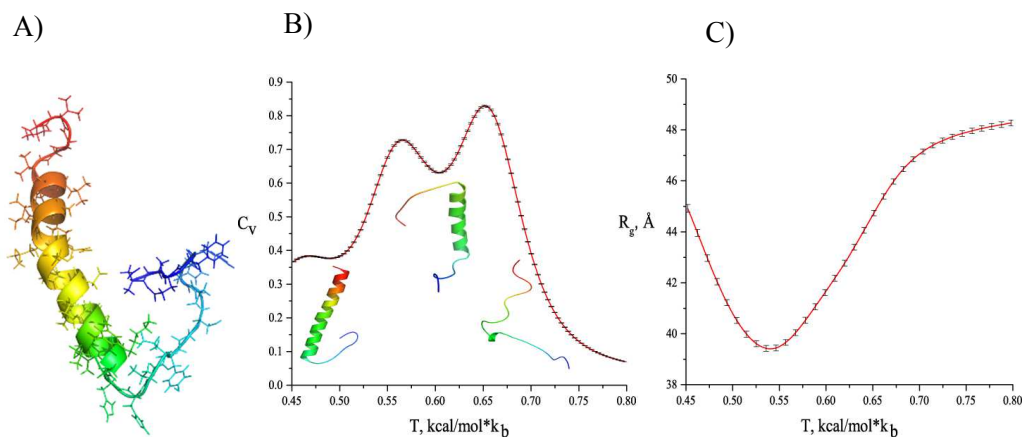
Figure 6.1. Protein stability curves. A) Amyloid β_{1-40} starting structure B) Heat capacity dependence on temperature of the protein in solution with depicted corresponding structure. C) Radius of gyration vs. temperature

The first peak at temperature T = 0.55 ε/K_B corresponds to melting of the non-native C-terminal helix. Due to the rigidity of a single helix, the unfolding of the non-native C-terminal helix leads to the decreases of R_g (Fig. 6.1 C). As the temperature increases further, the native helix starts to unfold into random coil and the R_g of Aβ increases. Therefore, the second C_v peak at 0.65 ε/K_B corresponds to the melting temperature, T_m. It is known that protein needs to be partially unfolded in order to form β-sheet rich aggregates[298]. To facilitate the observation of protein aggregation in simulations, we performed our aggregation simulations at temperature T=0.655 ε/K_B which is slightly above T_m.

Aggregation of Aβ petides on NP surface with different interaction strengths. Understanding how NP-protein interaction strength ε_{NP} influences the formation of amyloid aggregates is one of the key questions of this study. We varied the interaction strength ε_{NP} from 0.1ε to 0.7ε with the increment of 0.1ε. Ten Aβ monomers were

randomly positioned in the vicinity of the spherical NP. For each ε_{NP}, we performed 50 independent DMD simulations with different initial positions and velocities. To quantify the aggregation process on the NP surface, we monitored the average number residues per chain that form inter-chain β-sheet like structures on NP surface, $N_{\beta\text{-}Res}$ (Methods). Here, we only included those Aβ peptides that were bound to the NP surface. By averaging over 50 DMD runs, we obtained the average $N_{\beta\text{-}Res}$ as the function of simulation time (Fig. 6.2 A). Usually, protein aggregation in solution is characterized by a lag time phase followed by a fast elongation phase[305–307].

In our simulations, we didn't observe the lag time phase. We believe that due to a high local concentration of proteins on NP surface and the fact that we simulate at a denaturing temperature, the nucleation process is negligible. In our simulations, we observed that the aggregation reached plateau after a rapid elongation phase. For interactions ε_{NP} less than 0.3 ε, we found that the $N_{\beta\text{-}Res}$ has larger fluctuations compared to simulations with stronger NP-protein attractions. We found that large fluctuations resulted from a small number of proteins on NP surface due to weak NP-protein aggregation (Fig. D2).
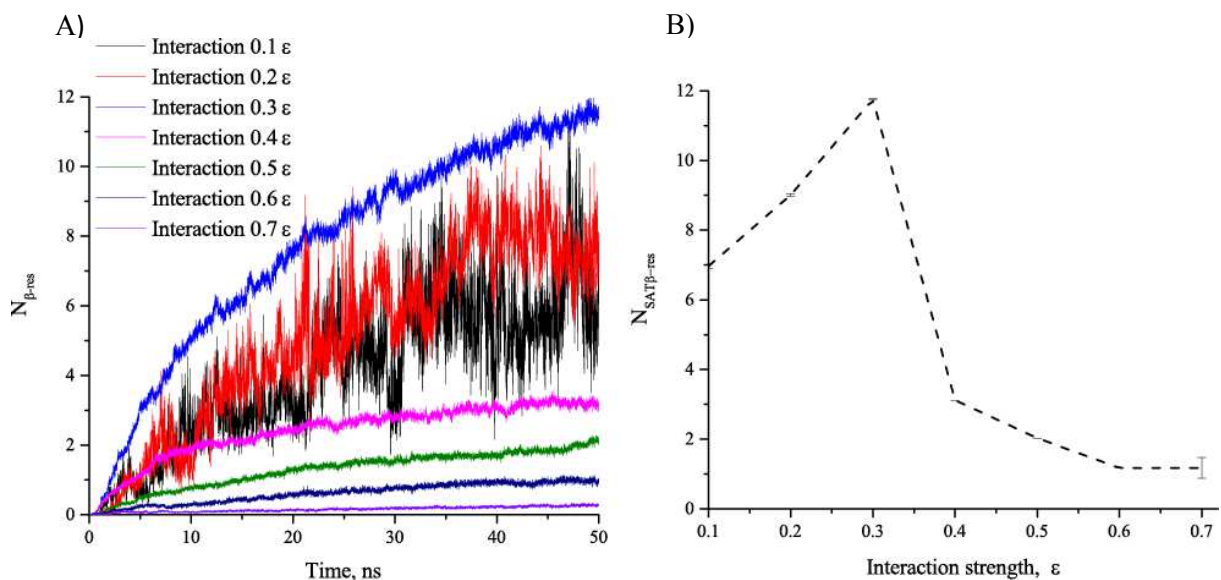
Figure 6.2. Aggregation on nanoparticle surface. A) Number of residues forming β-sheets per chain on NP surface B) Maximum number of residues in β-sheet structures per chain on NP surface

To quantify the aggregation process, we used the sigmoidal function (**Methods**), routinely used to fit experimental protein aggregation data[308], to fit computationally derived aggregation data (Fig. D1). From the fitting analysis, we obtained the maximal $N_{\beta\text{-}Res}$ as the function of NP-protein interaction strength ε_{NP} (Fig 2B). .We found that $N_{\beta\text{-}Res}$, which quantifies the average amount of β-sheet aggregation per chain on NP surface, has a maximal value near $\varepsilon_{NP} = 0.3\ \varepsilon$. When $\varepsilon_{NP} < 0.3\ \varepsilon$, increased NP-protein attraction leads to increased concentration of proteins bound to surface, which in turn enhance aggregation. As ε_{NP} is stronger than $0.3\ \varepsilon$, the increased interaction between NP surface atoms and proteins slowed down the diffusion of proteins on NP surface (Figure 6.4), resulting in reduced aggregation on NP surface (Fig 6.2 B).
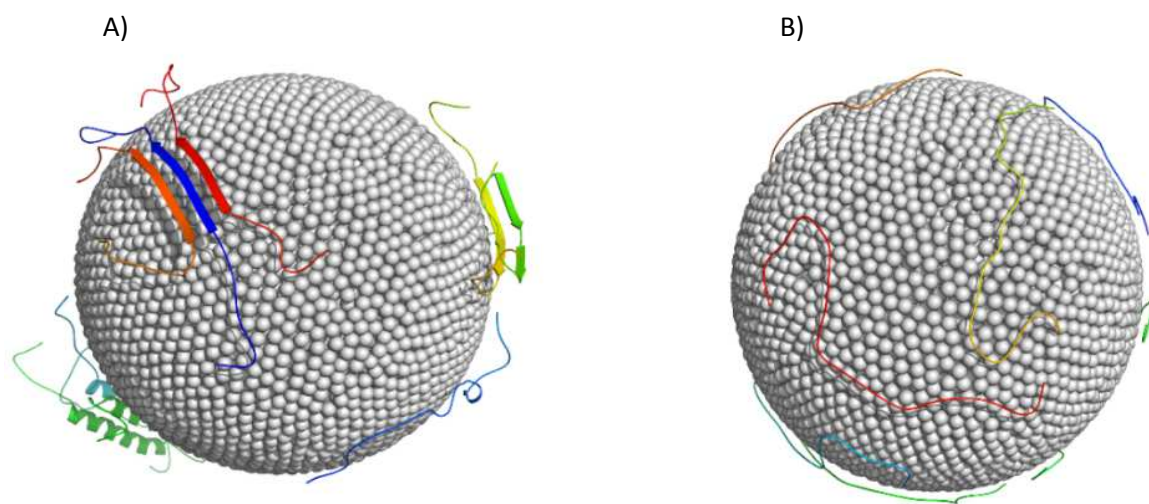
Figure 6.3. Proteins on nanoparticle surface. A) Formed β-sheet aggregates on nanoparticle surface at interaction strength of 0.3 ε B) Denatured protein on nanoparticle surface at interaction strength of 0.7 ε

The diffusion of proteins on the surface is governed by Arrhenius-type equation[309]:

$$D=D_0*\exp(-Q_a/k_bT) \qquad (6.1)$$

Where $Q_a =n*E$ is the activation energy and n is the number of NP surface atoms in contact with the protein residue (bead). The linear fit (Fig. 6.4 inset) gave us value of $Q_a/k_bT = 5.88$ (Appendix D Table D1) from which we calculated the n to be 4, meaning that the residue needs to break 4 bonds in order to make the next hop.

Visualized protein aggregation and structure configuration for interaction strengths of 0.3 ε and 0.7 ε are showed on Figure 6.3 A, B. Next, we examine the folding of NP monomer on NP surface with $\varepsilon_{NP} = 0.3 \varepsilon$
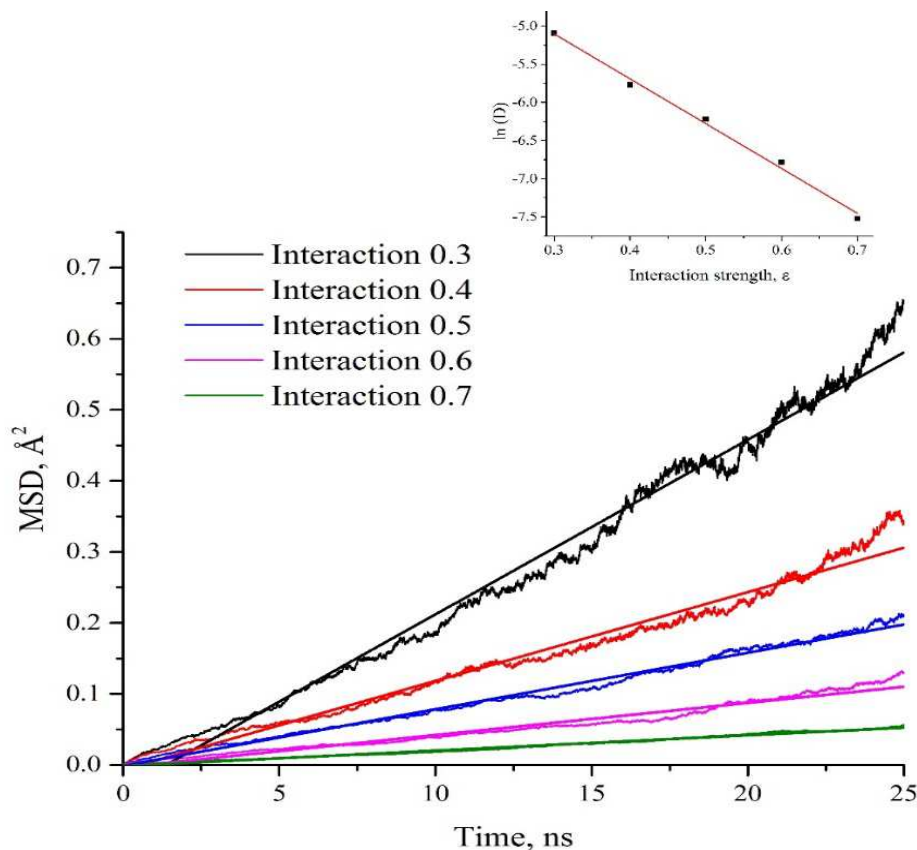
Figure 6.4. Diffusion on nanoparticle surface. Mean square deviation (MSD) vs time of the protein on nanoparticle surface. Diffusion coefficient dependence on interaction strength (ln inline plot) fitted with $\ln(D)=\ln(D_0)-k*\text{Interaction}$.

Aβ monomer is destabilized on NP surface. We placed an Aβ monomer on the NP surface with $\varepsilon_{NP} = 0.3\varepsilon$ and performed replica exchange DMD simulations. Using WHAM, we estimated the specific heat at the function of temperature (Fig. 6.5). Compared to the Aβ in solution, we noticed a shift of T_m (the highest peak) to lower

temperature (Fig. 6.5). The destabilization of protein on the NP surface is possibly due to stabilization of the unfolded state, where the protein makes more contacts with the NP. Interestingly, there is a shoulder in the specific heat near temperature ~0.75 ε/K_B.

By calculating the probability of the protein in contact with NP, we found that this
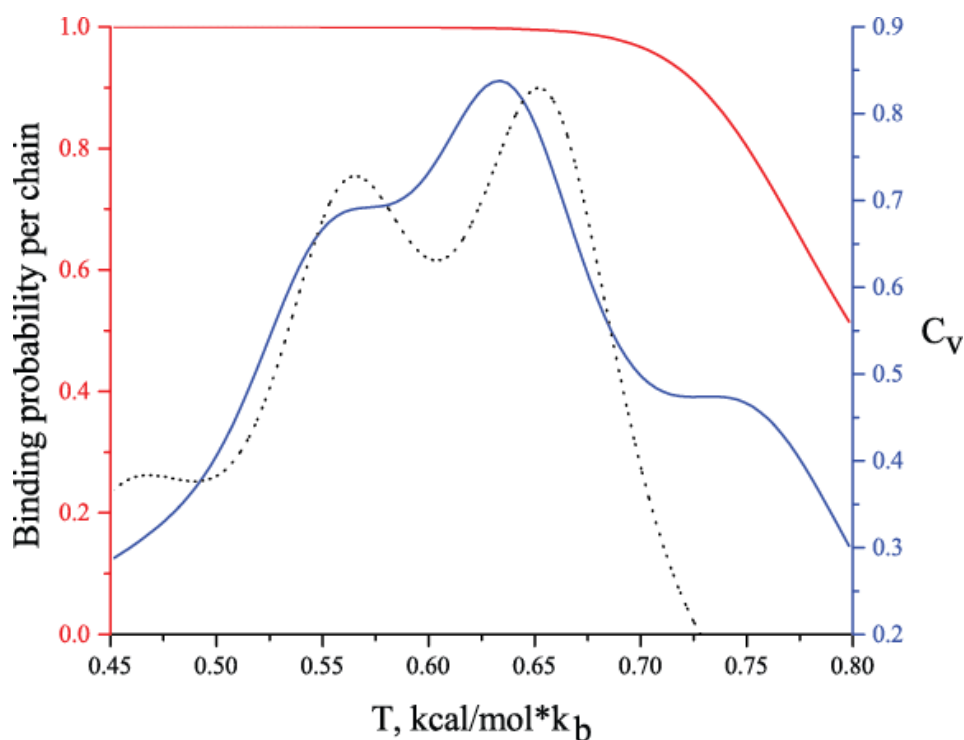
shoulder of C_v at high temperature corresponds to the dissociation of Aβ from the NP surface, T_d.

Figure 6.5. Stability of protein on nanoparticle surface. Heat capacity peaks moved towards lower temperatures (blue line) relative to heat capacity curve of the protein in solution (dashed line), indicating destabilization of protein structure due to nanoparticle surface binding. Emergence of the third peak at T=0.755 is reflection of the protein detaching from the nanoparticle surface (red line).

Therefore, at this intermediate NP-protein interaction strength $\varepsilon_{NP} = 0.3\varepsilon$, the protein was more destabilized on NP surface compared to in solution but still able to diffuse on surface, which in turn promoted the formation of Aβ aggregates (e.g., the snapshot of Aβ aggregates as in Fig 6.3A).
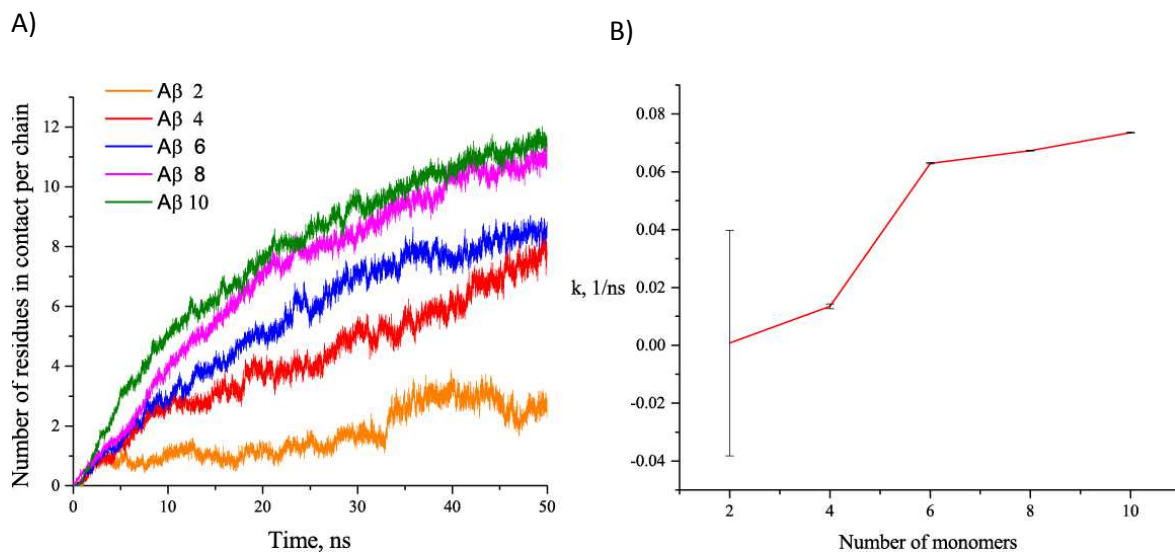

Figure 6.6. Protein aggregation dependence on concentration. A) Number of residues per chain in β sheet at interaction strength of 0.3 ε. B) Elongation rate dependence on number of monomers placed randomly onto nanoparticle surface.

The concentration-dependence of Aβ aggregation on NP surface. Our aggregation simulations suggested that with relatively weak NP-protein interaction the increased aggregation with increasing ε_{NP} is due to increased proteins on surface. Next, we performed DMD simulations to evaluate the concentration-dependence of Aβ aggregation on NP surface with the same interaction strength $\varepsilon_{NP} = 0.3\varepsilon$. We increased protein concentration from 2 to 10 monomers on NP surface. In each concentration, we performed 50 independent DMD simulations and compute the average $N_{\beta\text{-}Res}$ as the

function of time (Fig 6.6 A). Fitted with sigmoidal curves, we obtained the maximum amount of aggregates and the elongation rates, K_e of $7.92*10^{-4}$, 0.0135, 0.0629, 0.0673, 0.0735 ns^{-1} in the case of 2, 4, 6, 8 and 10 monomeres, respectively (Fig 6.6 B).

Figure 6.7. Competition of protein aggregation on NP surface and in solution. Lag time histograms of amyloid beta aggregation in bulk with interaction switched off a) and at interaction
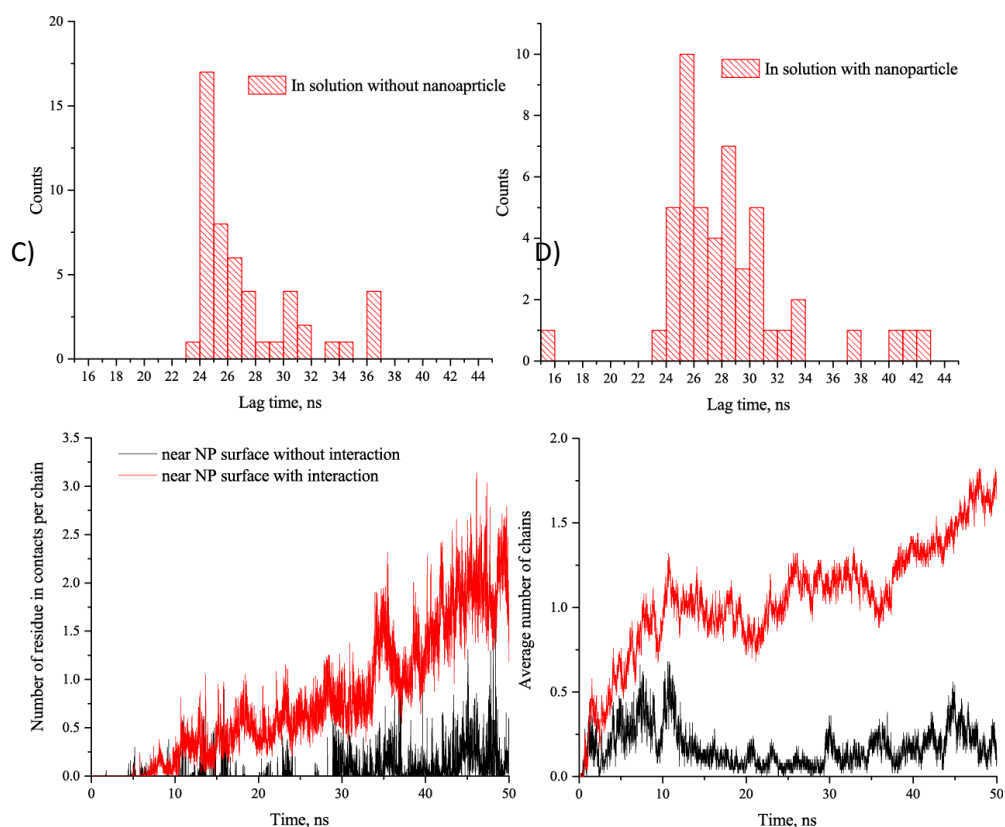
strength of -0.225kcal/mol. Aggregation trajectories of amyloid beta in vicinity of nanoparticle surface with interaction switched off (black) and on (red) c). Average number of chains in vicinity of nanoparticle surface over time d).

Our results suggested that the elongation rate K_e increased with increased protein concentration. Interestingly, there is a transition of K_e between four and six monomers on NP surface, after which the increase in concentration didn't have significant effect onto the elongation rate. We postulate that this transition between slow and fast elongation rate is possibly due to the protein cooperativity and reduced conformational entropy.

Competition of Aβ aggregation on NP surface and in solution. To further our understanding of protein aggregation in presence of nanoparticles, we conducted set of simulations with 6 Aβ monomers. Monomers were placed randomly away from nanoparticle surface. Firstly we simulated the system without assigned interactions, and then compared results when interaction strength was 0.225 kcal/mol. At this protein to nanoparticle ratio (6:1), we observed that protein aggregation lag time in solution away from nanoparticle surface was shorter (24 ns) compared to the one when weak interaction strength was assigned (26 ns) (Fig 6.7 A and 6.7 B). This is due to decreased local concentration in the bulk in presence of protein-nanoparticle interaction (Fig. 6.7 D). Also, after elongation phase proceeded at this concentration ratio, the influence of weak nanoparticle interaction onto protein aggregation dynamics in the bulk compared to the case when interaction was turned off was negligible (similar aggregation curve profile Fig. D3 A, B and distribution of average number of residues in beta sheets per chain Fig. D4 A, B). Contrary to the bulk, protein aggregation was observed in the vicinity of the nanoparticle when interaction was switched on, while lag time was diffusion limited (Fig. 6.7 C). This result implies that at higher protein to nanoparticle concentration ratios, bulk

diffusion time to reach nanoparticle surface would be lowered and weak interactions could promote protein aggregation, creating locally crowded environment. In the case of lower protein to nanoparticle concentration ratios, attractive interaction of nanoparticle would keep proteins in its vicinity, but with lower local concentration, while depleting it's concentration from the bulk. This would lead to two distinct aggregation processes: one that would take place on the surface of NP and the other in the bulk, with two distinct aggregation rates-one on the 2D nanoparticle surface k_{NP} and the other in solution $k_{sol.}$
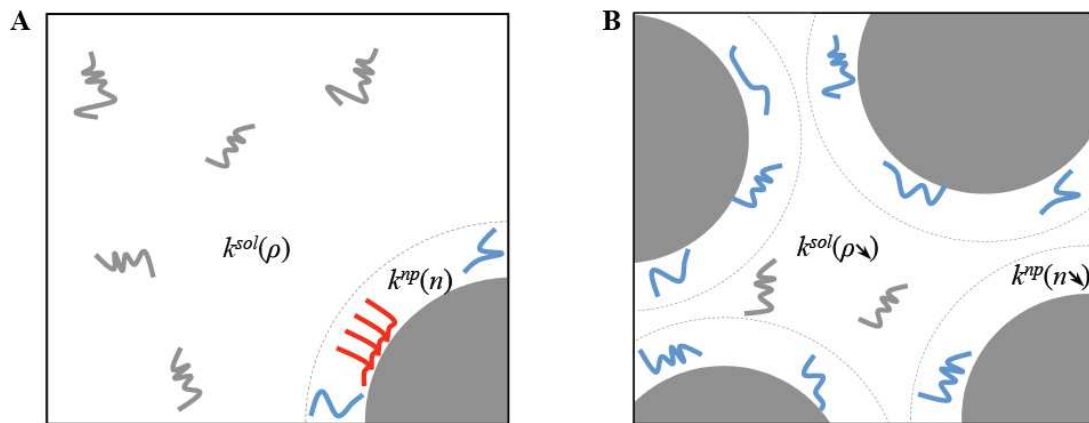
Figure 6.8. Mechanism of NP influence on protein aggregation. A) Weak interaction with high protein to NP ratio at critical number of proteins in vicinity of NP surface n^* such that $k_{NP}(n^*)>k_{sol}$ having promoting effect on protein aggregation B) Weak interaction with low protein to NP ratio hinders aggregation due to reduction of protein from solution and small number of bound protein (n) to each NP having hindering effect on protein aggregation

These rate constants would depend on protein concentration (Fig. 6.6 B). Aggregation in the bulk would be hindered due to reduction of protein caused by nanoparticles attracting the protein near their surface, while the aggregation on the nanoparticle surface would be alleviated due to the lower relative concentration ratio

between proteins and individual nanoparticle (Fig. 6.6 A, B) . Thus, we conclude that the weak interaction between NP and protein can promote or hinder protein aggregation depending on relative concentration ratio between protein and nanoparticle (Fig. 6.8 A). On the contrary, in the case of the strong NP-protein interaction, the protein aggregation would be hindered independently of the relative concentration ratio (Fig. 6.8 B).

3. Conclusion

In summary, our computational results showed that protein aggregation could be promoted or hindered in the presence of the nanomaterial depending on the interaction strength and relative concentration ratios between the protein and nanoparticle. In our DMD simulation study, we observed that as we increase interaction up to the turning point (Fig. 6.2 B), aggregation is promoted, after which it becomes hindered. Studies showed that graphene oxide sheets, carbon nanotubes and negatively charged gold nanoparticles that strongly interact with the Aβ hinder its aggregation[134,294,310]. Also, the study conducted by Cabaleiro-Lago et al. on Aβ aggregation in presence of polystyrene NPs, discovered dual effect of NPs on aggregation propensity related to relative concentration ratios between the protein and polystyrene nanoparticles[131]. Another study on scMN protein[128], revealed that presence of copolymer nanoparticles accelerated aggregation of more thermally stable scMN mutants, while hindered aggregation of the less stable ones. Authors argued that less stable mutants when in contact with nanoparticle, are prone to unfold and establish more contacts with the nanoparticle's surface, increasing the interaction strength and residence time compared to the more

stable mutants. These studies are in agreement with our prediction that as interaction increases after the certain turning point (in our model 0.3 kcal/mol Fig. 6.2B, a nanoparticle has stronger effect in hindering fibrillation process. Also, we found that weak interactions locally increase protein concentration, and in that way locally promote aggregation. Because amyloid-beta has a strong potential to form nuclear seed[308], effect of weakly binding nanoparticles like SiO_2, ZrO_2, CeO_2, C_{60} and C_{70} doesn't influence greatly lag time[132] and aggregation process, which we observed in our computational studies (Fig. 6.7 A, B and Appendix D4). Study on IAPP aggregation in presence of copolymer particles[133] revealed that residence time of the protein on surface of 85:15 and 50:50 NiPAM:BAM was of the same order, 85:15 copolymer nanoparticles had significantly bigger effect in preventing IAPP aggregation than the 50:50 NiPAM:BAM. Because of the specific interaction nature between IAPP and NiPAM:BAM our model was unable to explain this behavior in terms of the interaction strength. Although, further studies are needed to address specificity of nanoparticle-protein interaction and its influence onto aggregation, our model can explain why some nanoparticles are better in promoting or hindering protein fibrilization process, depending on the strength of mutual interaction.

4. Methods

Nanoparticle Model. Nanoparticle was modeled as two layers close packed all atom spherical nanoparticle of D=100 Å diameter. The VDW radius of atom was considered to be r=1.8 Å. Number of atoms calculated needed to form 2-layered closed

packing was N~5217. To determine this number we used formula $N=(D^2+(D-2r\sqrt{3}/2)^2)\cdot\rho_{2d}/r^2$, where $\rho_{2d}=0.9069$. Atoms were uniformly distributed around the center in θ and φ coordinates, while in **r** direction distribution was Gaussian centered at 50 Å and with standard deviation of 7 Å. Then simulation was run at temperature of 0.6 kcal/mol k_b for 100 ns, then 0.7 kcal/mol k_b for next 50 ns and at 0.85 kcal/mol k_b for the last 50 ns, when atoms formed closely packed two layer nanoparticle (Appendix D5). To constraint sphere radius to 50 Å, we assigned infinite well bounded at 46.88 Å and 50 Å from the virtual atom at the center.

Two-Bead Model of Protein. We modeled Ab protein (1BA4.pdb) using two-bead per residue model. Each amino acid is modeled using one bead for C-α (backbone carbon) and another one for C-β (side chain). Intra-molecular bonds along peptide are assigned to reflect protein geometry. Side chain-side chain interactions were modeled using structure-based potential, which favors observed native state interactions. The interaction strength between native contacts was set to $\varepsilon=1$ kcal/mol, while attractions between C-β atoms were assigned with hard-core distance of $D_{hc}=3$ Å and interaction range $D_{IR}=7.5$ Å. Also, hydrogen bonds are included in this model between backbone atoms[189]. Each C-α can form maximum two hydrogen bonds with other C-α atom, and two bonds formed by one C-α are co-linear in order to model the angular dependence of hydrogen bonds. Other inter-atomic interactions are modeled by simple hard-core distance of 3 Å.

Assigned Interactions Between Nanoparticle and Protein Residues. Attractive interactions between each nanoparticle atom and each residue atom were assigned with

distance range D_{IR}=5.75 Å, and hard-core distance of D_{hc}=3.6 Å. Assigned interactions didn't differentiate between different residues, i.e. they were non-specific (steps: D_{hc}=3.600000 3.800000 1.000000 4.300000 1.000000 4.550000 0.100000 5.250000 0.020000 D_{IR}=5.750000 ε_{in}). Attractive potentials used were ε_{in} = -0.1, -0.2, -0.3, -0.4, -0.5, -0.6 and -0.7 kcal/mol.

Simulation Set Up.:

Amyloid-β Stability In Solution. Coarse-grained two-bead residue of protein was used. It was immersed in 200x200x200 Å^3 simulation box with periodic boundary conditions. Firstly system was equilibrated at 0.45 kcal/mol k_b for 5 ns and then eight replica exchange DMD simulations were run (0.45, 0.50, 0.55, 0.60, 0.65, 0.70, 0.75, 0.80, and 0.85 kcal/mol k_b) for 3000000 time steps, which are approximately 150 ns. Using weighted histogram analysis method we calculated the heat capacity and radius of gyration.

Amyloid-β Aggregation On Nanoparticle Surface At Different Non-Specific Interaction Strengths And Concentrations. Ten monomers were randomly placed in proximity of nanoparticle surface at temperature of 0.655 kcal/mol k_b. Simulation box size was 205x205x205 Å^3 with periodic boundary conditions. Prior to running simulations, we equilibrated system at above-mentioned temperature for 5 ns. For each of interaction strengths (-0.1, -0.2, -0.3, -0.4, -0.5, -0.6, -0.7 kcal/mol), we ran 50 independent simulations with different initial conditions in duration of 50 ns. For each simulation we analyzed number of residues in contact on nanoparticle surface and in

solution. Similarly, 50 independent simulations were performed with different concentrations (2, 4, 6, 8 and 10 monomers).

Amyloid-β Stability On Nanoparticle Surface. Protein monomer was placed in simulation box of 205x205x205 Å^3 size with periodic boundary conditions and equilibrated at temperature of 0.45 kcal/mol k_b for 5 ns. After equilibration we ran eight replica exchange DMD simulations with temperatures ranging from 0.45-0.85 kcal/mol k_b. Using weighted histogram analysis method we calculated the heat capacity. Simulations were run for 150 ns.

Effect of Low Strength Nanoparticle-Protein Interaction On Protein Aggregation. To study how low interaction strength affects aggregation we placed six Aβ monomers randomly far away from nanoparticle. Size of simulation box in cases of switched on and switched off interaction was 205x205x205 Å^3 and simulations were firstly equilibrated for 5 ns. After equilibration simulation was run for 50 ns at temperature of 0.655 kcal/mol k_b. When interaction was switched off our $\varepsilon_{in}=0$ and when it was switched on $\varepsilon_{in}=-0.225$ kcal/mol. According to the distance of monomers from nanoparticle's center, we separated proteins onto the ones at the vicinity of surface (< 62.00 Å from the center) and in the bulk (> 62.00Å from the center). Number of independent simulations ran was 50, and for each simulation, the number of residues per chain in contact satisfying condition of β-sheet geometry was counted. Later this data was fitted with sigmoidal curves in order to get lag times for each simulation and then used to create lag time histograms in cases when attractive interaction was switched on and off.

Average Number of Residues in Contact. To quantify aggregation on nanoparticle surface we separated proteins that were on the surface from the protein in solution (bulk), by cut-off distance from the nanoparticle center $D_{cut-off}$=57.5 Å. Proteins with the distance less then $D_{cut-off}$ were categorized as the ones on the surface. In order to measure extent of aggregation we counted number of residues that were aligned to satisfy b-sheet (parallel and anti-parallel) geometry. We considered two residues (i,j) in contact if their distance was less than 7.5 Å, and condition that they form sheet structure if additionally (i+1,j+1) and (i-1,j-1) are in contact for parallel, or (i+1,j-1) and (i-1,j+1) are in contact for anti-parallel b-sheet. We ran 50 independent simulations with different initial conditions. For each simulation step it was calculated how many residues per chain are part of the sheet structure, and then it was averaged over 50 simulations at the same time step to get average number of residues in contact per chain at that instant.

Aggregation Curve Fitting. In order to get aggregation rate and aggregation maximum values we fitted aggregation curves in the case of protein placed at the nanoparticle surface with sigmoidal curves of the form: $y=(A-B)/(1+exp(-kt))+B$, using OriginLab 9.1 (Appendix D2). In case when protein were placed far away from the nanoparticle and let to diffuse to its surface the form of sigmoidal function we used was: $y=(A-B)/(1+exp(k(t-t_0)))+B$, again using OriginLab 9.1. Lag time t_{lag} was defined as $t_{lag}=t_0-2/k$, and calculated for each of 50 simulations, after which we created lag time histograms in OriginLab 9.1[313] (Fig 6.7 A and 6.7 B). Simulation visualization (Fig. 6.3 B) was made using Pymol[246] tool automol.

CHAPTER 7

COCNLUSION

This dissertation outlined my research on interaction between nanoparticles and biomolecules with the specific focus on its implications to protein structure, protein corona evolution and aggregation. It employed experimental and computational approaches to study molecular mechanisms responsible for corona formation and characteristics. Comprehension of the protein corona molecular level mechanisms would be essential for future nanomaterials application and production.

This work has addressed several topics, including Formation and Cell Translocation of Fibrinogen-Carbon Nanotube Protein Corona, followed by molecular dynamics effort to understand protein corona formation at molecular level in the following studies: Concept of Discrete Molecular Dynamic Simulations in Studying Protein Corona Formation, Effects of Nanoparticle Surface Chemistry on Nanoparticle Binding and Protein Structure, Differential Binding of Natural Amphiphiles to Nanosheets, Protein Aggregation Dependence on Nanoparticle-Protein Interaction and Relative Concentration.

Formation and Cell Translocation of Fibrinogen-Carbon Nanotube Protein Corona

In this study, I examined the formation and stability of fibrinogen-carbon nanotubes protein corona in aqueous solution and *in vivo*. Characterization of protein corona was done through UV-Vis absorbance and fluorescence spectroscopy. From TEM images we concluded that protein corona on multiwalled carbon nanotubes was more of

complex morphology, while protein corona formed on singlewalled nanotubes was smoother. Through UV-Vis absorbance at 280 nm we followed the change in the absorbance peak of fibrinogen tryptophan residues over 10 h. Absorbance peak of fibrinogen-SWCNT protein corona dropped exponentially following diffusion-sedimentation model, and eventually got stabilized after 400 min. On the contrary fibrinogen-MWCNT protein corona was stable in aqueous solution over all 10h. This suggests formation of "soft" corona in the case of SWCNT and "hard" corona in the case of MWCNT. Further fluorescence study backed this result. Quenching of Alexa Fluor 546 labeled fibrinogen fluorescence intensity upon binding to carbon nanotubes was monitored over different nanotubes concentration. The data was fitted by Stern-Volmer equation and Stern-Volmer coefficients were extracted, suggesting higher quenching power of MWCNT over SWCNT, implying that MWCNT better favored the protein binding.

Then carbon nanotubes with already formed protein corona with dye labeled fibrinogen were introduced into HT-29 cell lines extracellular environment. The fluorescence of fibrinogen was recovered upon entering of SWCNT into the cell, while MWCNT were bound to the cell membrane without penetrating it, probably due to high energy cost for their endocytosis. The recovery of fluorescence meant that protein got detached from SWCNT upon entering the cell, suggesting differential interaction between SWCNT and fibrinogen with amphiphilic membrane. All this results imply that protein corona on SWCNT was of the "soft" character, owing to high curvature of SWCNT and its small radius which were less favorable for the alignment and adsorption

of the tubular fibrinogen molecules. To better understand molecular mechanism of protein corona formation, I decided to use molecular dynamics methods in further studies.

Concept of Discrete Molecular Dynamic Simulations in Studying Protein Corona Formation

Here I examined formation of silver nanoparticle-ubiquitin corona. Ubiquitin is protein found in every eukaryotic cell. A silver nanoparticle was modeled to capture general properties of a metallic nanoparticle with predominantly hydrophobic atoms and small fraction of positively charged surface atoms. To mimic experimental conditions, negatively charged citrates were introduced onto nanoparticle surface through electrostatic interaction with positive surface atoms. Upon introduction of neutrally charged ubiquitins (pH 7.0), we observed displacement of citrate molecules from the nanoparticle surface and binding of ubiquitins. Although ubiquitin is negatively charged, it has 11 positively charged and 11 negatively charged residues. Near the protein helix surface there were identified residues with low negative potential that preferred binding to countercharges on NP surface. To evaluate if NP-ubiquitin interaction was electrostatically driven, we assigned higher electrostatic interaction between citrates and NP charged surface atoms. In this case citrate got more stabilized on the surface and resisted replacement by the protein molecules, leading to no ubiquitin bound to the surface. Consequently, we identified that electrostatic force was driving the formation of

the protein corona. After analysis of residue binding affinities, we found that residues 2 and 18 have high binding propensity. In the NMR experimental study with gold nanoparticles and ubiquitin similar result was obtained and residues 2, 15 and 18 were found to bind the surface. The reason residue 15 didn't have high number of contacts with the NP surface in our simulation was due it burial in the protein structure. This agreement between experimental result and the simulation highlighted the predictive power of our computational approach.

Further, protein corona kinetics was studied. Through the PMF construction based on center of the mass distances between nanoparticle and protein, and number of contacts between nanoparticle and identified residues that specifically bind to its surface, two peaks in PMF were identified. One corresponding to nonspecific binding and the other to specific binding. The barrier dividing these two peak corresponds to reorientation of the protein, suggesting that protein reorientation was the rate limiting step towards specific binding. Further formation of corona through coarse grained protein model was examined with interaction based on atomistic DMD simulations. Competition between citrates and ubiquitins was observed, and formation of the first layer protein corona followed by the formation of the second layer. This was characterized by the number of unbound proteins over time, which was fitted to the stretched exponential function. The stretched exponential fit suggests heterogeneity in relaxation time which comes from replacement of citrates from the surface to form the first layer, and then slowing down of the binding rate when the formation of the second layer takes place. This implies the non-cooperative character of protein-protein interaction.

Also both experimentally and computationally, destabilization of helical structure and increase in beta sheets was observed, further confirming the predictive power of our computational method in capturing protein corona effects.

Effects of Nanoparticle Surface Chemistry on Nanoparticle Binding and Protein Structure

Surface functionalization of nanomaterials is commonly used method in order to broaden their biomedical application through enhanced solubility. In this study, I examined the effect of fullerene hydroxylation to ubiquitin structure. Different number of hydroxyl groups was randomly assigned to fullerene surface (0, 4, 8, 12, 16 and 20). According to binding preference these 6 different fullerene derivatives could be divided in two groups: hydrophobic corresponding to 0, 4 and 8 OH groups and hydrophilic with 12, 16 and 20 OH groups. Fullerenols with 20 OH groups were observed to have two preferential binding site, with the one being near tyrosine, which was experimentally observed to have its fluorescence quenched with addition of fullerenols. This again affirms prediction of our computational method. Further, we observed that pristine fullerenes lead to protein denaturation once they got into hydrophobic core of the protein, while fullerenols (20 OH) stabilized protein structure.

As fullerenes are considered in potential use for drug delivery, it is important to investigate how its functionalization can adversely affect the biological system once they get introduced to it. This study suggest that hydrophobicity of the fullerenes may have

121

toxic effect once introduced to biological mille and that it is important factor to consider in order to use these nanomaterials in medicine.

Differential Binding of Natural Amphiphiles to Nanosheets

Previous studies addressed genesis of the protein corona and its dynamics in the case of one biomolecule type involved. It is more realistic that once a nanoparticle gets into the biosystem it will interact with different types of molecules. Thus, I conducted study focused on binding affinities and protein corona evolution of natural amphiphiles likes sugars, small peptides and fatty acids to graphene and graphene oxide nanosheets. Here, we observed that graphene has higher affinity to bind these molecules owing to its more hydrophobic surface compared to more hydrophilic graphene oxide. On the other hand, fatty acids showed the highest affinity towards nanosheets due to their greater flexibility and carbon content compared to the sugar and the peptide. This differential binding affinity reflected on protein corona evolution.

In early times it was observed that the most abundant species-peptides and sugars were first to bind, but at longer times they got replaced by fatty acid that possessed highest affinity to bind the nanosheets. Consequently, we suggest that highly concentrated species with low surface affinity can initiate formation of the "soft" corona, but eventually high affinity specie will replace them and render "hard" corona on the nanoparticle surface. This study offers insights in the mechanistic understanding of the fate and implication of graphene derivatives in biological and ecological environments.

122

Protein Aggregation Dependence on Nanoparticle-Protein Interaction and Relative Concentration

It was found that nanoparticles can enhance of hinder the protein aggregation depending on the nanoparticle type and relative concentration ratios between NPs and amyloids. In order to identify undelaying parameters that control nanoparticle propensity towards protein aggregation, I performed DMD study on the coarse grained amyloid beta and metallic nanoparticle. This study, specifically addressed the aggregation dependence on the intensity of attractive interaction between NP and the protein and as well on their relative concentration.

The result suggest that in the case of weakly interacting NP-protein systems, propensity on the aggregation depends on the relative ratio between NP and protein. If protein:NP concentration ratio is high, weak interaction between NP and protein will effectively increase protein concentration around NP surface, promoting the protein aggregation. On the other hand, at low protein:NP concentration ratios, weak interacting NPs will drastically reduce the protein from the bulk, but due to high NP concentration, each NP will have as well low number of proteins around its surface, effectively hindering the aggregation. By increasing the interaction strength we saw increase in aggregation propensity on the nanoparticle surface up to the critical point after which interaction was too strong and consequently reduced diffusion rate. Reduced protein diffusion on the strongly interacting nanoparticle surface hindered protein aggregation independent of the relative concentration ratios between NP and the protein. In summary,

this study identified parameters that should be considered in order to predict aggregation effects of the specific nanoparticle onto amyloidogenic proteins.

Future Directions

Future work related to this dissertation would concentrate on the study of protein crowding effect onto protein structure upon binding to the nanoparticle surface, as for example interior of the cell is highly crowded environment. Generally, it is adopted that crowding effect should have stabilizing effect onto protein due to reduced conformational entropy, but there are studies suggesting opposite. This is probably consequence of protein-protein interactions. It would be of great interest how crowding stabilizing effect competes with nanomaterials destabilizing effect onto the protein structure.

Also, when we studied protein aggregation in the presence of the nanoparticle we assigned non-specific interactions between nanoparticle surface and the protein. The next study should delineate how specific interaction influences protein aggregation, in the case when protein preferential orientation can induce differences in lag time and elongation rates.

Both these studies would give us better mechanical understanding of protein corona implications in biological environments and establishing pathway in responsible and effective application of nanomaterials.

APPENDICES

APPENDIX A

1. Methods

Experimental characterisation of AgNP-ubiquitin corona.

Transmission electron microscopy imaging of AgNP-ubiquitin corona. Direct observation of formed AgNP-ubiquitin coronae was performed by transmission electron microscopy (Hitachi H7600). Specifically, AgNPs (10 nM) were incubated at room temperature in deionized water (18 MΩ-cm) at neutral pH with ubiquitin (5 µM) for 2 h, pipetted on a copper grid and negatively stained with phosphotungstic acid (optically less dense material) for 10 min prior to imaging. Similar procedures were performed for the protein-free control AgNPs (10 nM).

Hydrodynamic size and zeta potential measurements. Citrate-coated AgNPs (BioPure, nominal size: 10 nm) were purchased from NanoComposix and dispersed in Milli-Q water to form a stock suspension of 1 mg/mL (300 nM). Lyophilized ubiquitin (Boston Biochem, isolated from plant *Arabidopsis thaliana*) of 5 mg was dissolved in 500 mL Milli-Q water to obtain a final concentration of 1 mM. The hydrodynamic sizes of AgNPs (34.9 nM), ubiquitin (10 mM), and AgNP-ubiquitin (molar ratio: 1:100; incubation: 2 h) were measured with three repeats each at room temperature using a Zetasizer (Nano-S90, Malvern) (**Appendix A Fig. A1)**. In addition, the zeta potentials of AgNPs (4.97 nM), ubiquitin (5 mM), and AgNP-ubiquitin (molar ratio: 1:1000; incubation: 2h) were obtained at pH 6.5 using a Zetasizer (Nano, Malvern).

UV-vis absorbance measurement. To infer the binding of ubiquitins onto AgNPs we carried out an absorbance measurement using a UV-vis spectrophotometer (Cary 300

BIO, Varian). For this measurement the final AgNP concentration was 1.74 nM, while the final ubiquitin concentration was 50 mM. The mixture of AgNP-ubiquitin was incubated for 2 h prior to the measurement. An absorbance peak induced by the surface plasmon resonance of AgNPs upon excitation was observed at 393 nm, which was redshifted to 407 nm for the absorbance peak of the AgNP-ubiquitin mixture.

Circular dichroism spectroscopy. To determine changes in the secondary structures of ubiquitin upon nanoparticle-protein corona formation we performed a CD measurement using a JASCO J-810 spectropolarimeter. AgNPs and ubiquitins of a molar ratio of 1:1000 were incubated for 2 h and were diluted in quartz cuvettes to match the sensitivity of the instrument. CD spectra were acquired at room temperature over a wavelength range of 200-300 nm and averaged over five scans taken at a speed of 50 nm/min. The backgrounds of the AgNP and ubiquitin controls were subtracted accordingly. The averages derived from the CONTINLL-4 and CONTINLL-7 methods were used to calculate percents of the secondary structures of the protein, based on the linear dependence between structural fractions and the spectra[314].

Computational modeling of AgNP-ubiquitin corona.

We combined both atomistic and coarse-grained molecular dynamics simulation to characterize the structure and dynamics of protein corona, where atomistic simulations were used to identify the binding modes between an individual ubiquitin and an AgNP, and coarse-grained simulations were used to characterise the corona formation between multiple ubiquitins and an AgNP.

Discrete molecular dynamics simulation. Detailed descriptions for DMD algorithm can be found elsewhere[264,311]. Briefly, inter-atomic interactions in DMD were modeled by square-well potential functions. Neighboring interactions (such as bonds, bond angles, and dihedrals) were modeled by infinitely deep square-well potentials. During a simulation, an atom's velocity remained constant until a potential step was encountered, upon which time it changed instantaneously according to the conservations of energy, momentum, and angular momentum. Simulations proceeded as a series of such collisions, with a rapid sorting algorithm used at each step to determine the subsequent collision.

The difference between DMD and traditional molecular dynamics is in the form of the interaction potential functions. Approximating continuous potentials with step functions, DMD simulations were reduced to event (collision)-driven molecular dynamics. The improved sampling efficiency of DMD over traditional molecular dynamics originates mainly from the rapid processing of collision events and localized updates of collisions (only collided atoms are required to update at each collision). At an adequately small step size, the discrete step function approaches the continuous potential function and DMD simulations become equivalent to traditional molecular dynamics. DMD simulations have been widely used to study biomolecules[312], such as protein folding[265], molecular recognitions[315], and protein aggregation[180].

Atomistic DMD model. We used the united-atom representation for proteins and citric acids (citrates), where all heavy atoms and polar hydrogens were explicitly modeled. The bonded interactions included covalent bonds, bond angles, and dihedrals.

We included van der Waals, solvation, environment-dependent hydrogen bonding interactions, and electrostatics in the non-bonded interactions. The solvation energy was modeled using the Lazaridis-Karplus implicit solvation model with the fully-solvated conformation as the reference stated[183]. The hydrogen bond interaction was modeled using a reaction-like algorithm[316]. In addition to the previous version of the atomistic DMD force field[265], we also added electrostatic interactions between charges, including the basic and acidic residues in proteins[180] and charged groups in small molecules. The interaction parameters for citric acids were adapted from the Medusa force field extension for small molecules[281]. We used the Debye-Hückel approximation to model the screened charge-charge interactions. The Debye length was set at approximately 10 Å by assuming water relative permittivity of 80, and a monovalent electrolyte concentration of 0.1 mM. We used an interaction range of 30 Å for the electrostatic interactions, where the screened potential approached zero.

AgNP model. Because our knowledge of the interactions between nanoparticles and proteins is still lacking, there are no well-accepted force fields that can readily capture the binding between AgNP and proteins. In order to model the formation of AgNP-ubiquitin corona, we developed a simple model for simulating AgNP. Since the interactions between AgNP and proteins take place primarily on the surface of AgNP, we only explicitly modeled the surface atoms. The VDW radius of a silver atom is $r = 1.72$ Å. Assuming close packing of silver atoms on the surface, we can calculate that the number of surface atoms for an AgNP with the diameter $D = 100$ Å is $N = \pi D^2 \rho_{2d} / \pi r^2$, where ρ_{2d} is the close packing density of ~0.84. Therefore, the total number of silver atoms is ~2,830

in one AgNP. We grouped every three atoms into one coarse-grained silver atom with a VDW radius of ~2.98 Å, and the number of surface atoms was reduced to 943. We introduced one atom in the center of the AgNP, and imposed distance constraints between the center and surface atoms at [49.5 Å, 50.5 Å]. As a result, all surface atoms effectively remained on the AgNP surface during simulations.

The same coarse-grained AgNP model was used in both all-atom and coarse-grained DMD simulations. In the all-atom simulations, the non-bonded interactions for AgNP surface atoms included van der Waals, solvation, and electrostatics. The VDW interaction between two atoms (i and j) in Medusa is proportional to $(\varepsilon_i \varepsilon_j)^{0.5}$, where $\varepsilon_i^{0.5}$ is the dipole polarisability of atom i. We assigned $\varepsilon=0.4$ for the coarse-grained surface atoms (comparing to $\varepsilon=0.12$ for carbonyl carbon in CHARMM 19[317]). For the Lazaridis-Karplus solvation interaction[183], we assumed a coarse-grained surface atom is hydrophobic and the free energy ΔG for excluding it from water is -2 kcal/mol.

AgNP is usually synthesized by chemical reduction of Ag+ salt and capped by the negatively charged citric acid, or citrate[318]. Due to incomplete reduction, it is likely that there are residual silver ions on the AgNP surface that bind to citrates. The citrate-capped AgNP alone had the zeta-potential of -45.0 mV, suggesting excessive citrate molecules. We randomly selected a subset of the surface atoms and assigned positive charges. We initially assigned +e to the charged surface atoms and performed equilibration simulations with excessive citrates. We found that citrate molecules with -3e had the tendency to attract multiple charged surface atoms (~3) to its vicinity, forming charged clusters (**Appendix A Fig. A4**). Since the charge-charge interactions are long-ranged and

their calculations in DMD are proportional to the square of total number of charged atoms, we decided to assign a positive charge of +3e to the charged surface atoms in order to increase DMD sampling efficiency by reducing excessive calculations.

In the all-atom DMD simulations, the units of mass, length, and energy are Dalton (1.66×10^{-24} gram), angstrom (10^{-10} meter), and kcal/mol (6.9×10^{-22} joule), respectively. Given the units of mass [M], length [L], and energy [E], the time unit (t.u.) can be determined as approximately 50 femtoseconds.

Calculation of contacts between AgNP and ubiquitin. We defined a contact occurred between an ubiquitin residue and the AgNP when the distance between the AgNP center and the corresponding C_β atom of the residue was less than 57.5 Å. The protein was assumed to be AgNP-bound if at least one residue was in contact with the AgNP, and the contact frequency between each residue and the AgNP was averaged over the total time that the protein remained bound to the AgNP.

Calculation of 2D-PMF. We first computed the 2D-histogram with respect to the center-of-mass distance between AgNP and ubiquitin, d_{cm}, and the number of contacts between AgNP and the subset of residues identified to bind specifically to AgNP, N_c. The inter-molecule distance d_{cm} was sampled from 60 Å to 120 Å with the bin size of 2.5 Å, while the sampling of N_c was from 0 to 13 with the bin size of 1. The 2D-PMF was simply computed proportional to the logarithm of population, $-K_b T ln(P)$. Here, K_b is the Boltzmann constant and P is the population.

Coarse-grained molecular system. We used a two-bead-per-residue protein model for the study of corona formation between multiple ubiquitins and an AgNP[188,189]. In the

two-bead model, each amino acid was represented by only the α-carbon (backbone) and β-carbon (sidechain). The bonded interactions between neighboring atoms along the peptide chain were assigned to mimic peptide geometry[188]. We used a structure-based potential to model the sidechain-sidechain packing interactions, where native interactions observed in the native state were favored. Two interacting residues can form either intra- or inter-monomer contacts, in order to promote protein-protein association[189,190]. The attractions between the residue β-carbons were assigned with a hard-core distance of D_{hc}=3 Å and an interaction range of D_{IR}=7.5 Å. The interaction strength of the native contact was ε, which was set as 1 kcal/mol. We also modeled the backbone-backbone hydrogen bond interaction as in Ref.[189] where each Cα can maximally form two hydrogen bonds with other Cα atoms, and two hydrogen bonds formed by one Cα atom are aligned co-linear[189] in order to model the angular dependence of hydrogen bonds. Other inter-atomic interaction for proteins was simply hard sphere collisions with the hardcore distant of D_{hc}=3 Å.

We determined the folding thermodynamics of an isolated coarse-grained ubiquitin by replica exchange DMD simulations[180]. Using weighted histogram analysis method[268,283], we calculated the specific heat and RMSD of ubiquitin as the function of simulation temperature (**Appendix A Fig. A2**). The specific heat featured a single peak at T_f = 340K, which corresponded to the melting temperature of the protein. Below T_f the protein remained folded with low RMSD, which was comparable to all-atom simulations (Fig. 3b). Above T_f, the protein became unfolded with large RMSD.

Each citric acid was represented by one coarse-grained atom. We used the same AgNP model as described above and assigned a strong attraction between citrates and the charged AgNP surface atoms. The citrates showed a weak repulsion to ubiquitin to mimic the mutually exclusive binding to AgNP as observed in atomistic simulations. We assigned a more favorable attraction between the charged AgNP atoms and the AgNP-binding residues (residues 18, 19, 20, 21, 22, 24, 25, 28, 52, 54, 55, 57, and 58), compared to the rest of the protein. The interaction parameters are summarized in the **Appendix A Table A1**.

Simulation setups and conditions. i) *Atomistic simulations*. The molecular system was composed of one AgNP, one ubiquitin, and 50 citrates. The molecules were placed in a 150 x 150 x 150 $Å^3$ cubic box with periodic boundary conditions. We set a subset of 40 surface atoms of AgNP (randomly distributed) as positively charged (3e), and kept the center atom fixed during the simulations. The simulation temperature was maintained at 300 K using an Andersen thermostat[319]. The molecular system of the AgNP and citrates was equilibrated at first in order to let citrates bind to the surface charges (**Appendix A Fig. A5**). In the control simulations of artificially enhanced electrostatic interactions between citrates and the AgNP, we added an additional charge (-e) to the C6 atom of the citrate molecule (**Appendix A Fig. A6**)

ii) *Coarse-grained simulations.* There were one AgNP, 25 (or 50) ubiquitins, and 80 citrates in a 300 x 300 x 300 $Å^3$ cubic box with periodic boundary conditions. A subset of 60 AgNP surface atoms was positively charged, and the AgNP center was also kept static. We performed the simulations at a constant temperature of 325 K, which was

set to enhance the kinetics while still below the melting point (**Appendix A Fig. A2**).

Fitting analysis of the AgNP-ubiquitin binding kinetics. We used the least square (χ^2) approach to fit the ubiquitin-AgNP binding data derived from coarse-grained DMD simulations. Since the data was approximately linear in the log-log plot (**Fig. 1.4 & Appendix A Fig. A7**), we fitted the data with three different models, including a power-law, $\sim t^{\alpha}$, a stretched exponential, $\sim 1\text{-}exp(\text{-}ct^{\alpha})$, and a cumulative lognormal, $\sim 1\text{+}erf(c\ln(t/\tau))$. Here, *erf* is the error function. Among three fitting models, the power-law gave the largest χ^2-value, 962.4. The fitting for both the stretched exponential and cumulative lognormal functions were similar, with χ^2-values equal to 469.1 and 486.8, respectively. A lognormal distribution is usually used to describe the data where the value is the multiplicative product of many independent random variables. The relaxation time cannot be modeled as the product of a large number of independent random variables. On the other hand, a stretched exponential function is often used to describe the relaxation kinetics with high heterogeneity in relaxation time, where the kinetics can be described as linear superposition of exponential decays with continuous distribution of relaxation time. A similar stretched exponential binding kinetics has been observed in a fluorescence study of protein binding to colloidal nanoparticles[191]. Therefore, the stretched exponential (α=0.34) better characterized the ubiquitin-AgNP binding kinetics.
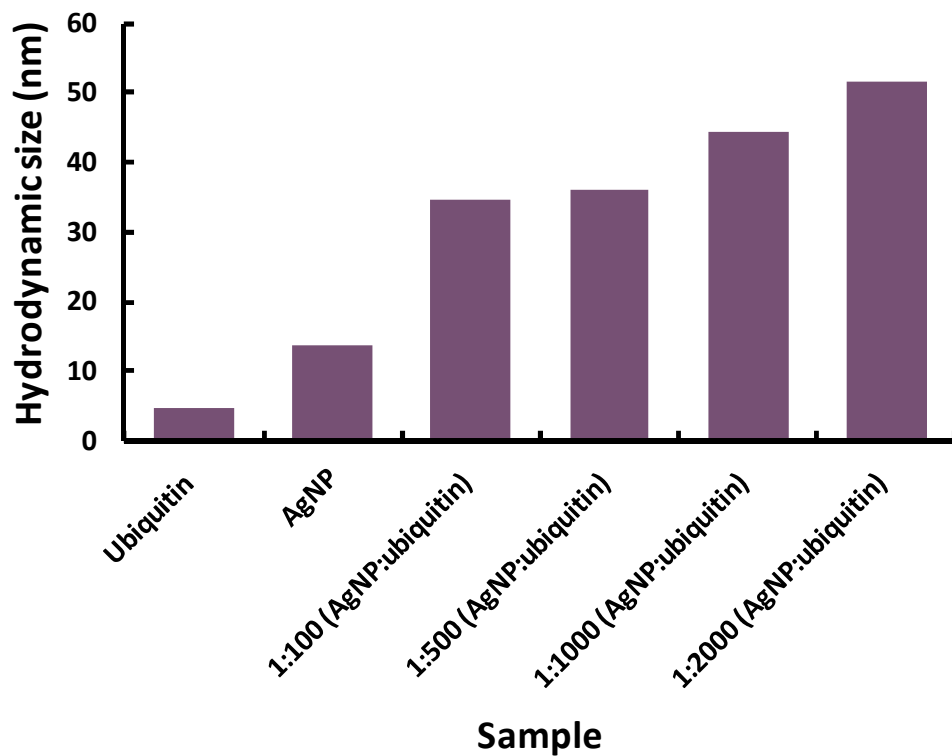
Figure A1. Hydrodynamic size of AgNP-ubiquitin corona at different molar ratios.
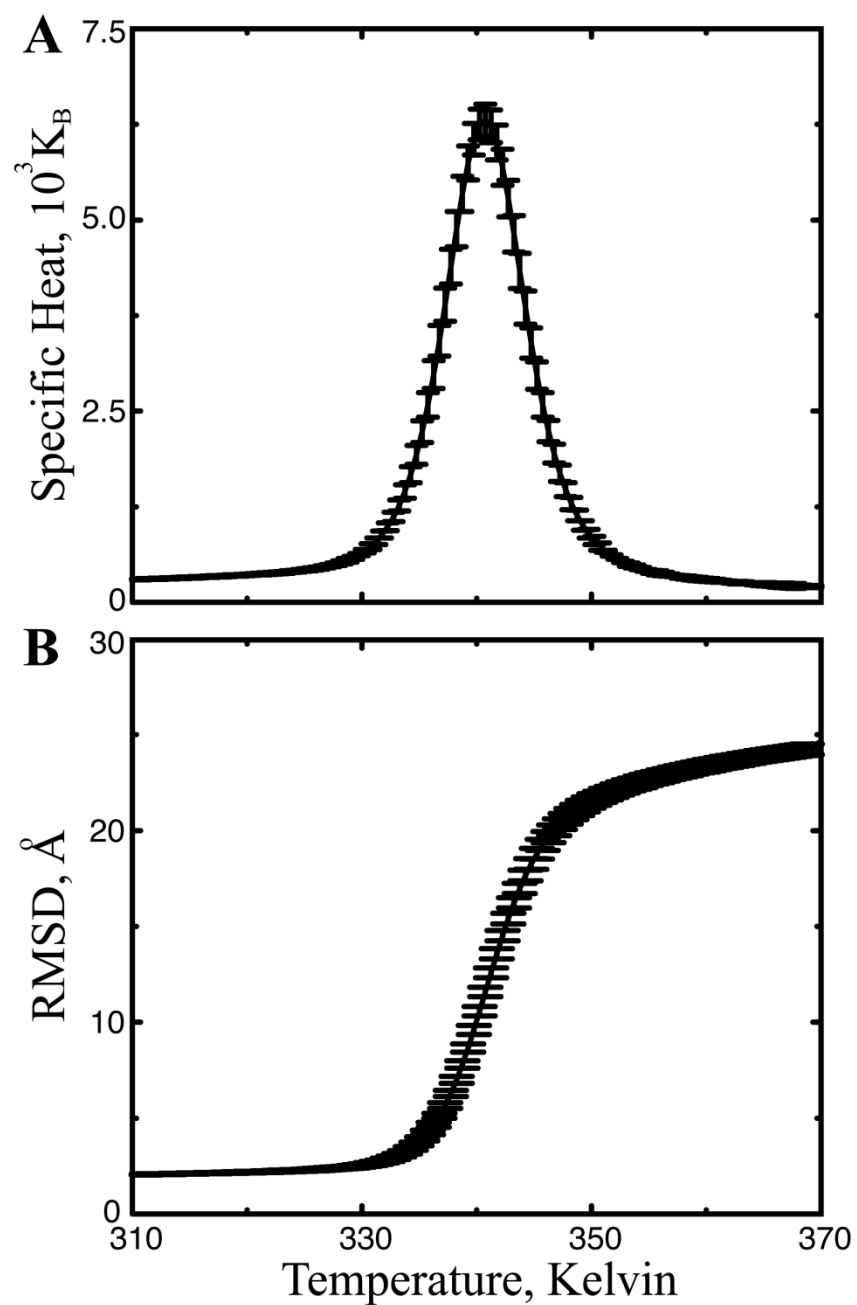
Figure A2. The folding thermodynamics of the coarse-grained ubiquitin. The specific heat (A) and RMSD (B) were computed as the function of the simulation temperature using replica exchange simulations and weighted histogram analysis. The error bars were computed as the statistical uncertainty[268].
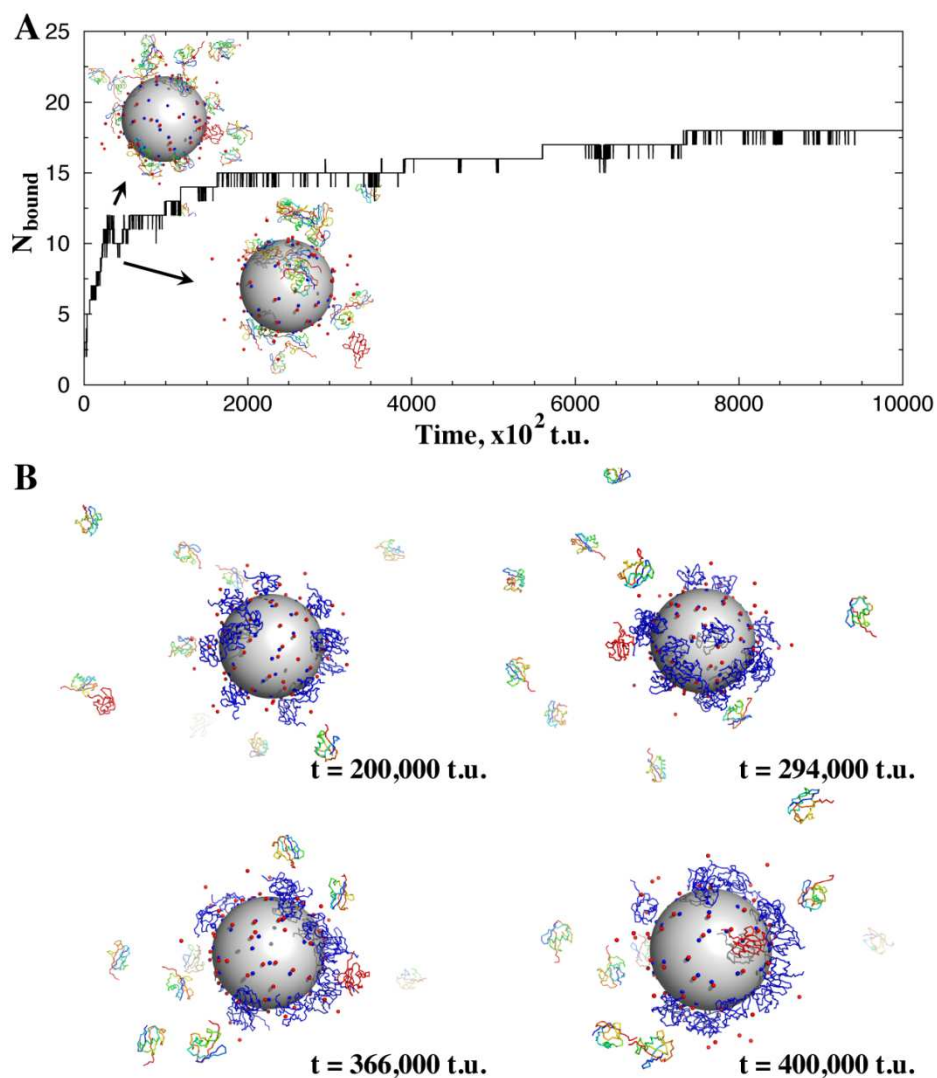
Figure A3. The kinetics of ubiquitin-AgNP binding. (a) The number of ubiquitin molecules bound to AgNP, N_{bound}, as the function of time (in DMD time unit, t.u., see Supporting Information) from a typical DMD simulation. The backbone trace of ubiquitin (rainbow color) is shown. The citrates correspond to the red spheres. The large gray sphere denotes the AgNP, and the blue spheres on the surface of the AgNP are the positively charged atoms. The insert illustrates the association and dissociation of a ubiquitin (in red). (b) The snapshots along the

DMD simulation trajectory demonstrate the non-specific binding between incoming ubiquitin and proteins already bound to AgNP, which slows down the association.
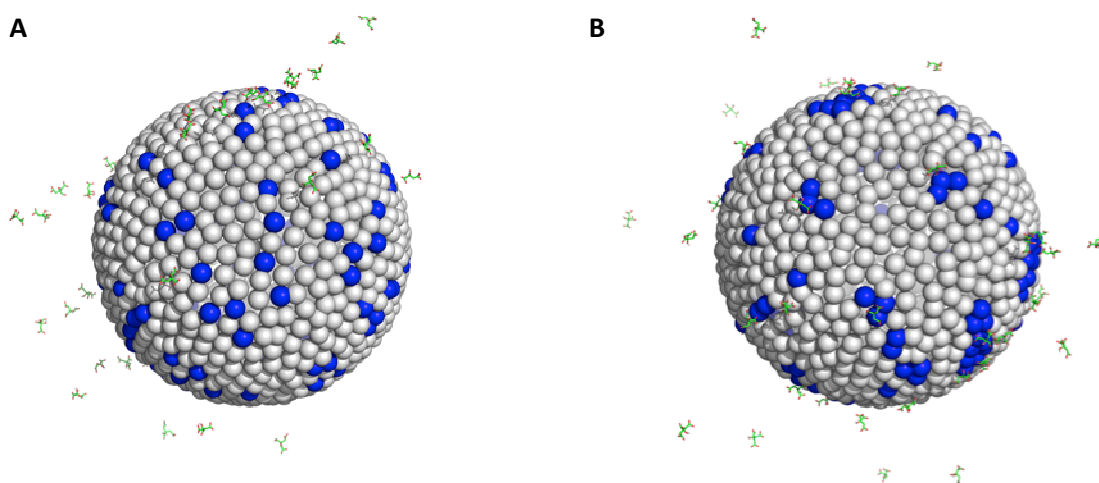
Figure A4. The equilibration of citrates and AgNP. The coarse-grained surface atoms are shown as spheres, where the charged atoms are colored blue and uncharged atoms are gray. The citrate is shown in stick representation. (A) Initially, the charges (+e) were randomly distributed on the surface and citrates were not bound. (B) During the equilibration simulations, the citrates with -3e had the tendency to attract multiple charged atoms (~3) together, forming charged clusters.
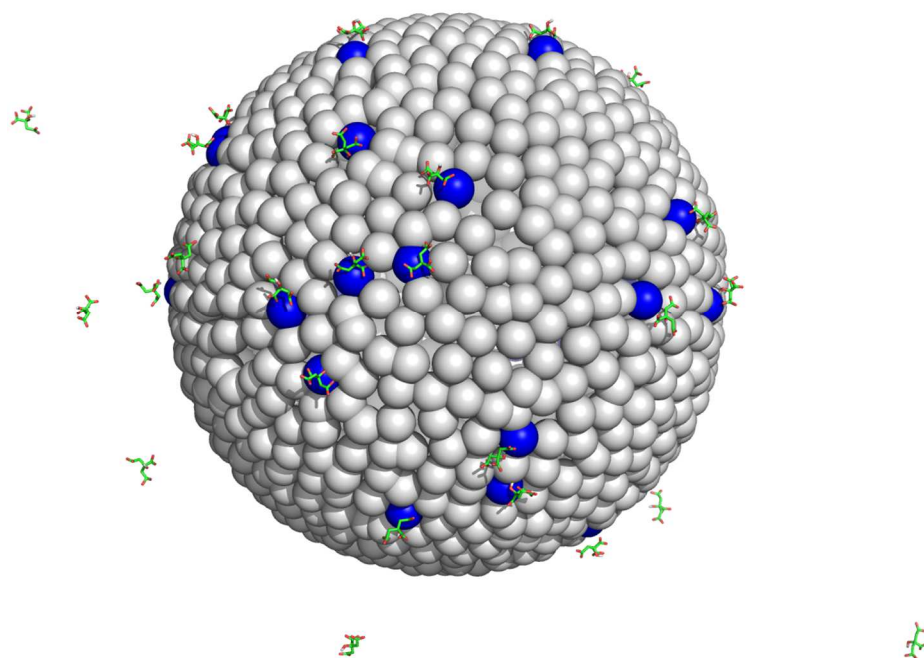
Figure A5. The equilibrated state of citrate-capped AgNP. The charged surface atoms (+3e) are shown as blue spheres, and the rest surface AgNP atoms are represented as gray spheres. The negatively-charged citrates (-3e) bind to the charged AgNP surface atoms, while there are excessive citrates in the solution.
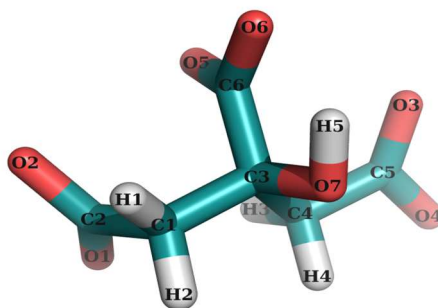
Figure A6. The molecular structure of citrate. The citrate molecule is in stick representation and the atoms are specifically labeled.
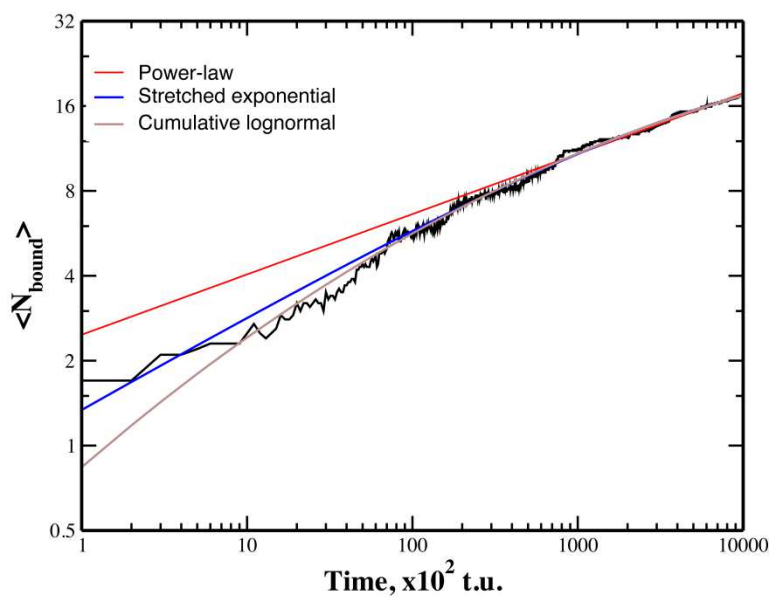
Figure A7. The ubiquitin-AgNP binding kinetics. The average number of ubiquitins bound to

AgNP, $<N_{bound}>$, was computed as the function of simulation time in a log-log plot (black line).

Using the least square method, the data was fitted with a power-law (red line), a stretched

exponential (blue), and a cumulative lognormal (brown).

Table A1. Interaction parameters between coarse-grained atoms. Most of the interactions were modeled by a single-well DMD potential, where D_{hc} denoted the hard-core distance, D_{IR} indicated the interaction range beyond which two atoms did not interact, and E_{rep} and E_{attr} corresponded to the repulsive (>0) and attractive (<0) energy steps, correspondingly. The energy unit, ε, was set as 1 kcal/mol. A hard sphere collision potential between atoms was defined by the hard-core distance, D_{hc}. The charged AgNP surface atoms interacted with each other via the screened electrostatic repulsion as described in the all-atom simulations (Methods). The AgNP-binding involved residues 18, 19, 20, 21, 22, 24, 25, 28, 52, 54, 55, 57, and 58, which featured high contact frequencies as revealed by the all-atom simulations. The interactions between inter- and intra-protein atom pairs were modeled by the structure-based potentials[189,190].

	Citrate	AgNP atom		Ubiquitin		
		Uncharged	Charged	AgNP-binding residue, C_β	Other residue, C_β	Backbone $C\alpha$
Citrate	D_{hc} = 4.5Å D_{IR} = 7.5Å E_{rep} = 2ε	D_{hc} = 4.5Å D_{IR} = 7.5Å E_{rep} = -1.2ε	D_{hc} = 4.5Å D_{IR} = 7.5Å E_{attr} = -4.2ε	D_{hc} = 4.5Å D_{IR} = 7.5Å E_{rep} = 0.4ε		Hard sphere: D_{hc} = 4.5 Å
Uncharged AgNP atoms	D_{hc} = 4.5 Å D_{IR} = 7.5Å E_{rep} = -1.2ε	Hard sphere: D_{hc} = 5.95 Å	Hard sphere: D_{hc} = 5.95 Å	D_{hc} = 4.5 Å D_{IR} = 7.5Å E_{attr} = -0.4ε		
Charged AgNP atoms	D_{hc} = 4.5 Å D_{IR} = 7.5Å E_{attr} = -4.2ε	Hard sphere: D_{hc} = 5.95 Å	Electrostatic repulsion	D_{hc} = 4.5 Å D_{IR} = 7.5Å E_{attr} = -1.0ε	D_{hc} = 4.5 Å D_{IR} = 7.5Å E_{attr} = -0.4ε	
AgNP-binding residue, C_β	D_{hc} = 4.5 Å D_{IR} = 7.5Å E_{rep} = 0.4ε	D_{hc} = 4.5 Å D_{IR} = 7.5Å E_{attr} = -0.4ε	D_{hc} = 4.5 Å D_{IR} = 7.5Å E_{attr} = -1.0ε	Structure-based interaction potential (Methods)		
Other residue, C_β			D_{hc} = 4.5 Å D_{IR} = 7.5Å E_{attr} = -0.4ε			
Backbone $C\alpha$	Hard sphere: D_{hc} = 4.5 Å					
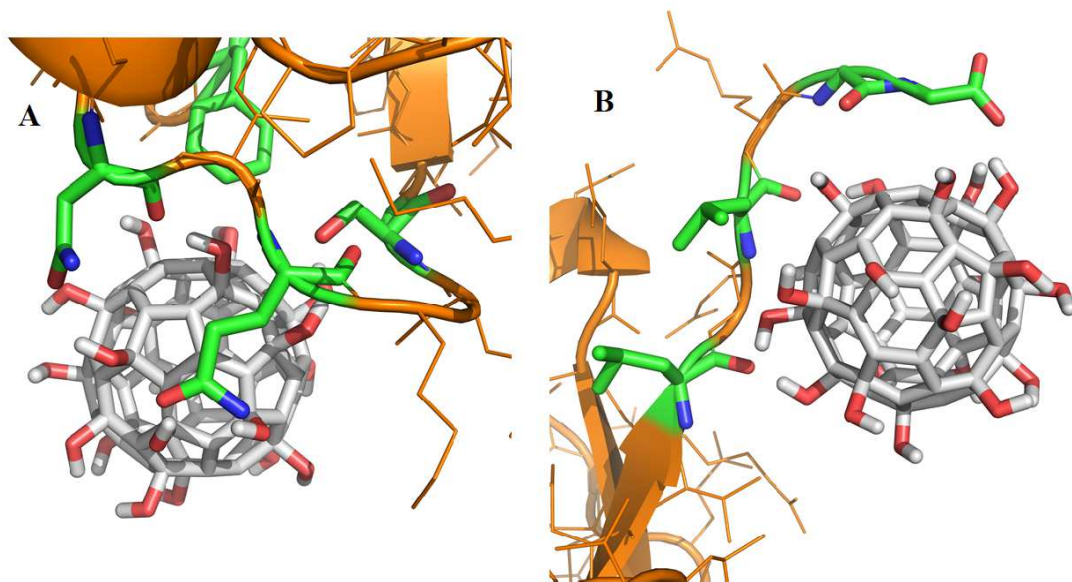
Figure B1. The binding sites of C60(OH)20 fullerenol on ubiquitin as predicted by docking simulations. The residues that make direct contact with ubiquitin include Phe45, Asn60, Gln 62 and Ser65 at site 1 (A), and Leu71, Leu73, Gly75 and Gly76 at site 2 (B), which are highlighted by depicting in stick representation. The C60 fullerene bind predominantly to site 1.
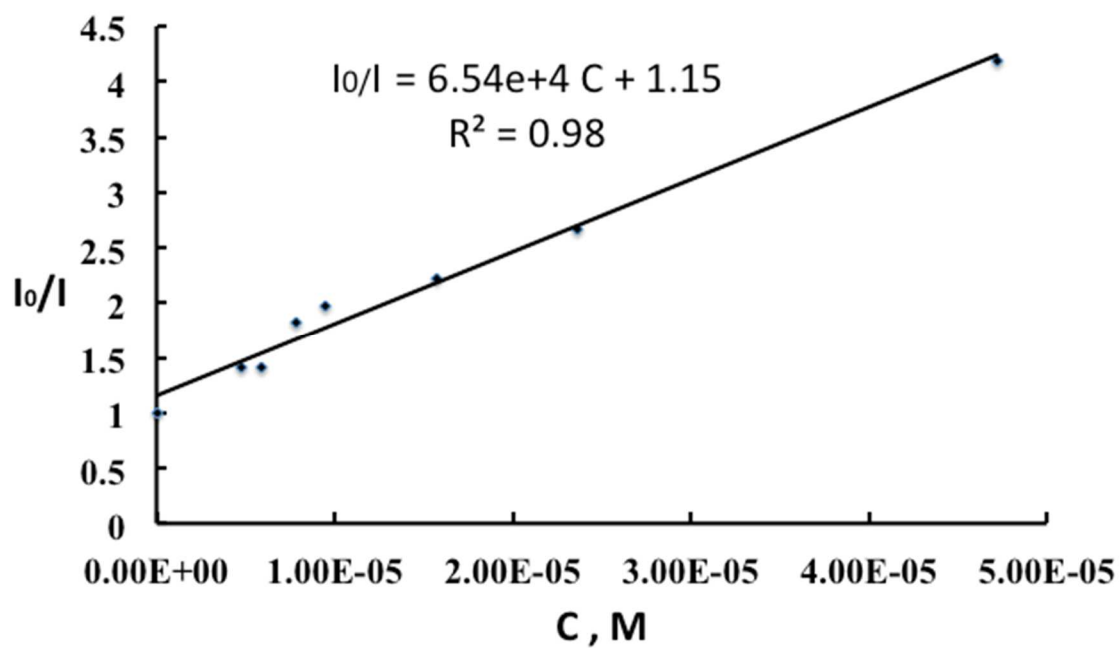
Figure B2. Stern-Volmer plot of fluorescence quenching of ubiquitin in the presence of fullerenol C_{60} $(OH)_{20}$.
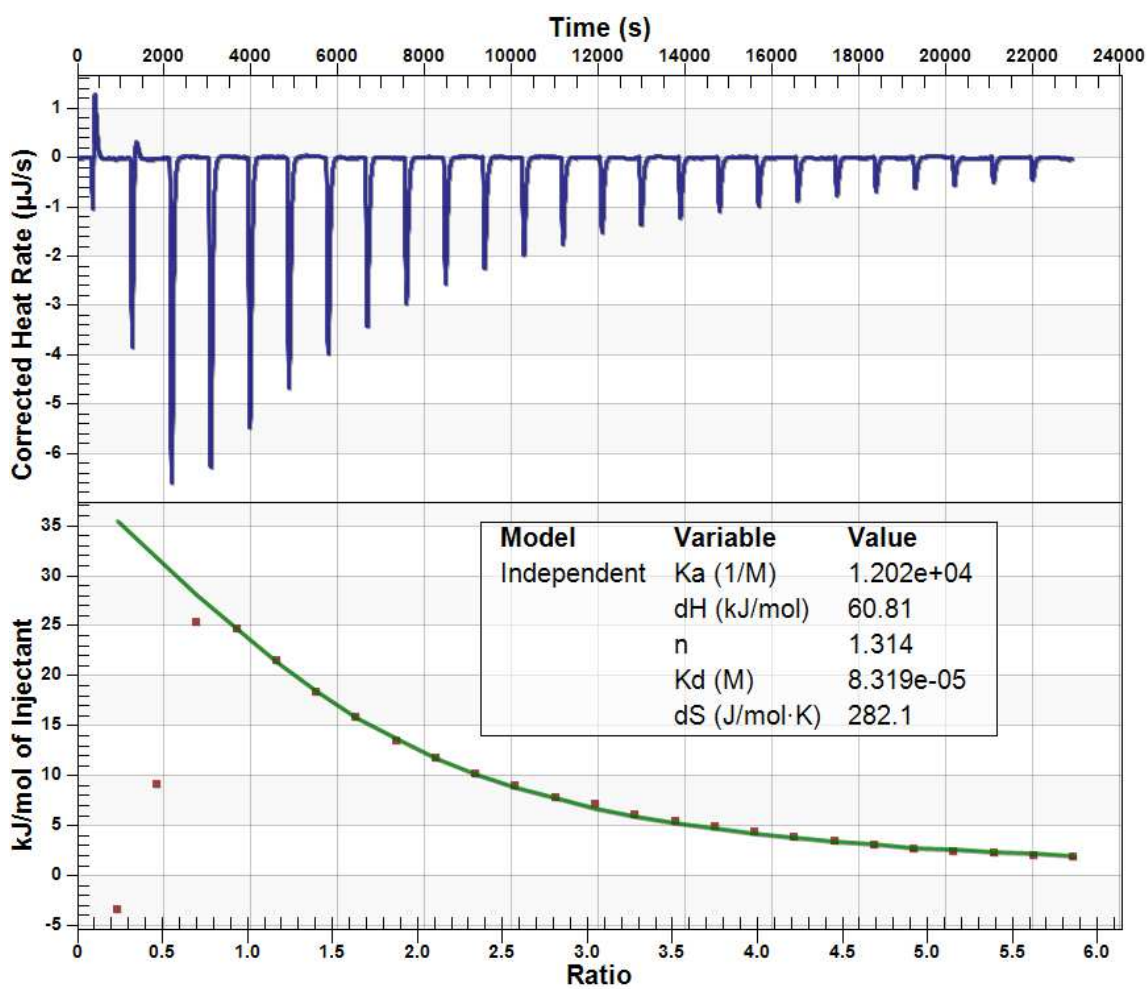
Figure B3. Isothermal titration calorimetry of C$_{60}$(OH)$_{20}$ fullerenol into ubiquitin
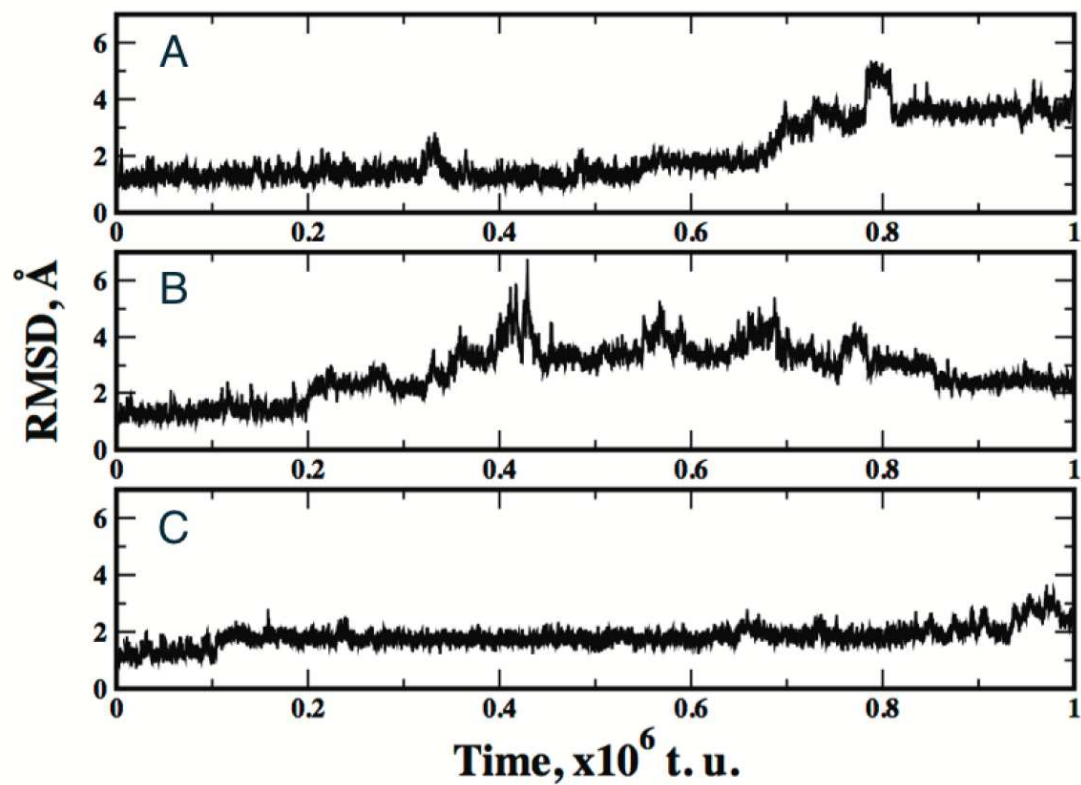
Figure B4. Representative RMSD plots of ubiquitin without any nanoparticles from DMD simulations. The three trajectories (A-C) are taken from three independent simulations.
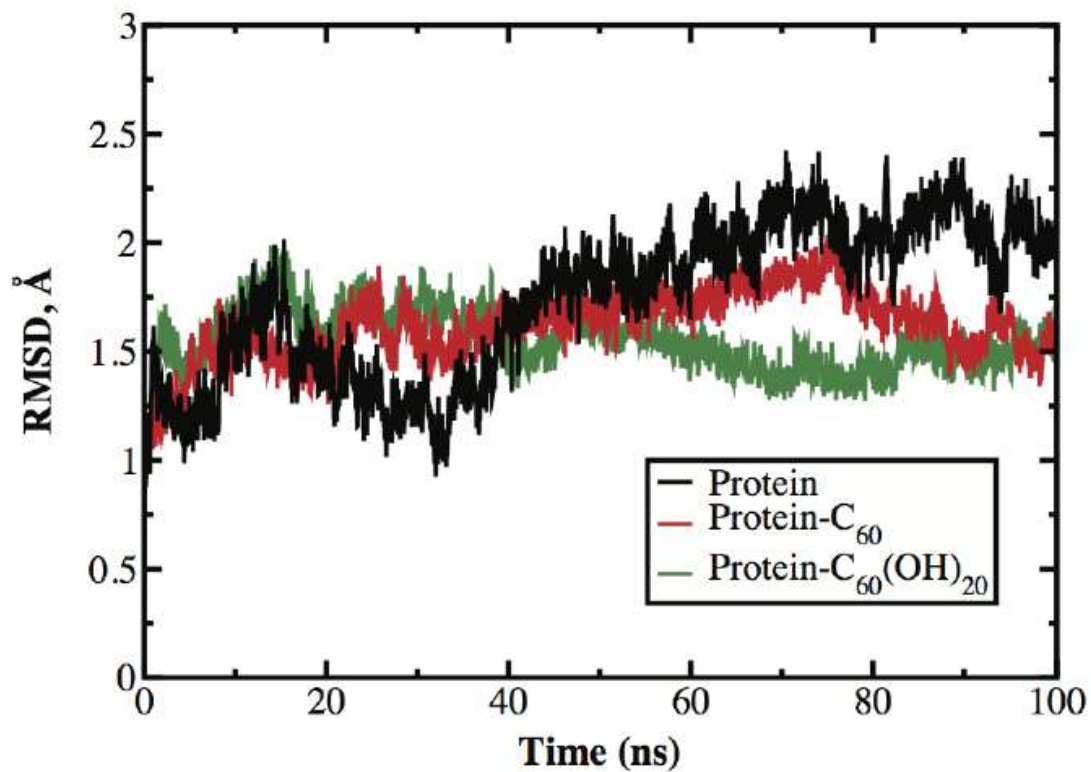
Figure B5. Protein heavy atom RMSD fluctuations in MD simulations in the cases of

ubiquitin-alone (black), ubiquitin with C60 fullerene (red) and ubiquitin with C60(OH)20

fullerenol (green).
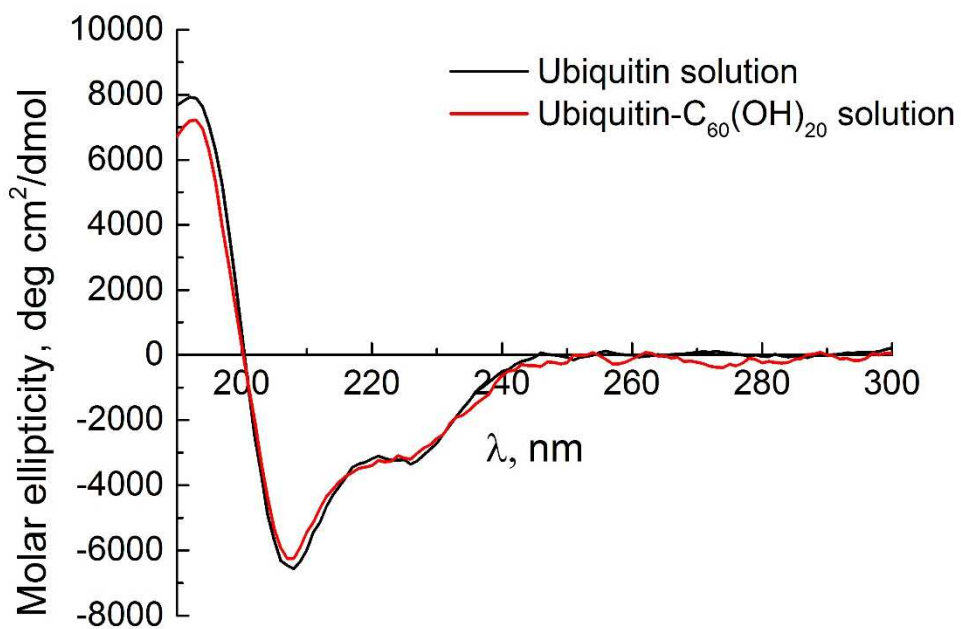
Figure B6. Circular dichroism spectra of ubiquitin and ubiquitin-fullerenol solutions
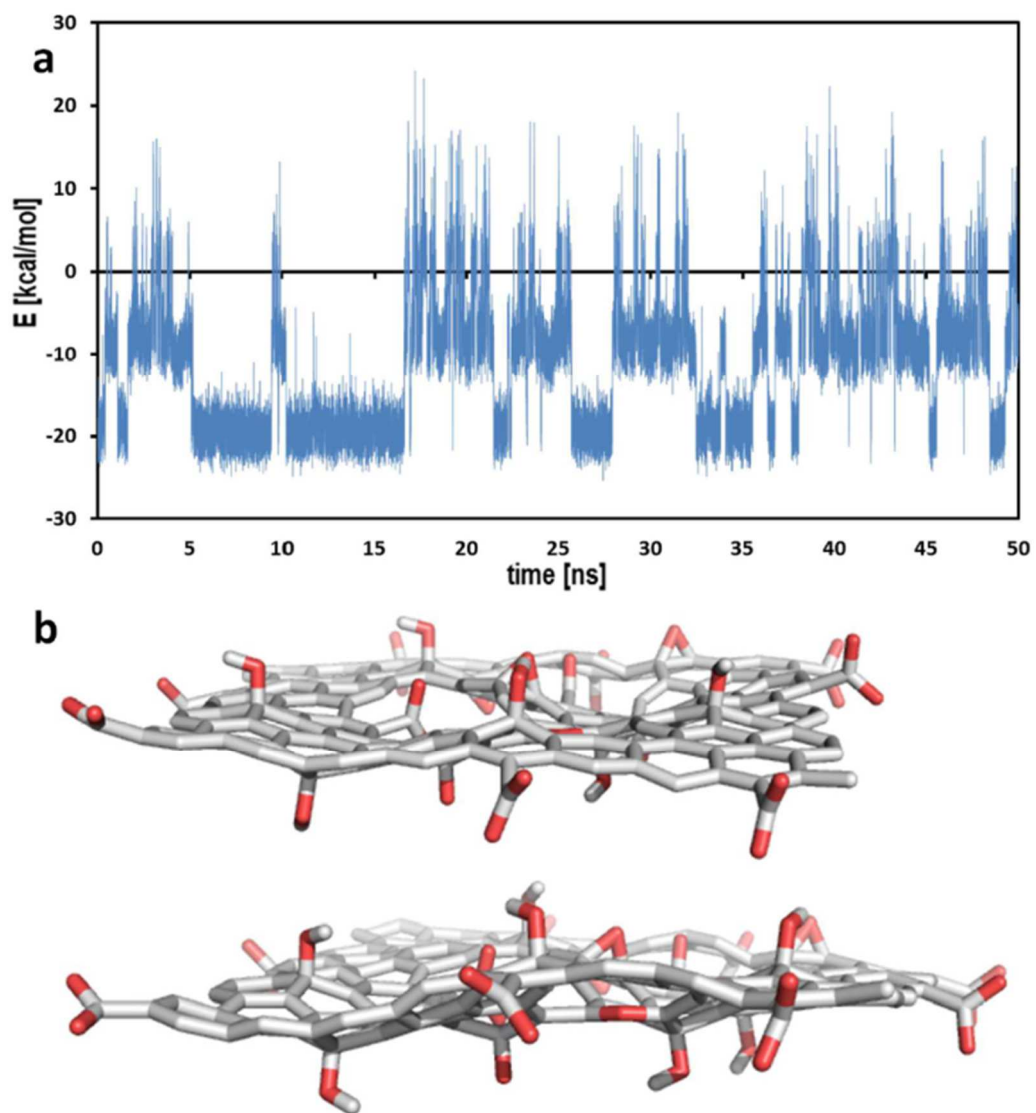
Figure C1. The high-energy normal mode of the graphene oxide nanosheet. The simulations were done with the nanosheet alone. (a) At T~0.67 kcal/mol·k_B, the fluctuation of the potential

energy indicated excitation of a higher-energy normal mode. (b) The snapshots of the nanosheet

in the high-energy state illustrated the twisted normal mode.
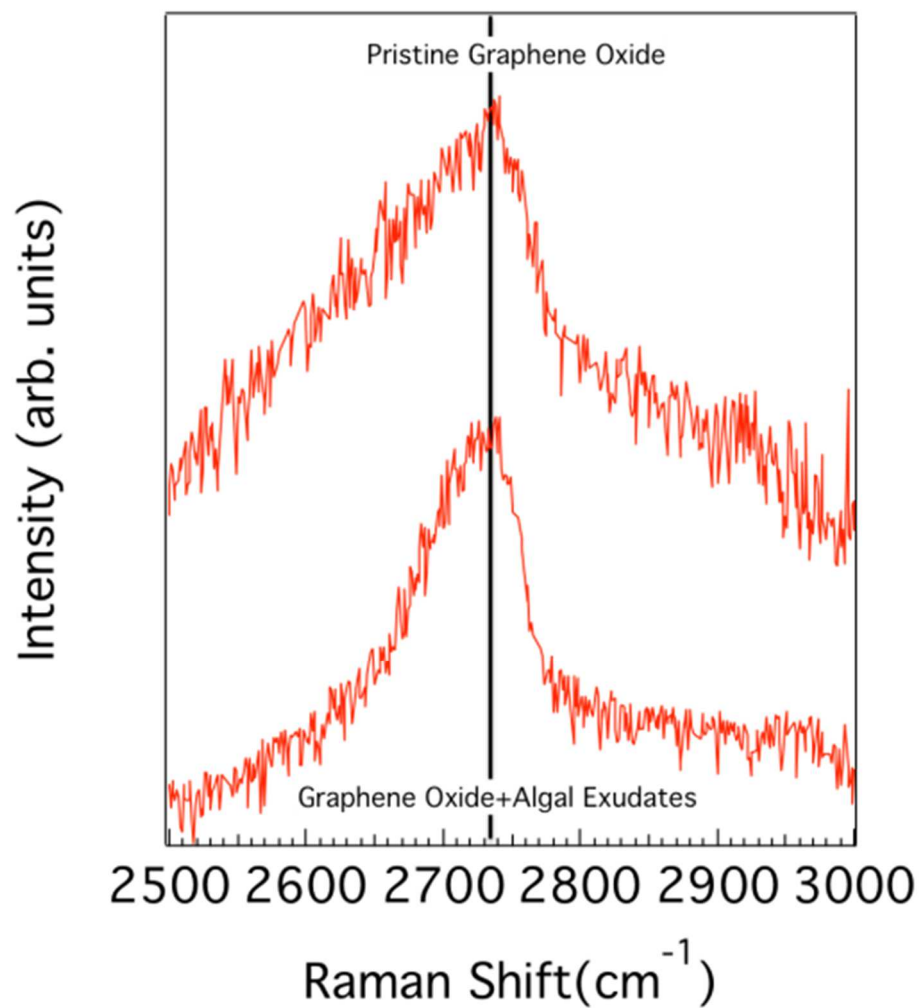
Figure C2. Raman spectra of graphene oxide before and after incubation with algal exudates. The absence of any shift in the 2D-band ($\sim$2730 cm^{-1}) suggests that the interaction between graphene oxide and exudates was weaker compared to graphene and exudates.
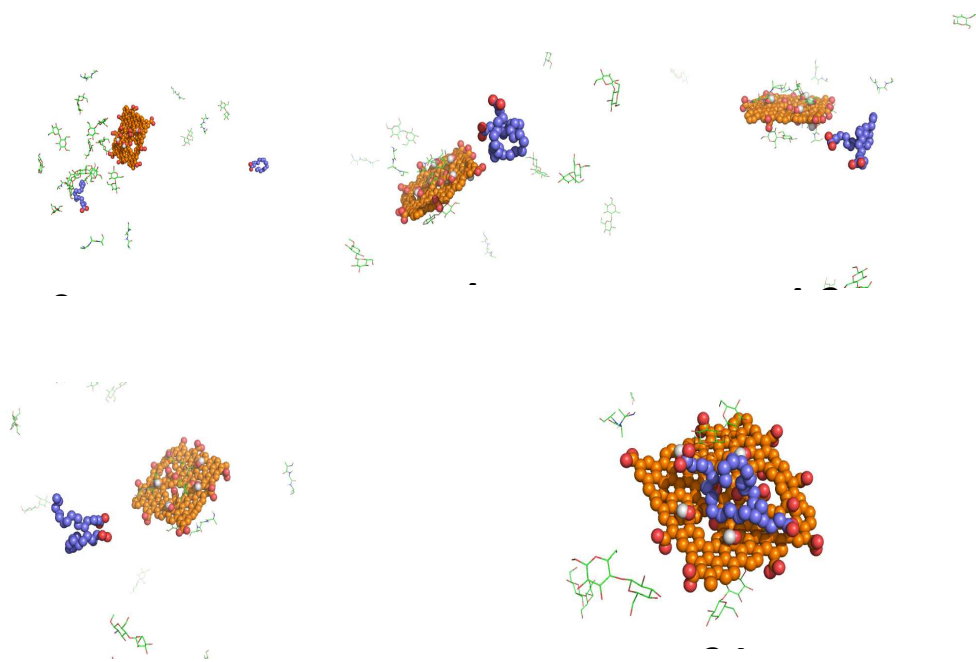
Figure C3. Palmitic acids (purple) were observed to bind to each other before their adsorption onto the nanosheet in one of the simulations.
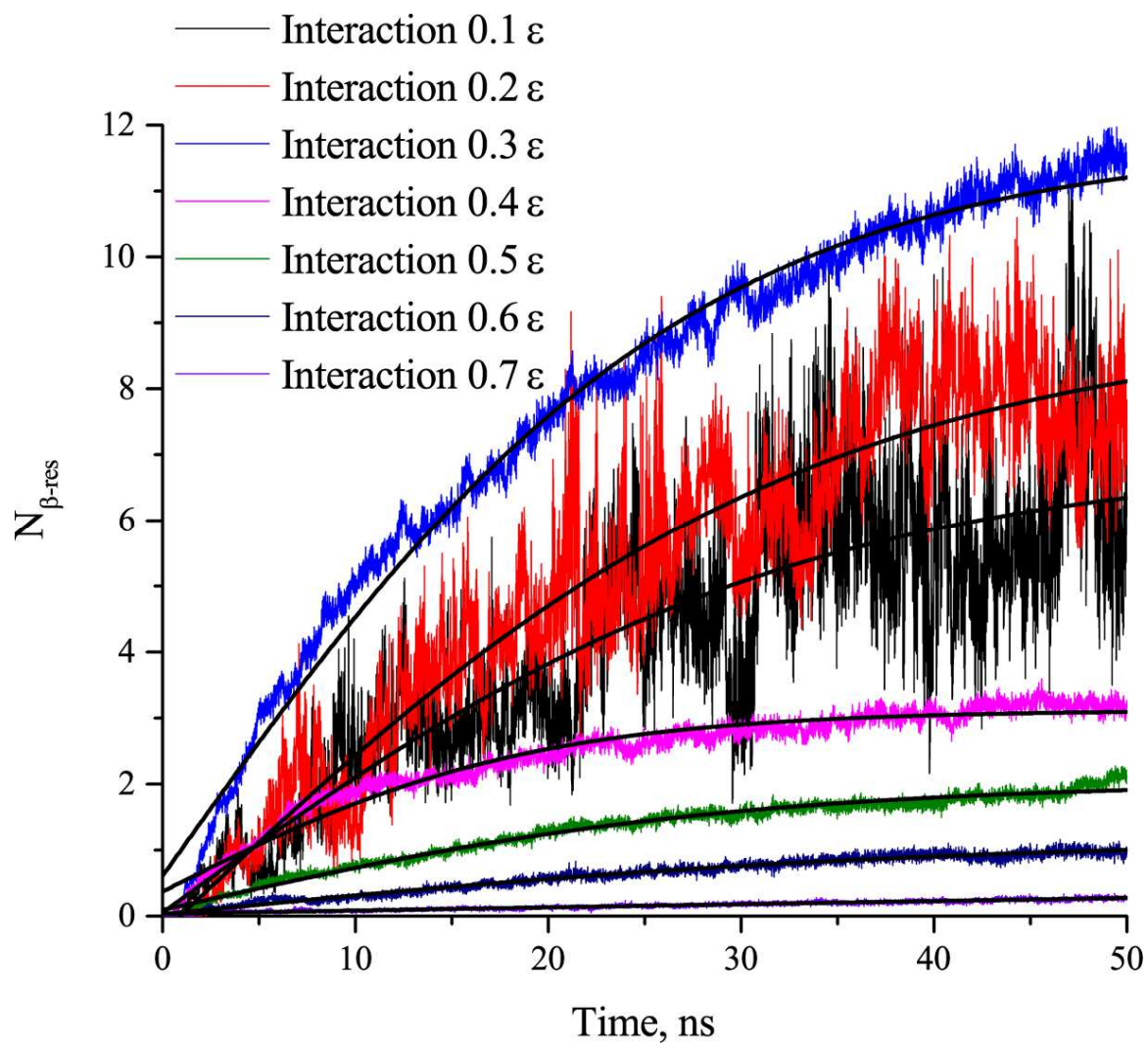
Figure D1. Sigmoidal fit of protein aggregation curves.
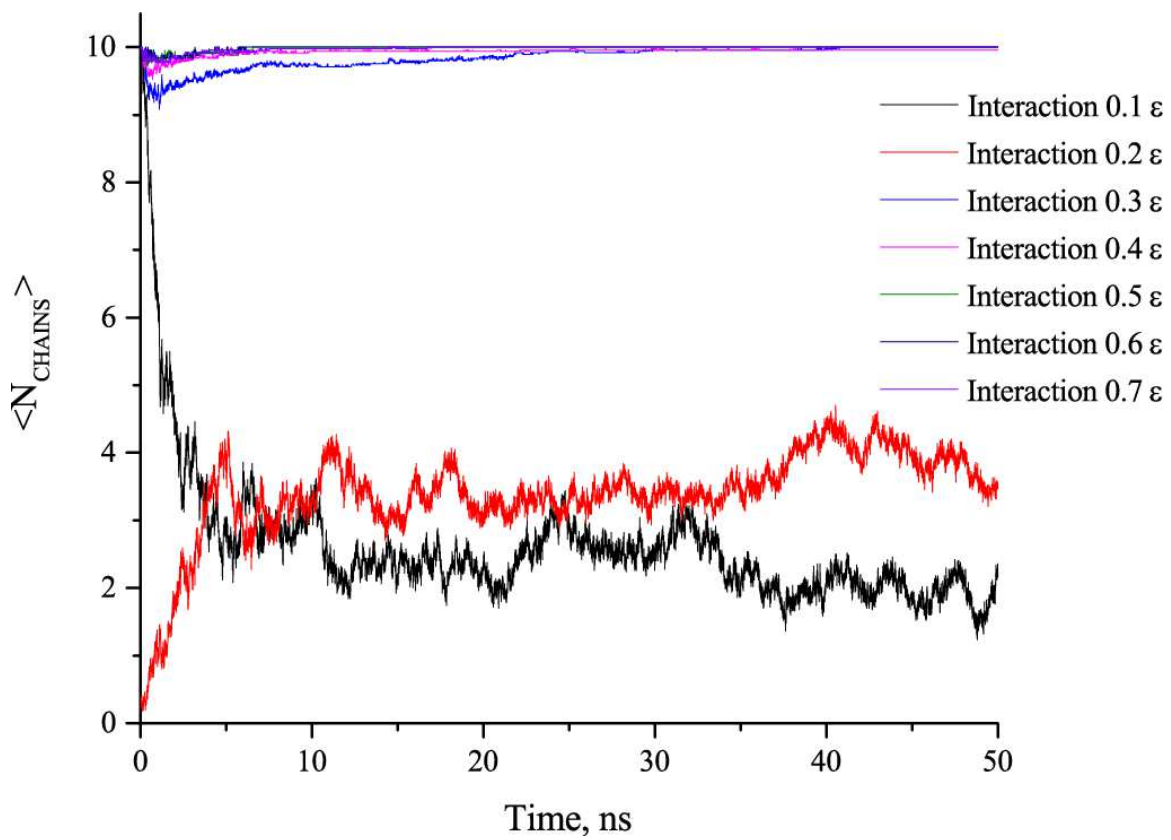
Figure D2. Average number of chains on nanoparticle surface over time.
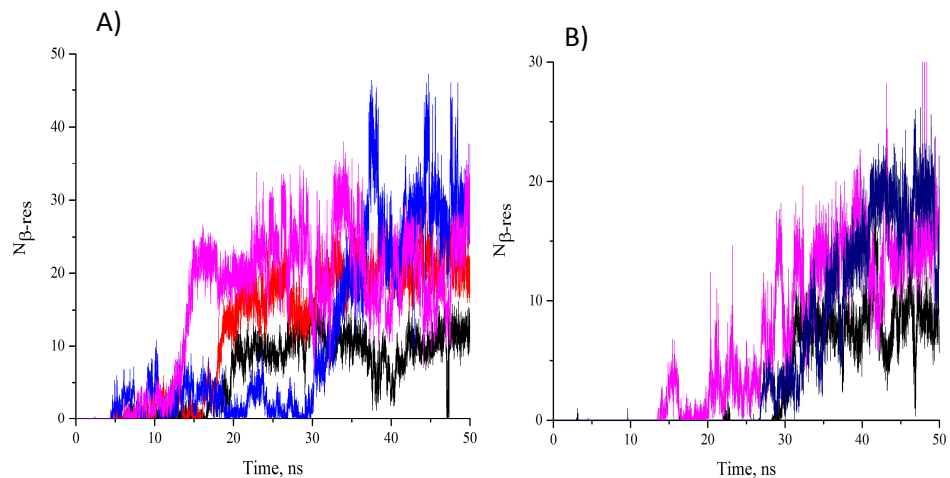
Figure D3. Non-averaged aggregation trajectories. A) Number of residues in β-sheets per chain in presence of nanoparticle (interaction 0.225ε) B) without nanoparticle (interaction switched off)
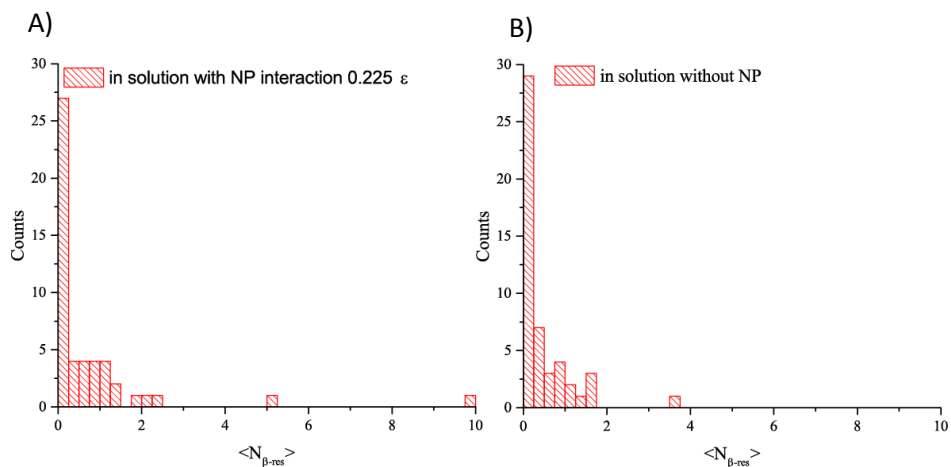
Figure D4. Influence of weak interaction on protein aggregation in solution. A) Average $N_{\beta\text{-res}}$ over first 25 ns distribution in presence of NP B) Average $N_{\beta\text{-res}}$ over first 25 ns distribution in absence of NP
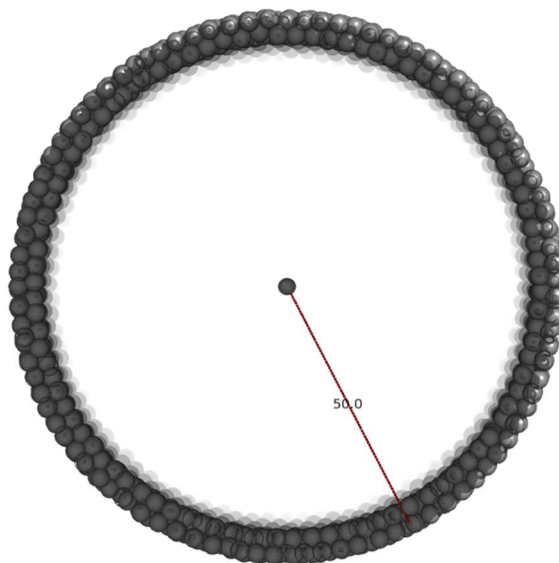
Figure D5. Nanoparticle model with two layers of atoms and radius of 5 nm.

Equation	D=A*exp(-B*x)		
Weight	Not weighted		
Res. Sum. of Sq.	0.02137		
Pearson's r	-0.99692		
Adj-R Sq.	0.99181		
		value	**STD**
	intercept	-3.33765	0.13869
D	**slope**	-5.87947	0.26691

Table D1. MSD Fit parameters.

COPYRIGHTS PERMISSIONS

Figure 1.8.

Figure 1.11:

Figure 1.9.

159

Figure 1.7

Figure 1.5

Mar 08, 2015

This is an Agreement between Slaven Radic ("You") and American Physical Society ("Publisher"). It consists of your order details, the terms and conditions provided by American Physical Society, and the payment instructions.

License Number	3584060697019
License date	Mar 08, 2015
Order Content Publisher	American Physical Society
Order Content Publication	Reviews of Modern Physics
Order Content Title	The electronic properties of graphene
Licensed copyright line	Copyright © 2009, American Physical Society
Order Content Author	A. H. Castro Neto et al.
Order Content Date	Jan 14, 2009
Volume number	81
I would like to...	Thesis/Dissertation
Requestor type	Student
Format	Print, Electronic
Portion	Image/photo
Number of images/photos requested	1
Portion description	FIG. 1.
Rights for	Main product
Duration of use	Life of current edition
Creation of copies for the disabled	no
With minor editing privileges	no
For distribution to	Worldwide
In the following language(s)	Original language of publication
With incidental promotional use	no
The lifetime unit quantity of new product	0 to 499
The requesting person/organization is:	Slaven Radic
Order reference number	None
Title of your thesis / dissertation	Biophysical Interaction between Nanoparticles and Biomolecules
Expected completion date	Mar 2015
Expected size (number of pages)	110
Total	**0.00 USD**

161

Figure 1.6

SPRINGER LICENSE
TERMS AND CONDITIONS

Mar 08, 2015

This is a License Agreement between Slaven Radic ("You") and Springer ("Springer") provided by Copyright Clearance Center ("CCC"). The license consists of your order details, the terms and conditions provided by Springer, and the payment terms and conditions.

All payments must be made in full to CCC. For payment instructions, please see information listed at the bottom of this form.

License Number	3582310364951
License date	Mar 05, 2015
Order Content Publisher	Springer
Order Content Publication	Nano Research
Order Content Title	Nano-graphene oxide for cellular imaging and drug delivery
Order Content Author	Xiaoming Sun
Order Content Date	Jan 1, 2008
Volume number	1
Issue number	3
Type of Use	Thesis/Dissertation
Portion	Figures
Author of this Springer article	No
Order reference number	None
Original figure numbers	Figure 4 A
Title of your thesis / dissertation	Biophysical interaction between Nanoparticles and Biomolecules
Expected completion date	Mar 2015
Estimated size(pages)	110
Total	0.00 USD

Terms and Conditions

Introduction

The publisher for this copyrighted material is Springer Science + Business Media. By clicking "accept" in connection with completing this licensing transaction, you agree that the following terms and conditions apply to this transaction (along with the Billing and Payment terms and conditions established by Copyright Clearance Center, Inc. ("CCC"), at the time that you opened your Rightslink account and that are available at any time at http://myaccount.copyright.com).

Limited License

With reference to your request to reprint in your thesis material on which Springer Science and Business Media control the copyright, permission is granted, free of charge, for the use indicated in your enquiry.

Licenses are for one-time use only with a maximum distribution equal to the number that you identified in the licensing process.

This License includes use in an electronic form, provided its password protected or on the university's intranet or repository, including UMI (according to the definition at the Sherpa website: http://www.sherpa.ac.uk/romeo/). For any other electronic use, please contact Springer at (permissions.dordrecht@springer.com or permissions.heidelberg@springer.com).

The material can only be used for the purpose of defending your thesis limited to university-use only. If the thesis is going

162

creative commons

L E G A L   C O D E

Attribution 2.5

License

THE WORK (AS DEFINED BELOW) IS PROVIDED UNDER THE TERMS OF THIS CREATIVE COMMONS PUBLIC LICENSE ("CCPL" OR "LICENSE"). THE WORK IS PROTECTED BY COPYRIGHT AND/OR OTHER APPLICABLE LAW. ANY USE OF THE WORK OTHER THAN AS AUTHORIZED UNDER THIS LICENSE OR COPYRIGHT LAW IS PROHIBITED.

BY EXERCISING ANY RIGHTS TO THE WORK PROVIDED HERE, YOU ACCEPT AND AGREE TO BE BOUND BY THE TERMS OF THIS LICENSE. THE LICENSOR GRANTS YOU THE RIGHTS CONTAINED HERE IN CONSIDERATION OF YOUR ACCEPTANCE OF SUCH TERMS AND CONDITIONS.

1. Definitions

   a. **"Collective Work"** means a work, such as a periodical issue, anthology or encyclopedia, in which the Work in its entirety in unmodified form, along with a number of other contributions, constituting separate and independent works in themselves, are assembled into a collective whole. A work that constitutes a Collective Work will not be considered a Derivative Work (as defined below) for the purposes of this License.

   b. **"Derivative Work"** means a work based upon the Work or upon the Work and other pre-existing works, such as a translation, musical arrangement, dramatization, fictionalization, motion picture version, sound recording, art reproduction, abridgment, condensation, or any other form in which the Work may be recast, transformed, or adapted, except that a work that constitutes a Collective Work will not be considered a Derivative Work for the purpose of this License. For the avoidance of doubt, where the Work is a musical composition or sound recording, the synchronization of the Work in timed-relation with a moving image ("synching") will be considered a Derivative Work for the purpose of this License.

   c. **"Licensor"** means the individual or entity that offers the Work under the terms of this License.

   d. **"Original Author"** means the individual or entity who created the Work.

   e. **"Work"** means the copyrightable work of authorship offered under the terms of this License.

   f. **"You"** means an individual or entity exercising rights under this License who has not previously violated the terms of this License with respect to the Work, or

Copyright Clearance Center

RightsLink®

Home   Account Info   Help   Live Chat

nature publishing group

Title:	Competitive Binding of Natural Amphiphiles with Graphene Derivatives
Author:	Slaven Radic, Nicholas K. Geitner, Ramakrishna Podila, Aleksandr Käkinen, Pengyu Chen, Pu Chun Ke
Publication:	Scientific Reports
Publisher:	Nature Publishing Group
Date:	Jul 24, 2013

Copyright © 2013, Rights Managed by Nature Publishing Group

Logged in as:
Slaven Radic
Account #:
3000895399

LOGOUT

Creative Commons

BACK   CLOSE WINDOW

AIP PUBLISHING LLC LICENSE
TERMS AND CONDITIONS

Mar 08, 2015

All payments must be made in full to CCC. For payment instructions, please see information listed at the bottom of this form.

License Number	3584051269475
Order Date	Mar 08, 2015
Publisher	AIP Publishing LLC
Publication	Applied Physics Letters
Article Title	Formation and cell translocation of carbon nanotube-fibrinogen protein corona
Author	Ran Chen,Slaven Radic,Poonam Choudhary, et al.
Online Publication Date	Sep 27, 2012
Volume number	101
Issue number	13
Type of Use	Thesis/Dissertation
Requestor type	Author (original article)
Format	Print and electronic
Portion	Excerpt (> 800 words)
Will you be translating?	No
Title of your thesis / dissertation	Biophysical Interaction between Nanoparticles and Biomolecules
Expected completion date	Mar 2015
Estimated size (number of pages)	110
Total	**0.00 USD**

Terms and Conditions

AIP Publishing LLC -- Terms and Conditions: Permissions Uses

AIP Publishing LLC ("AIPP") hereby grants to you the non-exclusive right and license to use and/or distribute the Material according to the use specified in your order, on a one-time basis, for the specified term, with a maximum distribution equal to the number that you have ordered. Any links or other content accompanying the Material are not the subject of this license.

1. You agree to include the following copyright and permission notice with the reproduction of the Material:"Reprinted with permission from [FULL CITATION]. Copyright [PUBLICATION YEAR] AIP Publishing LLC." For an article, the copyright and permission notice must be printed on the first page of the article or book chapter. For photographs, covers, or tables, the copyright and permission notice may appear with the Material, in a footnote, or in the reference list.

2. If you have licensed reuse of a figure, photograph, cover, or table, it is your responsibility to ensure that the material is original to AIPP and does not contain the copyright of another entity, and that the copyright notice of the figure, photograph, cover, or table does not indicate that it was reprinted by AIPP, with permission, from another source. Under no circumstances does AIPP, purport or intend to grant permission to reuse material to which it does not hold copyright.

3. You may not alter or modify the Material in any manner. You may translate the Material into another language only if you have licensed translation rights. You may not use the Material for promotional purposes. AIPP reserves all rights not specifically granted herein.

4. The foregoing license shall not take effect unless and until AIPP or its agent, Copyright Clearance Center, receives the Payment in accordance with Copyright Clearance Center Billing and Payment Terms and Conditions, which are incorporated herein by reference.

REFERENCES

1.   Roco, M. C. in *Nanotechnology Research Directions for Societal Needs in 2020* 1–28 (Springer Netherlands, 2011). at <http://link.springer.com/chapter/10.1007/978-94-007-1168-6_1>

2.   Dang, Y., Zhang, Y., Fan, L., Chen, H. & Roco, M. C. Trends in worldwide nanotechnology patent applications: 1991 to 2008. *J. Nanoparticle Res.* **12,** 687–706 (2010).

3.   *Nanotechnology Market Outlook 2020*. at <http://www.reportlinker.com/p02162665-summary/Nanotechnology-Market-Outlook.html>

4.   Nanotechnology for Drug Delivery : 2011-2021. *Cientifica Plc | Graphene | Emerging Technologies* at <http://www.cientifica.com/research/market-reports/nanotechnology-for-drug-delivery-2012/>

5.   Appenzeller, T. The man who dared to think small. *Science* **254,** 1300 (1991).

6.   Rudge, S. *et al.* Adsorption and desorption of chemotherapeutic drugs from a magnetically targeted carrier (MTC). *J. Control. Release Off. J. Control. Release Soc.* **74,** 335–340 (2001).

7.   Dobson, J. Gene therapy progress and prospects: magnetic nanoparticle-based gene delivery. *Gene Ther.* **13,** 283–287 (2006).

8.   Kang, Y. S., Risbud, S., Rabolt, J. F. & Stroeve, P. Synthesis and Characterization of Nanometer-Size Fe3O4 and γ-Fe2O3 Particles. *Chem. Mater.* **8,** 2209–2211 (1996).

9.   Salata, O. V. Applications of nanoparticles in biology and medicine. *J. Nanobiotechnology* **2,** 3 (2004).

10.   Nune, S. K. *et al.* Nanoparticles for biomedical imaging. *Expert Opin. Drug Deliv.* **6,** 1175–1194 (2009).

11.   Murphy, C. J. *et al.* Gold nanoparticles in biology: beyond toxicity to cellular imaging. *Acc. Chem. Res.* **41,** 1721–1730 (2008).

12.   Tong, L., Wei, Q., Wei, A. & Cheng, J.-X. Gold nanorods as contrast agents for biological imaging: optical properties, surface conjugation and photothermal effects. *Photochem. Photobiol.* **85,** 21–32 (2009).

13.   Jain, P. K., Huang, X., El-Sayed, I. H. & El-Sayed, M. A. Noble metals on the nanoscale: optical and photothermal properties and some applications in imaging, sensing, biology, and medicine. *Acc. Chem. Res.* **41,** 1578–1586 (2008).

14.   Mody, V. V., Siwale, R., Singh, A. & Mody, H. R. Introduction to metallic nanoparticles. *J. Pharm. Bioallied Sci.* **2,** 282–289 (2010).

15.   Dykman, L. A. & Khlebtsov, N. G. Gold Nanoparticles in Biology and Medicine: Recent Advances and Prospects. *Acta Naturae* **3,** 34–55 (2011).

16.   Cai, W., Gao, T., Hong, H. & Sun, J. Applications of gold nanoparticles in cancer nanotechnology. *Nanotechnol. Sci. Appl.* **1,** 17–32 (2008).

17.   Hu, M. *et al.* Dark-field microscopy studies of single metal nanoparticles: understanding the factors that influence the linewidth of the localized surface plasmon resonance. *J. Mater. Chem.* **18,** 1949–1960 (2008).

18.   Abou El-Nour, K. M. M., Eftaiha, A., Al-Warthan, A. & Ammar, R. A. A. Synthesis and applications of silver nanoparticles. *Arab. J. Chem.* **3,** 135–140 (2010).

19.   Kim, J. S. *et al.* Antimicrobial effects of silver nanoparticles. *Nanomedicine Nanotechnol. Biol. Med.* **3,** 95–101 (2007).

20.   Liu, L. *et al.* The potent antimicrobial properties of cell penetrating peptide-conjugated silver nanoparticles with excellent selectivity for gram-positive bacteria over erythrocytes. *Nanoscale* **5,** 3834–3840 (2013).

21.   Prabhu, S. & Poulose, E. K. Silver nanoparticles: mechanism of antimicrobial action, synthesis, medical applications, and toxicity effects. *Int. Nano Lett.* **2,** 1–10 (2012).

22.   Gupta, V. K., Mach, R. L. & Sreenivasaprasad, S. *Fungal Biomolecules: Sources, Applications and Recent Developments*. (John Wiley & Sons, 2015).

23.   Sondi, I. & Salopek-Sondi, B. Silver nanoparticles as antimicrobial agent: a case study on E. coli as a model for Gram-negative bacteria. *J. Colloid Interface Sci.* **275,** 177–182 (2004).

24.   Lara, H. H., Garza-Treviño, E. N., Ixtepan-Turrent, L. & Singh, D. K. Silver nanoparticles are broad-spectrum bactericidal and virucidal compounds. *J. Nanobiotechnology* **9,** 30 (2011).

25.   Danilczuk, M., Lund, A., Sadlo, J., Yamada, H. & Michalik, J. Conduction electron spin resonance of small silver particles. *Spectrochim. Acta. A. Mol. Biomol. Spectrosc.* **63,** 189–191 (2006).

26.   Alivisatos, A. P. Semiconductor Clusters, Nanocrystals, and Quantum Dots. *Science* **271,** 933–937 (1996).

27.   Murray, C. B., Norris, D. J. & Bawendi, M. G. Synthesis and characterization of nearly monodisperse CdE (E = sulfur, selenium, tellurium) semiconductor nanocrystallites. *J. Am. Chem. Soc.* **115,** 8706–8715 (1993).

28.   Brus, L. Electronic wave functions in semiconductor clusters: experiment and theory. *J. Phys. Chem.* **90,** 2555–2560 (1986).

29.   Resch-Genger, U., Grabolle, M., Cavaliere-Jaricot, S., Nitschke, R. & Nann, T. Quantum dots versus organic dyes as fluorescent labels. *Nat. Methods* **5,** 763–775 (2008).

30.   Smith, A. M., Duan, H., Mohs, A. M. & Nie, S. Bioconjugated Quantum Dots for In Vivo Molecular and Cellular Imaging. *Adv. Drug Deliv. Rev.* **60,** 1226–1240 (2008).

31.   Parak, W. J., Pellegrino, T. & Plank, C. Labelling of cells with quantum dots. *Nanotechnology* **16,** R9–R25 (2005).

32.   Zhang, L. W. & Monteiro-Riviere, N. A. Mechanisms of Quantum Dot Nanoparticle Cellular Uptake. *Toxicol. Sci.* **110,** 138–155 (2009).

33.   Delehanty, J. B. *et al.* Self-assembled quantum dot-peptide bioconjugates for selective intracellular delivery. *Bioconjug. Chem.* **17,** 920–927 (2006).

34.   Mostofizadeh, A., Li, Y., Song, B. & Huang, Y. Synthesis, Properties, and Applications of Low-Dimensional Carbon-Related Nanomaterials. *J. Nanomater.* **2011,** e685081 (2010).

35.   Cha, C., Shin, S. R., Annabi, N., Dokmeci, M. R. & Khademhosseini, A. Carbon-Based Nanomaterials: Multifunctional Materials for Biomedical Engineering. *ACS Nano* **7,** 2891–2897 (2013).

36.   Castro Neto, A. H., Guinea, F., Peres, N. M. R., Novoselov, K. S. & Geim, A. K. The electronic properties of graphene. *Rev. Mod. Phys.* **81,** 109–162 (2009).

37.   Novoselov, K. S. *et al.* Electric field effect in atomically thin carbon films. *Science* **306,** 666–669 (2004).

38.   Geim, A. K. & MacDonald, A. H. Graphene: Exploring carbon flatland. *Phys. Today* **60,** 35–41 (2007).

39.   Phillips, P. Fractionalize this. *Nat. Phys.* **6,** 931–933 (2010).

40.   Shi, H., Barnard, A. S. & Snook, I. K. Quantum mechanical properties of graphene nano-flakes and quantum dots. *Nanoscale* **4,** 6761–6767 (2012).

41.   Si, Y. & Samulski, E. T. Synthesis of Water Soluble Graphene. *Nano Lett.* **8,** 1679–1682 (2008).

42.   Chung, C. *et al.* Biomedical Applications of Graphene and Graphene Oxide. *Acc. Chem. Res.* **46,** 2211–2224 (2013).

43.   Bonaccorso, F., Sun, Z., Hasan, T. & Ferrari, A. C. Graphene photonics and optoelectronics. *Nat. Photonics* **4,** 611–622 (2010).

44.   Sun, X. *et al.* Nano-Graphene Oxide for Cellular Imaging and Drug Delivery. *Nano Res.* **1,** 203–212 (2008).

45.   Morales-Narvaez, E. & Merkoci, A. Graphene Oxide as an Optical Biosensing Platform. *Adv. Mater.* **24,** 3298–3308 (2012).

46.   Yang, Y., Asiri, A. M., Tang, Z., Du, D. & Lin, Y. Graphene based materials for biomedical applications. *Mater. Today* **16,** 365–373 (2013).

47.   Georgakilas, V. *et al.* Functionalization of Graphene: Covalent and Non-Covalent Approaches, Derivatives and Applications. *Chem. Rev.* **112,** 6156–6214 (2012).

48.   Katoch, J. *et al.* Structure of a Peptide Adsorbed on Graphene and Graphite. *Nano Lett.* **12,** 2342–2346 (2012).

49.   Pandey, R. B., Kuang, Z., Farmer, B. L., Kim, S. S. & Naik, R. R. Stability of peptide (P1 and P2) binding to a graphene sheet via an   all-atom to all-residue coarse-grained approach. *Soft Matter* **8,** 9101–9109 (2012).

50.   Kim, S. N. *et al.* Preferential Binding of Peptides to Graphene Edges and Planes. *J. Am. Chem. Soc.* **133,** 14480–14483 (2011).

51.   Kundu, A., Layek, R. K. & Nandi, A. K. Enhanced fluorescent intensity of graphene oxide–methyl cellulose hybrid in acidic medium: Sensing of nitro-aromatics. *J. Mater. Chem.* **22,** 8139–8144 (2012).

52.   O'Connell, M. J. *Carbon Nanotubes: Properties and Applications*. (CRC Press, 2006).

53.   Coleman, J. N., Khan, U., Blau, W. J. & Gun'ko, Y. K. Small but strong: A review of the mechanical properties of carbon nanotube–polymer composites. *Carbon* **44,** 1624–1652 (2006).

54.   Demczyk, B. G. *et al.* Direct mechanical measurement of the tensile strength and elastic modulus of multiwalled carbon nanotubes. *Mater. Sci. Eng. A* **334,** 173–178 (2002).

55.   Fuhrer, M. S. in *Advanced Semiconductor and Organic Nano-Techniques* (ed. Morkoç, H.) 293–343 (Academic Press, 2003). at <http://www.sciencedirect.com/science/article/pii/B9780125070607500209>

56.   Lee, S. M. *et al.* Hydrogen adsorption and storage in carbon nanotubes. *Synth. Met.* **113,** 209–216 (2000).

57.   Liu, Z., Tabakman, S., Welsher, K. & Dai, H. Carbon Nanotubes in Biology and Medicine: In vitro and in vivo Detection, Imaging and Drug Delivery. *Nano Res.* **2,** 85–120 (2009).

58.   Wang, J., Liu, G. & Jan, M. R. Ultrasensitive electrical biosensing of proteins and DNA: carbon-nanotube derived amplification of the recognition and transduction events. *J. Am. Chem. Soc.* **126,** 3010–3011 (2004).

59.   Liu, S. & Guo, X. Carbon nanomaterials field-effect-transistor-based biosensors. *NPG Asia Mater.* **4,** e23 (2012).

60.   Park, K. H., Chhowalla, M., Iqbal, Z. & Sesti, F. Single-walled carbon nanotubes are a new class of ion channel blockers. *J. Biol. Chem.* **278,** 50212–50216 (2003).

61.   Asuri, P. *et al.* Water-soluble carbon nanotube-enzyme conjugates as functional biocatalytic formulations. *Biotechnol. Bioeng.* **95,** 804–811 (2006).

62.   Harrison, B. S. & Atala, A. Carbon nanotube applications for tissue engineering. *Biomaterials* **28,** 344–353 (2007).

63.   Li, C. *et al.* Complementary Detection of Prostate-Specific Antigen Using In2O3 Nanowires and Carbon Nanotubes. *J. Am. Chem. Soc.* **127,** 12484–12485 (2005).

64.   Bhirde, A. A. *et al.* Targeted Killing of Cancer Cells in Vivo and in Vitro with EGF-Directed Carbon Nanotube-Based Drug Delivery. *Acs Nano* **3,** 307–316 (2009).

65.   Feazell, R. P., Nakayama-Ratchford, N., Dai, H. & Lippard, S. J. Soluble single-walled carbon nanotubes as longboat delivery systems for Platinum(IV) anticancer drug design. *J. Am. Chem. Soc.* **129,** 8438–+ (2007).

66.   Liu, Z. *et al.* Drug delivery with carbon nanotubes for in vivo cancer treatment. *Cancer Res.* **68,** 6652–6660 (2008).

67.   Wu, W. *et al.* Targeted delivery of amphotericin B to cells by using functionalized carbon nanotubes. *Angew. Chem. Int. Ed Engl.* **44,** 6358–6362 (2005).

68.   Taylor, R., Hare, J., Abdulsada, A. & Kroto, H. Isolation, Separation and Characterization of the Fullerenes C-60 and C-70 - the 3rd Form of Carbon. *J. Chem. Soc.-Chem. Commun.* 1423–1424 (1990). doi:10.1039/c39900001423

69.   Fagan, P. *et al.* Some Well Characterized Chemical Reactivities of Buckminsterfullerene (c-60). *Carbon* **30,** 1213–1226 (1992).

70.   Prylutskyy, Y. I. *et al.* C60 fullerene aggregation in aqueous solution. *Phys. Chem. Chem. Phys.* **15,** 9351–9360 (2013).

71.   Ikeda, A., Fukuhara, C. & Shinkai, S. Synthesis of 2-aminomethylpyridene-appended [60]fullerenes. On the difference in the metal-binding properties between 5,6-open and 6,6-closed Isomers. *Chem. Lett.* 915–916 (1998). doi:10.1246/cl.1998.915

72.   Yamakoshi, Y. *et al.* Active oxygen species generated from photoexcited fullerene (C60) as potential medicines: O2-* versus 1O2. *J. Am. Chem. Soc.* **125,** 12803–12809 (2003).

73.   Bensasson, R., Bienvenue, E., Dellinger, M., Leach, S. & Seta, P. C60 in Model Biological-Systems - a Visible-Uv Absorption Study of Solvent-Dependent Parameters and Solute Aggregation. *J. Phys. Chem.* **98,** 3492–3500 (1994).

74.   Hirsch, A., Lamparth, I. & Schick, G. Regioselectivity of multiple cyclopropanations of C-60 and introduction of a general bond-labeling algorithm for fullerenes and their derivatives. *Liebigs Ann.* 1725–1734 (1996).

75.   Scrivens, W., Tour, J., Creek, K. & Pirisi, L. Synthesis of C-14-Labeled C-60, Its Suspension in Water, and Its Uptake. *J. Am. Chem. Soc.* **116,** 4517–4518 (1994).

76.   Bianco, A. *et al.* Synthesis, chiroptical properties, and configurational assignment of fulleroproline derivatives and peptides. *J. Am. Chem. Soc.* **118,** 4072–4080 (1996).

77.   Chen, Y., Cai, R. F., Chen, S. M. & Huang, Z. E. Synthesis and characterization of fullerol derived from C-60(n-) precursors. *J. Phys. Chem. Solids* **62,** 999–1001 (2001).

78.   Tzoupis, H. *et al.* Binding of novel fullerene inhibitors to HIV-1 protease: insight through molecular dynamics and molecular mechanics Poisson–Boltzmann surface area calculations. *J. Comput. Aided Mol. Des.* **25,** 959–976 (2011).

79.   Friedman, S. H. *et al.* Inhibition of the HIV-1 protease by fullerene derivatives: model building studies and experimental verification. *J. Am. Chem. Soc.* **115,** 6506–6509 (1993).

80.   Sijbesma, R. *et al.* Synthesis of a Fullerene Derivative for the Inhibition of Hiv Enzymes. *J. Am. Chem. Soc.* **115,** 6510–6512 (1993).

81.   Shoji, M. *et al.* Anti-influenza activity of c60 fullerene derivatives. *PloS One* **8,** e66337 (2013).

82.   Wang, S., Gao, R., Zhou, F. & Selke, M. Nanomaterials and singlet oxygen photosensitizers: potential applications in photodynamic therapy. *J. Mater. Chem.* **14,** 487–493 (2004).

83.   Boutorine, A. S. *et al.* Fullerene–Oligonucleotide Conjugates: Photoinduced Sequence-Specific DNA Cleavage. *Angew. Chem. Int. Ed. Engl.* **33,** 2462–2465 (1995).

84.   Krusic, P. J., Wasserman, E., Keizer, P. N., Morton, J. R. & Preston, K. F. Radical reactions of c60. *Science* **254,** 1183–1185 (1991).

85.   Monti, D. *et al.* C60 carboxyfullerene exerts a protective activity against oxidative stress-induced apoptosis in human peripheral blood mononuclear cells. *Biochem. Biophys. Res. Commun.* **277,** 711–717 (2000).

86.   Nakamura, E. & Isobe, H. Functionalized fullerenes in water. The first 10 years of their chemistry, biology, and nanoscience. *Acc. Chem. Res.* **36,** 807–815 (2003).

87.   Foley, S. *et al.* Cellular localisation of a water-soluble fullerene derivative. *Biochem. Biophys. Res. Commun.* **294,** 116–119 (2002).

88.   Yin, X. *et al.* Impacts of fullerene derivatives on regulating the structure and assembly of collagen molecules. *Nanoscale* **5,** 7341–7348 (2013).

89.   Liu, Z., Suenaga, K. & Iijima, S. Imaging the Structure of an Individual C60 Fullerene Molecule and its Deformation Process Using HRTEM with Atomic Sensitivity. *J. Am. Chem. Soc.* **129,** 6666–6667 (2007).

90.   Cedervall, T., Hansson, L.-A., Lard, M., Frohm, B. & Linse, S. Food Chain Transport of Nanoparticles Affects Behaviour and Fat Metabolism in Fish. *PLoS ONE* **7,** e32254 (2012).

91.   Lin, S. *et al.* Uptake, Translocation, and Transmission of Carbon Nanomaterials in Rice Plants. *Small* **5,** 1128–1132 (2009).

92.   Buzea, C., Pacheco, I. I. & Robbie, K. Nanomaterials and nanoparticles: Sources and toxicity. *Biointerphases* **2,** MR17–MR71 (2007).

93.   Ma, S. & Lin, D. The biophysicochemical interactions at the interfaces between nanoparticles and aquatic organisms: adsorption and internalization. *Environ. Sci. Process. Impacts* **15,** 145–160 (2012).

94.   Cedervall, T. *et al.* Understanding the nanoparticle-protein corona using methods to quantify exchange rates and affinities of proteins for nanoparticles. *Proc. Natl. Acad. Sci. U. S. A.* **104,** 2050–2055 (2007).

95.   Sousa, S. R., Brás, M. M., Moradas-Ferreira, P. & Barbosa, M. A. Dynamics of Fibronectin Adsorption on TiO2 Surfaces. *Langmuir* **23,** 7046–7054 (2007).

96.   Renner, L., Pompe, T., Salchert, K. & Werner, C. Fibronectin Displacement at Polymer Surfaces. *Langmuir* **21,** 4571–4577 (2005).

97.   Renner, L., Pompe, T., Salchert, K. & Werner, C. Dynamic Alterations of Fibronectin Layers on Copolymer Substrates with Graded Physicochemical Characteristics. *Langmuir* **20,** 2928–2933 (2004).

98.   Lundqvist, M., Sethson, I. & Jonsson, B.-H. Protein adsorption onto silica nanoparticles: conformational changes depend on the particles' curvature and the protein stability. *Langmuir ACS J. Surf. Colloids* **20,** 10639–10647 (2004).

99.   Lundqvist, M., Sethson, I. & Jonsson, B.-H. High-resolution 2D 1H-15N NMR characterization of persistent structural alterations of proteins induced by interactions with silica nanoparticles. *Langmuir ACS J. Surf. Colloids* **21,** 5974–5979 (2005).

100.   Monopoli, M. P., Åberg, C., Salvati, A. & Dawson, K. A. Biomolecular coronas provide the biological identity of nanosized materials. *Nat. Nanotechnol.* **7,** 779–786 (2012).

101.   Milani, S., Bombelli, F. B., Pitek, A. S., Dawson, K. A. & Raedler, J. Reversible versus Irreversible Binding of Transferrin to Polystyrene   Nanoparticles: Soft and Hard Corona. *Acs Nano* **6,** 2532–2541 (2012).

102.   Hellstrand, E. *et al.* Complete high-density lipoproteins in nanoparticle corona. *FEBS J.* **276,** 3372–3381 (2009).

103.   Vácha, R., Martinez-Veracoechea, F. J. & Frenkel, D. Receptor-Mediated Endocytosis of Nanoparticles of Various Shapes. *Nano Lett.* **11,** 5391–5395 (2011).

104.	Alkilany, A. M. & Murphy, C. J. Toxicity and cellular uptake of gold nanoparticles: what we have learned so far? *J. Nanoparticle Res.* **12,** 2313–2333 (2010).

105.	Connor, E. E., Mwamuka, J., Gole, A., Murphy, C. J. & Wyatt, M. D. Gold Nanoparticles Are Taken Up by Human Cells but Do Not Cause Acute Cytotoxicity. *Small* **1,** 325–327 (2005).

106.	Shukla, R. *et al.* Biocompatibility of gold nanoparticles and their endocytotic fate inside the cellular compartment: a microscopic overview. *Langmuir ACS J. Surf. Colloids* **21,** 10644–10654 (2005).

107.	Otto, D. P. & Villiers, M. M. de. in *Nanotechnology in Drug Delivery* (eds. Villiers, M. M. de, Aramwit, P. & Kwon, G. S.) 3–33 (Springer New York, 2009). at <http://link.springer.com/chapter/10.1007/978-0-387-77668-2_1>

108.	Goodman, C. M., McCusker, C. D., Yilmaz, T. & Rotello, V. M. Toxicity of Gold Nanoparticles Functionalized with Cationic and Anionic Side Chains. *Bioconjug. Chem.* **15,** 897–900 (2004).

109.	Pan, Y. *et al.* Gold nanoparticles of diameter 1.4 nm trigger necrosis by oxidative stress and mitochondrial damage. *Small Weinh. Bergstr. Ger.* **5,** 2067–2076 (2009).

110.	Pan, Y. *et al.* Size-dependent cytotoxicity of gold nanoparticles. *Small Weinh. Bergstr. Ger.* **3,** 1941–1949 (2007).

111.	Patra, H. K., Banerjee, S., Chaudhuri, U., Lahiri, P. & Dasgupta, A. K. Cell selective response to gold nanoparticles. *Nanomedicine Nanotechnol. Biol. Med.* **3,** 111–119 (2007).

112.	Asharani, P. V., Lianwu, Y., Gong, Z. & Valiyaveettil, S. Comparison of the toxicity of silver, gold and platinum nanoparticles in developing zebrafish embryos. *Nanotoxicology* **5,** 43–54 (2011).

113.	Tarantola, M. *et al.* Toxicity of gold-nanoparticles: Synergistic effects of shape and surface functionalization on micromotility of epithelial cells. *Nanotoxicology* **5,** 254–268 (2011).

114.	Haase, A. *et al.* Toxicity of silver nanoparticles in human macrophages: uptake, intracellular distribution and cellular responses. *J. Phys. Conf. Ser.* **304,** 012030 (2011).

115.	Gliga, A. R., Skoglund, S., Wallinder, I. O., Fadeel, B. & Karlsson, H. L. Size-dependent cytotoxicity of silver nanoparticles in human lung cells: the role of cellular uptake, agglomeration and Ag release. *Part. Fibre Toxicol.* **11,** 11 (2014).

116.	Chen, L. Q. *et al.* Nanotoxicity of silver nanoparticles to red blood cells: Size-dependent adsorption, uptake and hemolytic activity. *Chem. Res. Toxicol.* (2015). doi:10.1021/tx500479m

117.	Käkinen, A. *et al.* Interaction of firefly luciferase and silver nanoparticles and its impact on enzyme activity. *Nanotechnology* **24,** 345101 (2013).

118.   Hirai, T. *et al.* Silver nanoparticles induce silver nanoparticle-specific allergic responses (HYP6P.274). *J. Immunol.* **192,** 118.19–118.19 (2014).

119.   De Lima, R., Seabra, A. B. & Durán, N. Silver nanoparticles: a brief review of cytotoxicity and genotoxicity of chemically and biogenically synthesized nanoparticles. *J. Appl. Toxicol. JAT* **32,** 867–879 (2012).

120.   Levard, C., Hotze, E. M., Lowry, G. V. & Brown, G. E. Environmental Transformations of Silver Nanoparticles: Impact on Stability and Toxicity. *Environ. Sci. Technol.* **46,** 6900–6914 (2012).

121.   Lam, C.-W., James, J. T., McCluskey, R. & Hunter, R. L. Pulmonary toxicity of single-wall carbon nanotubes in mice 7 and 90 days after intratracheal instillation. *Toxicol. Sci. Off. J. Soc. Toxicol.* **77,** 126–134 (2004).

122.   Takagi, A. *et al.* Induction of mesothelioma in p53+/- mouse by intraperitoneal application of multi-wall carbon nanotube. *J. Toxicol. Sci.* **33,** 105–116 (2008).

123.   Seabra, A. B., Paula, A. J., de Lima, R., Alves, O. L. & Durán, N. Nanotoxicity of Graphene and Graphene Oxide. *Chem. Res. Toxicol.* **27,** 159–168 (2014).

124.   Isakovic, A. *et al.* Distinct cytotoxic mechanisms of pristine versus hydroxylated fullerene. *Toxicol. Sci. Off. J. Soc. Toxicol.* **91,** 173–183 (2006).

125.   Benilova, I., Karran, E. & De Strooper, B. The toxic Aβ oligomer and Alzheimer's disease: an emperor in need of clothes. *Nat. Neurosci.* **15,** 349–357 (2012).

126.   Nucifora, L. G. *et al.* Identification of novel potentially toxic oligomers formed in vitro from mammalian-derived expanded huntingtin exon-1 protein. *J. Biol. Chem.* **287,** 16017–16028 (2012).

127.   Kalia, L. V., Kalia, S. K., McLean, P. J., Lozano, A. M. & Lang, A. E. α-Synuclein oligomers and clinical implications for Parkinson disease. *Ann. Neurol.* **73,** 155–169 (2013).

128.   C Cabaleiro-Lago, O. S. The effect of nanoparticles on amyloid aggregation depends on the protein stability and intrinsic aggregation rate. *Langmuir ACS J. Surf. Colloids* **28,** 1852–7 (2011).

129.   Zaman, M., Ahmad, E., Qadeer, A., Rabbani, G. & Khan, R. H. Nanoparticles in relation to peptide and protein aggregation. *Int. J. Nanomedicine* **9,** 899–912 (2014).

130.   Linse, S. *et al.* Nucleation of protein fibrillation by nanoparticles. *Proc. Natl. Acad. Sci.* **104,** 8691–8696 (2007).

131.   Cabaleiro-Lago, C., Quinlan-Pluck, F., Lynch, I., Dawson, K. A. & Linse, S. Dual Effect of Amino Modified Polystyrene Nanoparticles on Amyloid β Protein Fibrillation. *ACS Chem. Neurosci.* **1,** 279–287 (2010).

132.   Wu, W. *et al.* TiO2 nanoparticles promote β-amyloid fibrillation in vitro. *Biochem. Biophys. Res. Commun.* **373,** 315–318 (2008).

133.   Cabaleiro-Lago, C., Lynch, I., Dawson, K. A. & Linse, S. Inhibition of IAPP and IAPP [20–29] Fibrillation by Polymeric Nanoparticles. *Langmuir* **26,** 3453–3461 (2010).

134.   Liao, Y.-H., Chang, Y.-J., Yoshiike, Y., Chang, Y.-C. & Chen, Y.-R. Negatively charged gold nanoparticles inhibit Alzheimer's amyloid-β fibrillization, induce fibril dissociation, and mitigate neurotoxicity. *Small Weinh. Bergstr. Ger.* **8,** 3631–3639 (2012).

135.   Nel, A. E. *et al.* Understanding biophysicochemical interactions at the nano-bio interface. *Nat. Mater.* **8,** 543–557 (2009).

136.   Sund, J., Alenius, H., Vippola, M., Savolainen, K. & Puustinen, A. Proteomic characterization of engineered nanomaterial-protein interactions in relation to surface reactivity. *ACS Nano* **5,** 4300–4309 (2011).

137.   Ge, C. *et al.* Binding of blood proteins to carbon nanotubes reduces cytotoxicity. *Proc. Natl. Acad. Sci. U. S. A.* **108,** 16968–16973 (2011).

138.   Zuo, G., Huang, Q., Wei, G., Zhou, R. & Fang, H. Plugging into proteins: poisoning protein function by a hydrophobic nanoparticle. *ACS Nano* **4,** 7508–7514 (2010).

139.   Ratnikova, T. A., Govindan, P. N., Salonen, E. & Ke, P. C. In vitro polymerization of microtubules with a fullerene derivative. *ACS Nano* **5,** 6306–6314 (2011).

140.   Shang, J. *et al.* Experimental and simulation studies of a real-time polymerase chain reaction in the presence of a fullerene derivative. *Nanotechnology* **20,** 415101 (2009).

141.   Shen, J.-W., Wu, T., Wang, Q. & Kang, Y. Induced stepwise conformational change of human serum albumin on carbon nanotube surfaces. *Biomaterials* **29,** 3847–3855 (2008).

142.   Kubiak, K. & Mulheran, P. A. Molecular dynamics simulations of hen egg white lysozyme adsorption at a charged solid surface. *J. Phys. Chem. B* **113,** 12189–12200 (2009).

143.   Makarucha, A. J., Todorova, N. & Yarovsky, I. Nanomaterials in biological environment: a review of computer modelling studies. *Eur. Biophys. J. EBJ* **40,** 103–115 (2011).

144.   De Vries, A. H., Mark, A. E. & Marrink, S. J. Molecular dynamics simulation of the spontaneous formation of a small DPPC vesicle in water in atomistic detail. *J. Am. Chem. Soc.* **126,** 4488–4489 (2004).

145.   Chiu, C.-C., Dieckmann, G. R. & Nielsen, S. O. Molecular dynamics study of a nanotube-binding amphiphilic helical peptide at different water/hydrophobic interfaces. *J. Phys. Chem. B* **112,** 16326–16333 (2008).

146.   Chiu, C.-C., Dieckmann, G. R. & Nielsen, S. O. Role of peptide--peptide interactions in stabilizing peptide-wrapped single-walled carbon nanotubes: a molecular dynamics study. *Biopolymers* **92,** 156–163 (2009).

147.   Hung, A. *et al.* Ordering surfaces on the nanoscale: implications for protein adsorption. *J. Am. Chem. Soc.* **133,** 1438–1450 (2011).

148.   Auer, S., Trovato, A. & Vendruscolo, M. A condensation-ordering mechanism in nanoparticle-catalyzed peptide aggregation. *PLoS Comput. Biol.* **5,** e1000458 (2009).

149.   Pantarotto, D. *et al.* Synthesis, structural characterization, and immunological properties of carbon nanotubes functionalized with peptides. *J. Am. Chem. Soc.* **125,** 6160–6164 (2003).

150.   Ke, P. C. & Lamm, M. H. A biophysical perspective of understanding nanoparticles at large. *Phys. Chem. Chem. Phys. PCCP* **13,** 7273–7283 (2011).

151.   Bahr, J. L. & Tour, J. M. Covalent chemistry of single-wall carbon nanotubes. *J. Mater. Chem.* **12,** 1952–1958 (2002).

152.   Chen, R. J., Zhang, Y., Wang, D. & Dai, H. Noncovalent sidewall functionalization of single-walled carbon nanotubes for protein immobilization. *J. Am. Chem. Soc.* **123,** 3838–3839 (2001).

153.   Zheng, M. *et al.* DNA-assisted dispersion and separation of carbon nanotubes. *Nat. Mater.* **2,** 338–342 (2003).

154.   Rao, R. *et al.* Single-molecule fluorescence microscopy and Raman spectroscopy studies of RNA bound carbon nanotubes. *Appl. Phys. Lett.* **85,** 4228–4230 (2004).

155.   Wu, Y. *et al.* Coating single-walled carbon nanotubes with phospholipids. *J. Phys. Chem. B* **110,** 2475–2478 (2006).

156.   Lynch, I., Salvati, A. & Dawson, K. A. Protein-nanoparticle interactions: What does the cell see? *Nat. Nanotechnol.* **4,** 546–547 (2009).

157.   Shemetov, A. A., Nabiev, I. & Sukhanova, A. Molecular interaction of proteins and peptides with nanoparticles. *ACS Nano* **6,** 4585–4602 (2012).

158.   Lynch, I. & Dawson, K. A. Protein-nanoparticle interactions. *Nanotoday* **3,** 40–47 (2008).

159.   Mahmoudi, M. & Serpooshan, V. Large Protein Absorptions from Small Changes on the Surface of Nanoparticles. *J. Phys. Chem. C* **115,** 18275–18283 (2011).

160.   Vroman, L. Effect of absorbed proteins on the wettability of hydrophilic and hydrophobic solids. *Nature* **196,** 476–477 (1962).

161.   Cedervall, T. *et al.* Understanding the nanoparticle-protein corona using methods to quantify   exchange rates and affinities of proteins for nanoparticles. *Proc. Natl. Acad. Sci. U. S. A.* **104,** 2050–2055 (2007).

162. Wang, J. *et al.* Soft Interactions at Nanoparticles Alter Protein Function and Conformation in a Size Dependent Manner. *Nano Lett.* **11,** 4985–4991 (2011).

163. Brunauer, S., Emmett, P. H. & Teller, E. Adsorption of Gases in Multimolecular Layers. *J. Am. Chem. Soc.* **60,** 309–319 (1938).

164. Barrett, E. P., Joyner, L. G. & Halenda, P. P. The Determination of Pore Volume and Area Distributions in Porous Substances. I. Computations from Nitrogen Isotherms. *J. Am. Chem. Soc.* **73,** 373–380 (1951).

165. Mason, M. & Weaver, W. The Settling of Small Particles in a Fluid. *Phys. Rev.* **23,** 412–426 (1924).

166. Gao, G., Çagin, T. & Iii, W. A. G. Energetics, structure, mechanical and vibrational properties of single-walled carbon nanotubes. *Nanotechnology* **9,** 184 (1998).

167. Bachilo, S. M. *et al.* Structure-assigned optical spectra of single-walled carbon nanotubes. *Science* **298,** 2361–2366 (2002).

168. Lin, S. *et al.* Detection of phospholipid-carbon nanotube translocation using fluorescence energy transfer. *Appl. Phys. Lett.* **89,** 143118 (2006).

169. Mizuno, K. *et al.* A black body absorber from vertically aligned single-walled carbon nanotubes. *Proc. Natl. Acad. Sci. U. S. A.* **106,** 6044–6047 (2009).

170. Caspary, E. A. & Kekwick, R. A. Some physicochemical properties of human fibrinogen. *Biochem. J.* **67,** 41–48 (1957).

171. Poland, C. A. *et al.* Carbon nanotubes introduced into the abdominal cavity of mice show asbestos-like pathogenicity in a pilot study. *Nat. Nanotechnol.* **3,** 423–428 (2008).

172. Ge, C. *et al.* Binding of blood proteins to carbon nanotubes reduces cytotoxicity. *Proc. Natl. Acad. Sci. U. S. A.* **108,** 16968–16973 (2011).

173. Vaitheeswaran, S. & Garcia, A. E. Protein stability at a carbon nanotube interface. *J. Chem. Phys.* **134,** 125101 (2011).

174. Jana, A. K. & Sengupta, N. Adsorption mechanism and collapse propensities of the full-length, monomeric Aβ(1-42) on the surface of a single-walled carbon nanotube: a molecular dynamics simulation study. *Biophys. J.* **102,** 1889–1896 (2012).

175. Salvati, A. *et al.* Transferrin-functionalized nanoparticles lose their targeting capabilities when a biomolecule corona adsorbs on the surface. *Nat. Nanotechnol.* **8,** 137–143 (2013).

176. Barnard, A. S. How can ab initio simulations address risks in nanotech? *Nat. Nanotechnol.* **4,** 332–335 (2009).

177. Sotiriou, G. A. & Pratsinis, S. E. Antibacterial activity of nanosilver ions and particles. *Environ. Sci. Technol.* **44,** 5649–5654 (2010).

178.   Ding, F. & Dokholyan, N. V. Simple but predictive protein models. *Trends Biotechnol.* **23,** 450–455 (2005).

179.   Ding, F., Guo, W., Dokholyan, N. V., Shakhnovich, E. I. & Shea, J.-E. Reconstruction of the src-SH3 protein domain transition state ensemble using multiscale molecular dynamics simulations. *J. Mol. Biol.* **350,** 1035–1050 (2005).

180.   Ding, F., Furukawa, Y., Nukina, N. & Dokholyan, N. V. Local unfolding of Cu, Zn superoxide dismutase monomer determines the morphology of fibrillar aggregates. *J. Mol. Biol.* **421,** 548–560 (2012).

181.   Rapaport, D. C. *The art of molecular dynamics simulation*. (Cambridge University Press, 2004).

182.   Ding, F. & Dokholyan, N. V. Emergence of Protein Fold Families through Rational Design. *PLoS Comput. Biol.* **2,** e85 (2006).

183.   Lazaridis, T. & Karplus, M. Effective energy functions for protein structure prediction. *Curr. Opin. Struct. Biol.* **10,** 139–145 (2000).

184.   El Badawy, A. M. *et al.* Surface charge-dependent toxicity of silver nanoparticles. *Environ. Sci. Technol.* **45,** 283–287 (2011).

185.   Vijay-Kumar, S., Bugg, C. E. & Cook, W. J. Structure of ubiquitin refined at 1.8 A resolution. *J. Mol. Biol.* **194,** 531–544 (1987).

186.   Doni, G., Kostiainen, M. A., Danani, A. & Pavan, G. M. Generation-dependent molecular recognition controls self-assembly in supramolecular dendron-virus complexes. *Nano Lett.* **11,** 723–728 (2011).

187.   Calzolai, L., Franchini, F., Gilliland, D. & Rossi, F. Protein--nanoparticle interaction: identification of the ubiquitin--gold nanoparticle interaction site. *Nano Lett.* **10,** 3101–3105 (2010).

188.   Ding, F., Dokholyan, N. V., Buldyrev, S. V., Stanley, H. E. & Shakhnovich, E. I. Direct molecular dynamics observation of protein folding transition state ensemble. *Biophys. J.* **83,** 3525–3532 (2002).

189.   Ding, F., Dokholyan, N. V., Buldyrev, S. V., Stanley, H. E. & Shakhnovich, E. I. Molecular dynamics simulation of the SH3 domain aggregation suggests a generic amyloidogenesis mechanism. *J. Mol. Biol.* **324,** 851–857 (2002).

190.   Yang, S. *et al.* Domain swapping is a consequence of minimal frustration. *Proc. Natl. Acad. Sci. U. S. A.* **101,** 13786–13791 (2004).

191.   Röcker, C., Pötzl, M., Zhang, F., Parak, W. J. & Nienhaus, G. U. A quantitative fluorescence study of protein monolayer formation on colloidal nanoparticles. *Nat. Nanotechnol.* **4,** 577–580 (2009).

192.   Onuchic, J. N., Wolynes, P. G., Luthey-Schulten, Z. & Socci, N. D. Toward an outline of the topography of a realistic protein-folding funnel. *Proc. Natl. Acad. Sci. U. S. A.* **92,** 3626–3630 (1995).

193.   Yamago, S. *et al.* In vivo biological behavior of a water-miscible fullerene: 14C labeling, absorption, distribution, excretion and acute toxicity. *Chem. Biol.* **2,** 385–389 (1995).

194.   Oberdorster, E. Manufactured Nanomaterials (Fullerenes, C60) Induce Oxidative Stress in the Brain of Juvenile Largemouth Bass. *Environ. Health Perspect.* **112,** 1058–1062 (2004).

195.   Lin, C.-M. C60 Fullerene Derivatized Nanoparticles and their Application to Therapeutics. *Recent Pat. Nanotechnol.* **6,** 105–113 (2012).

196.   Da Ros, T. & Prato, M. Medicinal chemistry with fullerenes and fullerene derivatives. *Chem Commun* 663–669 (1999). doi:10.1039/A809495K

197.   Wang, I. C. *et al.* C60 and Water-Soluble Fullerene Derivatives as Antioxidants Against Radical-Initiated Lipid Peroxidation. *J. Med. Chem.* **42,** 4614–4620 (1999).

198.   Gharbi, N. *et al.* [60]Fullerene is a Powerful Antioxidant in Vivo with No Acute or Subacute Toxicity. *Nano Lett.* **5,** 2578–2585 (2005).

199.   Kolosnjaj, J., Szwarc, H. & Moussa, F. in *Bio-Applications of Nanoparticles* (ed. Chan, W. C. W.) 168–180 (Springer New York, 2007). at <http://link.springer.com/chapter/10.1007/978-0-387-76713-0_13>

200.   Yumita, N. *et al.* Sonodynamically-induced anticancer effects by functionalized fullerenes. *Anticancer Res.* **33,** 3145–3151 (2013).

201.   Ryan, J. J. *et al.* Fullerene nanomaterials inhibit the allergic response. *J. Immunol. Baltim. Md 1950* **179,** 665–672 (2007).

202.   Li, S., Zhao, X., Mo, Y., Cummings, P. T. & Heller, W. T. Human serum albumin interactions with C60 fullerene studied by spectroscopy, small-angle neutron scattering, and molecular dynamics simulations. *J. Nanoparticle Res.* **15,** 1–11 (2013).

203.   Benyamini, H. *et al.* Interaction of c(60)-fullerene and carboxyfullerene with proteins: docking and binding site alignment. *Bioconjug. Chem.* **17,** 378–386 (2006).

204.   Chen, B.-X., Wilson, S. R., Das, M., Coughlin, D. J. & Erlanger, B. F. Antigenicity of fullerenes: Antibodies specific for fullerenes and their characteristics. *Proc. Natl. Acad. Sci.* **95,** 10809–10813 (1998).

205.   Bosi, S., Ros, T. D., Spalluto, G. & Prato, M. Fullerene derivatives: an attractive tool for biological applications. *Eur. J. Med. Chem.* **38,** 913–923 (2003).

206.   Chen, Z., Ma, K., Wang, G., Zhao, X. & Tang, A. Structures and stabilities of C60(OH)4 and C60(OH)6 fullerenols. *J. Mol. Struct. THEOCHEM* **498,** 227–232 (2000).

207.	Eropkin, M. Y. *et al.* Synthesis and Biological Activity of Fullerenols with Various Contents of Hydroxyl Groups. *Pharm. Chem. J.* **47,** 87–91 (2013).

208.	Mikawa, M. *et al.* Paramagnetic water-soluble metallofullerenes having the highest relaxivity for MRI contrast agents. *Bioconjug. Chem.* **12,** 510–514 (2001).

209.	Grebowski, J., Krokosz, A. & Puchala, M. Fullerenol C60(OH)36 could associate to band 3 protein of human erythrocyte membranes. *Biochim. Biophys. Acta BBA - Biomembr.* **1828,** 2007–2014 (2013).

210.	Kokubo, K. in *The delivery of nanoparticles* 317–332. (InTech, 2012).

211.	Ratnikova, T. A., Govindan, P. N., Salonen, E. & Ke, P. C. In vitro polymerization of microtubules with a fullerene derivative. *ACS Nano* **5,** 6306–6314 (2011).

212.	Nedumpully Govindan, P., Monticelli, L. & Salonen, E. Mechanism of Taq DNA Polymerase Inhibition by Fullerene Derivatives: Insight from Computer Simulations. *J. Phys. Chem. B* **116,** 10676–10683 (2012).

213.	Monticelli, L., Barnoud, J., Orlowski, A. & Vattulainen, I. Interaction of C70 fullerene with the Kv1.2 potassium channel. *Phys. Chem. Chem. Phys. PCCP* **14,** 12526–12533 (2012).

214.	Wu, X. *et al.* Influences of the size and hydroxyl number of fullerenes/fullerenols on their interactions with proteins. *J. Nanosci. Nanotechnol.* **10,** 6298–6304 (2010).

215.	Deng, Z. J., Liang, M., Monteiro, M., Toth, I. & Minchin, R. F. Nanoparticle-induced unfolding of fibrinogen promotes Mac-1 receptor activation and inflammation. *Nat. Nanotechnol.* **6,** 39–44 (2011).

216.	Shang, W., Nuffer, J. H., Dordick, J. S. & Siegel, R. W. Unfolding of Ribonuclease A on Silica Nanoparticle Surfaces. *Nano Lett.* **7,** 1991–1995 (2007).

217.	Wettern, P. D. M. in *Progress in Botany* (eds. Behnke, P. D. H.-D., Esser, P. D. D. h c K., Kubitzki, P. D. K., Runge, P. D. M. & Ziegler, P. D. D. h c H.) 153–165 (Springer Berlin Heidelberg, 1992). at <http://link.springer.com/chapter/10.1007/978-3-642-77047-0_8>

218.	Hershko, A. & Ciechanover, A. The ubiquitin system. *Annu. Rev. Biochem.* **67,** 425–479 (1998).

219.	Ding, F., Tsao, D., Nie, H. & Dokholyan, N. V. Ab Initio Folding of Proteins with All-Atom Discrete Molecular Dynamics. *Structure* **16,** 1010–1018 (2008).

220.	Shirvanyants, D., Ding, F., Tsao, D., Ramachandran, S. & Dokholyan, N. V. Discrete Molecular Dynamics: An Efficient And Versatile Simulation Method For Fine Protein Characterization. *J. Phys. Chem. B* **116,** 8375–8382 (2012).

221.	Ding, F. *et al.* Direct observation of a single nanoparticle–ubiquitin corona formation. *Nanoscale* **5,** 9162–9169 (2013).

222.   Dobson, C. M. Principles of protein folding, misfolding and aggregation. *Semin. Cell Dev. Biol.* **15,** 3–16 (2004).

223.   Gsponer, J. & Vendruscolo, M. Theoretical approaches to protein aggregation. *Protein Pept. Lett.* **13,** 287–293 (2006).

224.   Sayes, C. M. *et al.* The Differential Cytotoxicity of Water-Soluble Fullerenes. *Nano Lett.* **4,** 1881–1887 (2004).

225.   Pinteala, M., Dascalu, A. & Ungurenasu, C. Binding fullerenol C60(OH)24 to dsDNA. *Int. J. Nanomedicine* **4,** 193–199 (2009).

226.   Qiao, R., Roberts, A. P., Mount, A. S., Klaine, S. J. & Ke, P. C. Translocation of C60 and Its Derivatives Across a Lipid Bilayer. *Nano Lett.* **7,** 614–619 (2007).

227.   Piątek, A., Dawid, A. & Gburski, Z. The properties of small fullerenol cluster (C60(OH)24)7: Computer simulation. *Spectrochim. Acta. A. Mol. Biomol. Spectrosc.* **79,** 819–823 (2011).

228.   Yang, S.-T. *et al.* Interaction of fullerenol with lysozyme investigated by experimental and computational approaches. *Nanotechnology* **19,** 395101 (2008).

229.   Jagielska, A. & Scheraga, H. A. Influence of temperature, friction, and random forces on folding of the B-domain of staphylococcal protein A: All-atom molecular dynamics in implicit solvent. *J. Comput. Chem.* **28,** 1068–1082 (2007).

230.   Srinivasan, R. & Rose, G. D. A physical basis for protein secondary structure. *Proc. Natl. Acad. Sci.* **96,** 14258–14263 (1999).

231.   Mesarič, T. *et al.* Effects of surface curvature and surface characteristics of carbon-based nanomaterials on the adsorption and activity of acetylcholinesterase. *Carbon* **62,** 222–232 (2013).

232.   Xu, H. *et al.* Graphene-based nanoprobes and a prototype optical biosensing platform. *Biosens. Bioelectron.* **50,** 251–255 (2013).

233.   Podila, R., Vedantam, P., Ke, P. C., Brown, J. M. & Rao, A. M. Evidence for Charge-Transfer-Induced Conformational Changes in Carbon Nanostructure–Protein Corona. *J. Phys. Chem. C* **116,** 22098–22103 (2012).

234.   Vijay-Kumar, S., Bugg, C. E. & Cook, W. J. Structure of ubiquitin refined at 1.8Åresolution. *J. Mol. Biol.* **194,** 531 – 544 (1987).

235.   Morris, G. M. *et al.* Automated Docking Using a Lamarckian Genetic Algorithm and an Empirical Binding Free Energy Function. *J. Comput. Chem.* **19,** 1639 (1998).

236.   Hess, B., Kutzner, C., Spoel, D. van der & Lindahl, E. GROMACS 4: Algorithms for Highly Efficient, Load-Balanced, and Scalable Molecular Simulation. *J Chem Theory Comput* **4,** 435 (2008).

237.   Jorgensen, W. L. & Tirado-Rives, J. The OPLS [optimized potentials for liquid simulations] potential functions for proteins, energy minimizations for crystals of cyclic peptides and crambin. *J. Am. Chem. Soc.* **110,** 1657–1666 (1988).

238.   Jorgensen, W. L., Maxwell, D. S. & Rives, J. T. Development and Testing of the OPLS All-Atom Force Field on Conformational Energetics and Properties of Organic Liquids. *J. Am. Chem. Soc.* **118,** 11225–11236 (1996).

239.   Jorgensen, W. L., Chandrasekhar, J., Madura, J. D., Impey, R. W. & Klein, M. L. Comparison of simple potential functions for simulating liquid water. *J. Chem. Phys.* **79,** 926–935 (1983).

240.   Bussi, G., Donadio, D. & Parrinello, M. Canonical sampling through velocity rescaling. *J. Chem. Phys.* **126,** 014101 (2007).

241.   Berendsen, H. J. C., Postma, J. P. M., Gunsteren, W. F. van, DiNola, A. & Haak, J. R. Molecular dynamics with coupling to an external bath. *J. Chem. Phys.* **81,** 3684 (1984).

242.   Parrinello, M. & Rahman, A. Polymorphic transitions in single crystals: A new molecular dynamics method. *J. Appl. Phys.* **52,** 7182 (1981).

243.   Hess, B., Bekker, H., Berendsen, H. J. C. & Fraaije, J. G. E. M. LINCS: A linear constraint solver for molecular simulations. *J. Comput. Chem.* **18,** 1463 (1997).

244.   Darden, T., York, D. & Pedersen, L. Particle mesh Ewald: An N [center-dot] log(N) method for Ewald sums in large systems. *J. Chem. Phys.* **98,** 10089–10092 (1993).

245.   Essmann, U. *et al.* A smooth particle mesh Ewald method. *J. Chem. Phys.* **103,** 8577–8593 (1995).

246.   *The PyMOL Molecular Graphics System, Version 1.5.0.4 Schrödinger, LLC.*

247.   Lakowicz, J. R. *Principles of Fluorescence Spectroscopy*. (Springer, 2007).

248.   Gauthier, T. D., Shane, E. C., Guerin, W. F., Seitz, W. R. & Grant, C. L. Fluorescence quenching method for determining equilibrium constants for polycyclic aromatic hydrocarbons binding to dissolved humic materials. *Environ. Sci. Technol.* **20,** 1162–1166 (1986).

249.   Huang, X. *et al.* Graphene-Based Materials: Synthesis, Characterization, Properties, and Applications. *Small* **7,** 1876–1902 (2011).

250.   Geim, A. K. Graphene: Status and Prospects. *Science* **324,** 1530–1534 (2009).

251.   He, Q., Wu, S., Yin, Z. & Zhang, H. Graphene-based electronic sensors. *Chem. Sci.* **3,** 1764–1772 (2012).

252.   Yang, W. *et al.* Carbon Nanomaterials in Biosensors: Should You Use Nanotubes or Graphene? *Angew. Chem.-Int. Ed.* **49,** 2114–2138 (2010).

253.   Qiu, J.-D., Huang, J. & Liang, R.-P. Nanocomposite film based on graphene oxide for high performance flexible   glucose biosensor. *Sens. Actuators B-Chem.* **160,** 287–294 (2011).

254.   Yang, K., Feng, L., Shi, X. & Liu, Z. Nano-graphene in biomedicine: theranostic applications. *Chem. Soc. Rev.* **42,** 530–547 (2013).

255.   Mass production of high quality graphene: An analysis of worldwide patents. at <http://www.nanowerk.com/spotlight/spotid=25744.php>

256.   THE World Market for Graphene 2010-2017 - Research and Markets. at <http://www.researchandmarkets.com/reports/2236835/the_world_market_for_graphene_20 102017>

257.   Wang, K. *et al.* Biocompatibility of Graphene Oxide. *Nanoscale Res. Lett.* **6,** 8 (2010).

258.   Ke, P. C. Fiddling the string of carbon nanotubes with amphiphiles. *Phys. Chem. Chem. Phys. PCCP* **9,** 439–447 (2007).

259.   Hlady, V. & Buijs, J. Protein adsorption on solid surfaces. *Curr. Opin. Biotechnol.* **7,** 72–77 (1996).

260.   Liu, Z., Robinson, J. T., Sun, X. & Dai, H. PEGylated nanographene oxide for delivery of water-insoluble cancer   drugs. *J. Am. Chem. Soc.* **130,** 10876–+ (2008).

261.   Erickson, K. *et al.* Determination of the Local Chemical Structure of Graphene Oxide and Reduced Graphene Oxide. *Adv. Mater.* **22,** 4467–4472 (2010).

262.   Pacilé, D. *et al.* Electronic properties and atomic structure of graphene oxide membranes. *Carbon* **49,** 966–972 (2011).

263.   Qin, W., Li, X., Bian, W.-W., Fan, X.-J. & Qi, J.-Y. Density functional theory calculations and molecular dynamics   simulations of the adsorption of biomolecules on graphene surfaces. *Biomaterials* **31,** 1007–1016 (2010).

264.   Rapaport, D. C. *The Art of Molecular Dynamics Simulation*. (Cambridge University Press, 2004).

265.   Ding, F., Tsao, D., Nie, H. & Dokholyan, N. V. Ab initio folding of proteins with all-atom discrete molecular dynamics. *Struct. Lond. Engl. 1993* **16,** 1010–1018 (2008).

266.   Nishiyama, Y., Sugiyama, J., Chanzy, H. & Langan, P. Crystal Structure and Hydrogen Bonding System in Cellulose Iα from Synchrotron X-ray and Neutron Fiber Diffraction. *J. Am. Chem. Soc.* **125,** 14300–14306 (2003).

267.   Metropolis, N. & Ulam, S. The Monte Carlo Method. *J. Am. Stat. Assoc.* **44,** 335 (1949).

268.   Chodera, J. D., Swope, W. C., Pitera, J. W., Seok, C. & Dill, K. A. Use of the weighted histogram analysis method for the analysis of   simulated and parallel tempering simulations. *J. Chem. Theory Comput.* **3,** 26–41 (2007).

269.   Chen, P., Powell, B. A., Mortimer, M. & Ke, P. C. Adaptive Interactions between Zinc Oxide Nanoparticles and Chlorella sp. *Environ. Sci. Technol.* **46,** 12178–12185 (2012).

270.   Podila, R., Vedantam, P., Ke, P. C., Brown, J. M. & Rao, A. M. Evidences For Charge Transfer-Induced Conformational Changes In Carbon Nanostructure-Protein Corona. *J. Phys. Chem. C Nanomater. Interfaces* **116,** 22098–22103 (2012).

271.   Park, S. & Ruoff, R. S. Chemical methods for the production of graphenes. *Nat. Nanotechnol.* **4,** 217–224 (2009).

272.   Podila, R., Rao, R., Tsuchikawa, R., Ishigami, M. & Rao, A. M. Raman spectroscopy of folded and scrolled graphene. *ACS Nano* **6,** 5784–5790 (2012).

273.   Haas, A. F. & Wild, C. Composition analysis of organic matter released by cosmopolitan coral   reef-associated green algae. *Aquat. Biol.* **10,** 131–138 (2010).

274.   Humphrey, W., Dalke, A. & Schulten, K. VMD: visual molecular dynamics. *J. Mol. Graph.* **14,** 33–38, 27–28 (1996).

275.   Hanwell, M. D. *et al.* Avogadro: an advanced semantic chemical editor, visualization, and analysis platform. *J. Cheminformatics* **4,** 17 (2012).

276.   Loh, K. P., Bao, Q., Eda, G. & Chhowalla, M. Graphene oxide as a chemically tunable platform for optical applications. *Nat. Chem.* **2,** 1015–1024 (2010).

277.   Dreyer, D. R., Park, S., Bielawski, C. W. & Ruoff, R. S. The chemistry of graphene oxide. *Chem. Soc. Rev.* **39,** 228–240 (2010).

278.   Bagri, A. *et al.* Structural evolution during the reduction of chemically derived graphene oxide. *Nat. Chem.* **2,** 581–587 (2010).

279.   Halgren, T. A. MMFF VI. MMFF94s option for energy minimization studies. *J. Comput. Chem.* **20,** 720–729 (1999).

280.   O'Boyle, N. M. *et al.* Open Babel: An open chemical toolbox. *J. Cheminformatics* **3,** 33 (2011).

281.   Yin, S., Biedermannova, L., Vondrasek, J. & Dokholyan, N. V. MedusaScore: an accurate force field-based scoring function for virtual drug screening. *J. Chem. Inf. Model.* **48,** 1656–1662 (2008).

282.   Proctor, E. A., Ding, F. & Dokholyan, N. V. Structural and thermodynamic effects of post-translational modifications in mutant and wild type Cu, Zn superoxide dismutase. *J. Mol. Biol.* **408,** 555–567 (2011).

283.	Kumar, S., Rosenberg, J. M., Bouzida, D., Swendsen, R. H. & Kollman, P. A. THE weighted histogram analysis method for free-energy calculations on biomolecules. I. The method. *J. Comput. Chem.* **13,** 1011–1021 (1992).

284.	Lundqvist, M. *et al.* Nanoparticle size and surface properties determine the protein corona with possible implications for biological impacts. *Proc. Natl. Acad. Sci. U. S. A.* **105,** 14265–14270 (2008).

285.	Bonner, J. C. *et al.* Interlaboratory evaluation of rodent pulmonary responses to engineered nanomaterials: the NIEHS Nano GO Consortium. *Environ. Health Perspect.* **121,** 676–682 (2013).

286.	Chen, R. *et al.* Formation and cell translocation of carbon nanotube-fibrinogen protein corona. *Appl. Phys. Lett.* **101,** 133702 (2012).

287.	Lee, Y. K., Choi, E.-J., Webster, T. J., Kim, S.-H. & Khang, D. Effect of the protein corona on nanoparticles for modulating cytotoxicity and immunotoxicity. *Int. J. Nanomedicine* **10,** 97–113 (2015).

288.	Cheng, Y. *et al.* Blood-brain barrier permeable gold nanoparticles: an efficient delivery platform for enhanced malignant glioma therapy and imaging. *Small Weinh. Bergstr. Ger.* **10,** 5137–5150 (2014).

289.	Li, J. *et al.* A multifunctional polymeric nanotheranostic system delivers doxorubicin and imaging agents across the blood-brain barrier targeting brain metastases of breast cancer. *ACS Nano* **8,** 9925–9940 (2014).

290.	Tang, J. *et al.* Silver nanoparticles crossing through and distribution in the blood-brain barrier in vitro. *J. Nanosci. Nanotechnol.* **10,** 6313–6317 (2010).

291.	Wong-Ekkabut, J. *et al.* Computer simulation study of fullerene translocation through lipid membranes. *Nat. Nanotechnol.* **3,** 363–368 (2008).

292.	Colvin, V. L. & Kulinowski, K. M. Nanoparticles as catalysts for protein fibrillation. *Proc. Natl. Acad. Sci.* **104,** 8679–8680 (2007).

293.	Auer, S., Trovato, A. & Vendruscolo, M. A Condensation-Ordering Mechanism in Nanoparticle-Catalyzed Peptide Aggregation. *PLoS Comput Biol* **5,** e1000458 (2009).

294.	Li, H., Luo, Y., Derreumaux, P. & Wei, G. Carbon Nanotube Inhibits the Formation of β-Sheet-Rich Oligomers of the Alzheimer's Amyloid-β(16-22) Peptide. *Biophys. J.* **101,** 2267–2276 (2011).

295.	Nelson, R. *et al.* Structure of the cross-β spine of amyloid-like fibrils. *Nature* **435,** 773–778 (2005).

296.	Cleary, J. P. *et al.* Natural oligomers of the amyloid-beta protein specifically disrupt cognitive function. *Nat. Neurosci.* **8,** 79–84 (2005).

297.   Hoffner, G., Souès, S. & Djian, P. Aggregation of Expanded Huntingtin in the Brains of Patients With Huntington Disease. *Prion* **1,** 26–31 (2007).

298.   Stefani, M. Biochemical and biophysical features of both oligomer/fibril and cell membrane in amyloid cytotoxicity. *FEBS J.* **277,** 4602–4613 (2010).

299.   Caughey, B. & Lansbury, P. T. Protofibrils, pores, fibrils, and neurodegeneration: separating the responsible protein aggregates from the innocent bystanders. *Annu. Rev. Neurosci.* **26,** 267–298 (2003).

300.   Moreth, J. *et al.* Globular and Protofibrillar Aβ Aggregates Impair Neurotransmission by Different Mechanisms. *Biochemistry (Mosc.)* **52,** 1466–1476 (2013).

301.   Ferrone, F. Analysis of protein aggregation kinetics. *Methods Enzymol.* **309,** 256–274 (1999).

302.   Guo, J. *et al.* Exploring the Influence of Carbon Nanoparticles on the Formation of β-Sheet-Rich Oligomers of IAPP22–28 Peptide by Molecular Dynamics Simulation. *PLoS ONE* **8,** (2013).

303.   Ueda, Y., Taketomi, H. & Gō, N. Studies on protein folding, unfolding, and fluctuations by computer simulation. II. A. Three-dimensional lattice model of lysozyme. *Biopolymers* **17,** 1531–1548 (1978).

304.   Sugita, Y. & Okamoto, Y. Replica-exchange molecular dynamics method for protein folding. *Chem. Phys. Lett.* **314,** 141–151 (1999).

305.   Jarrett, J. T., Berger, E. P. & Lansbury, P. T. The C-terminus of the beta protein is critical in amyloidogenesis. *Ann. N. Y. Acad. Sci.* **695,** 144–148 (1993).

306.   Walsh, D. M., Lomakin, A., Benedek, G. B., Condron, M. M. & Teplow, D. B. Amyloid beta-protein fibrillogenesis. Detection of a protofibrillar intermediate. *J. Biol. Chem.* **272,** 22364–22372 (1997).

307.   Lomakin, A., Teplow, D. B., Kirschner, D. A. & Benedek, G. B. Kinetic theory of fibrillogenesis of amyloid beta-protein. *Proc. Natl. Acad. Sci. U. S. A.* **94,** 7942–7947 (1997).

308.   Harper, J. D. & Lansbury, P. T. Models of amyloid seeding in Alzheimer's disease and scrapie: mechanistic truths and physiological consequences of the time-dependent solubility of amyloid proteins. *Annu. Rev. Biochem.* **66,** 385–407 (1997).

309.   Hosford, W. F. *Physical Metallurgy*. (CRC Press, 2005).

310.   Mahmoudi, M., Akhavan, O., Ghavami, M., Rezaee, F. & Ghiasi, S. M. A. Graphene oxide strongly inhibits amyloid beta fibrillation. *Nanoscale* **4,** 7322–7325 (2012).

311.   Allen, M. P. & Tildesley, D. J. *Computer Simulation of Liquids*. (Oxford University Press, 1989).

312.   Dokholyan, N. V. *Computational Modeling of Biological Systems: From Molecules to Pathways*. (Springer Science & Business Media, 2012).

313.   Origin (OriginLab, Northampton, MA). *Origin (OriginLab, Northampton, MA)* at <http://www.originlab.com/index.aspx?go=Company&pid=1130>

314.   Chen, R. *et al.* Interaction of lipid vesicle with silver nanoparticle-serum albumin protein corona. *Appl. Phys. Lett.* **100,** 13703–137034 (2012).

315.   Dagliyan, O., Proctor, E. A., D'Auria, K. M., Ding, F. & Dokholyan, N. V. Structural and dynamic determinants of protein-peptide recognition. *Struct. Lond. Engl. 1993* **19,** 1837–1845 (2011).

316.   Ding, F., Borreguero, J. M., Buldyrey, S. V., Stanley, H. E. & Dokholyan, N. V. Mechanism for the alpha-helix to beta-hairpin transition. *Proteins* **53,** 220–228 (2003).

317.   Neria, E., Fischer, S. & Karplus, M. Simulation of activation free energies in molecular systems. *J. Chem. Phys.* **105,** 1902–1921 (1996).

318.   Henglein, A. & Giersig, M. Formation of Colloidal Silver Nanoparticles: Capping Action of Citrate. *J. Phys. Chem. B* **103,** 9533–9539 (1999).

319.   Andersen, H. C. Molecular dynamics simulations at constant pressure and/or temperature. *J. Chem. Phys.* **72,** 2384 (1980).